ISSN 1880-8468

Technical Report of
International Development Engineering
国際開発工学報告

TRIDE-2012-03 February 29, 2012

Abstracts of Bachelor Theses
Presented in February 2012

Department of International Development Engineering,
Graduate School of Science and Engineering,
Tokyo Institute of Technology
http://www.ide.titech.ac.jp/TR

Preface

Bachelor theses of Department of International Development Engineering, Tokyo Institute of Technology were presented successfully on July 29, 2011, February 21, and 29, 2012. This technical report consists of the abstracts of those theses.

Technical Report of International Development Engineering
TRIDE-2012-03

Table of Contents

Multilink RSSI Measurement for Wireless BAN using ZigBee Devices

Student Number: 05B25458 Name: Takashi Yamazaki Supervisor: Jun-ichi Takada

1 Background

Nowadays, body area networks (BAN), which are short range networks on or near human body, is catching great attention. To date, BAN technologies have been applied for specific objectives such as military, medical purposes, but it is said that BAN will become more popular technology in various applications. In particular, it is expected that BAN is utilized in medical or healthcare purposes. BAN is expected to be applicable for Medical Information and Communication Technology (MICT) using networks comprised of implanted devices or sensor devices on body surfaces.

We have to take into account the effects of radiation to a human body during radio communication. Devices must communicate under restrictions such as SAR (specific absorption rate) and EMC (electro magnetic compatibility) regarding radio power. Thus, it is difficult to make communication reliable in BAN. Developing reliable communication systems with low radiation power is great challenge.

In previous studies, variation of radio propagation channels have been measured and BAN channel models have been developed. However, measurement scenarios were limited because the conventional measurement system was connected to the antennas with cables. The lengths of coaxial cables limited activity range, and in some cases, tensions of cables causes the positions of antennas to move. Also, the number of ports of instrument equipments is limited, so it was difficult to measure the properties with multiple sensor nodes.

2 Objectives

Cooperative transmission systems have been proposed as reliable transmission systems with samll radiation power [1]. To construct this system, we should be carefully investigated the characteristics of BAN multilink channels.

This research aims at constructing a wireless multilink system, to measure the variation of BAN channels using ZigBee devices (Fig.1). Using this system variation of BAN multilink channels due to the body motion can be investigated

ZigBee is a short range radio communication protocol and it has significant features of low power consumption and flexible network topology.

Figure 1: Crossbow IRIS Mote

3 Multilink RSSI measurement system

In this research the measurement system is composed of 10 ZigBee devices, one transmitter and nine receivers. Transmitter sends a message packet which contains the packet ID with a 12 second interval. When receiver devices detect a message packet, they record the receive signal strength indicator (RSSI) value and the packet number.

4 Experiments and Results

In the experiments, the channel responses were taken in two scenarios, “walking” and “running”. One transmitter node and nine receiver nodes were fixed on body surface (Fig.2) and the transmitted signal was recorded periodically at every receiver node simultaneously during walking or running in the hallway.

Figure.3 shows the measurement result of path gain variations in walking scenario at wrist, shoulder and waist. The proposed measurement system is applicable in the wider range of scenarios than the cable-connected system. These results are useful in the development of BAN channel models and evaluation of cooperative transmission techniques.

5 Conclusions

In this research, a channel measurement system using ZigBee devices has been proposed to realize the cable-free dynamic BAN multilink channel measurement. Some

Table 1: Correlation coefficient in walking scenario

Node	Wrist	Upper arm	Shoulder	Chest	Waist	Thin	Ankle	Ear	Back
Wrist	1								
Arm	0.31	1							
Shoulder	0.054	0.172	1						
Chest	-0.058	-0.032	0.152	1					
Waist	0.054	0.07	0.124	0.162	1				
Thin	0.162	0.244	0.062	-0.042	0.184	1			
Ankle	0.008	-0.062	0.014	-0.064	-0.072	0.044	1		
Ear	0.064	0.118	0.116	-0.044	0.128	0.106	0.072	1	
Back	0.08	0.102	0.172	0.114	0.026	0.028	-0.016	0.054	1

Figure 2: Positions of sensor devices

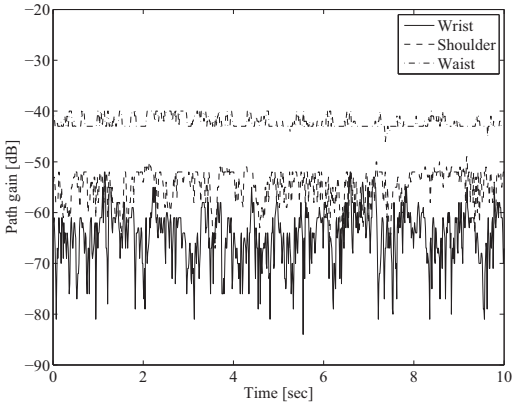

Figure 3: Measurement result in walking scenario

BAN multilink measurements are conducted, and the correlation properties of the channels are obtained.

References

[1] Xigang Huang, Hangguan Shan, Xuemin Shen: "On energy efficiency of cooperative communications in wireless body area network," Wireless Communications and Networking Conference (WCNC), IEEE, pp.1097–1101, 2011

[2] Minseok Kim, J. Takada: "Statistical Model for 4.5-GHz Narrowband On-Body Propagation Channel With Specific Actions," *Antennas and Wireless Propagation Letters, IEEE*, vol.8, pp.1250–1254, 2009

[3] L. Hanlen, V. Chaganti, B. Gilbert1, D. Rodda, T. Lamahewa, D. Smith: "Open-source Testbed for Body Area Networks: 200 sample/sec, 12 hrs Continuous Measurement," Personal, Indoor and Mobile Radio Communications Workshops (PIMRC Workshops), 2010 IEEE 21st International Symposium on

[4] D.B. Smith, L.W. Hanlen, T.A. Lamahewa: "A new look at the body area network channel model," Antennas and Propagation (EUCAP), Proceedings of the 5th European Conference on, pp.2987–2991, 2011

[5] S.L. Cotton, G.A. Conway, W.G. Scanlon: "A Time-Domain Approach to the Analysis and Modeling of On-Body Propagation Characteristics Using Synchronized Measurements at 2.45 GHz," Antennas and Propagation, IEEE Transactions on, Vol,57, Issue:4, pp.943–955, 2009

Recognition of mumerical value of electric emergy meter on Android devices

Student Number : 0 7 − 0 4 4 6 8　Yan Wansheng　Supervisor : Yukihiko Yamasita

1 Introduction

Human beings have been using a huge amount of energy such as oil and natural gas. Fossil fuel took about 200 million years to be accumulated by the energy of the sun. It will be spent in next 100 years or 200 years. Especially oil is said to be depleted in 40 years. Natural gas is said to be depleted in 60 years. Furthermore, greenhouse gas emission from fossil fuel use causes global warming. If greenhouse gas still continues to increase, averaged global temperature will rise from 2.4 to 6.4 °C in 100 years, and sea level will rise from 9 to 88cm. It casues various problems. Therefore, we have to reduce the use of fossil fuels. Natural energy such as solar power (renewable energy) is important to solve the proplem.

To make solar power a stable source of energy in a region, not only to install solar panels but also to maintain a stable power over time is important. Then it is necessary to determine whether the generator has been normal. Kakegawa where people have installed solar panels, is developing a self-diagnosis photovoltanic power generation system, and aims to create a solar network in the region. This self-diagnostic system measures the amount of solar radiation on equipment installed at City Hall and other representative points, and the amount of electricity generated by photovoltaic systems is estimated from the data. We can see it on web, and know the amount of power generated in the past period.

If we want to use this system, we must start a PC, record the number of a electric energy meter installed outside the house, and input the number into the PC. It is time consuming. If we can input the number more easily, the number of users of the system will increase, and the system will be more effective. This is the reason why I develop a system to input the value easily.

2 Recognition of number of electric energy meter on Android devices

Android devices are suitable for the purpose since they are very populer now. Smartphone shipments have already exceeded PC shipments.

The process of energy meter recognition by Android devices consists of image acquisition, preprocessing, and classification.

2.1 Image acquisition and preprocessing

Process of image acquisition and preprocessing is as follows.

1. Take a picture of the electric energy meter. (Figure 1)

Figure 1: Photos of energy meters

2. Cut out the numeric rengion of the image. (Figure 2) .

Figure 2: Part of the number

3. Obtain the threshold for binarization by Otsu's method .

4. Binarize the image by it. (Figure 3)

Figure 3: Binarized image

5. Label the objects in the image, and extract number objects.

6. Normalize an extracted number object to 16 × 16-pixels image. (Figure 4) .

Figure 4: Extracted number

2.2 Classfification

k-nearest neighbor classifier is used to discriminate the number. I explain this method. First we retrieve the k training samples in the proximity of the input pattern x from training sample set. That is, calculate the distance between the input pattern x and training samples, retrieving the k nearest training samples. Count the number of training samples belonging to each category. Classify the input pattern x to the category which have the most training samples among the extracted k training samples. The input pattern x is a 256-dimensional vector.

$$x = \left[\begin{array}{cccc} x_1 & x_2 & ..... & x_{256} \end{array} \right] ..... \quad (1)$$

Let x_{ij} be the j-th training sample of the i-th class. The distance D_{ij} between x_{ij} and x is given by

$$D_{ij} = \sqrt{(x_{ij1} - x_1)^2 + ... + (x_{ij256-x_{256}})^2} .... \quad (2)$$

The number of the extracted k nearest training samples belonging to category i is denoded by K_i. x is classified into the category with the largest K_i.

3 Experiment

I took pictures of energy meters by an Android device, performed pretreatment, and classified to 10 classes from 0 to 9 by hand. They make up the training sampleset. Training data consist of 200 16 × 16-pixels images. 23 photos are taken by Android decice and recognized for test. 19 photos were correctly recognized. Then accurate recognition rate is 82.6%.

Figures 5 and 6 are the results of the same power meter, but photographs are taken from different angles. Figure 6 is a result of misclassification. To resolve this problem, we have to increase training samples, or the angle have to be set carefully when taking a photo. Figure 8 is a result of misclassification because of reflection of light by the glass on the energy meter.

4 Conclusion

I proposed a system to recognize the number of electric energy meter. I conducted experiments to show it's perfomance. If the photo is taken clearly, the system

Figure 5: Accurate identification

Figure 6: Incorrect identification 1

Figure 7: Incorrect identification 2

can recognized the number correctly. For future work, we have to derelop a system for noisy image.

References

[1] Eiichi Furukawa, "Android 2.1 programming bible, "Sosimu, 2010

[2] Keiji Shotasu, " Programming of Image Processing, "SoftBank Creative, 2008

[3] Richard O.Duda, Peter E.Hart, David G.Stork, "Pattern identification, "Communications Tech, 2003

[4] Jyunichirou Toriwaki, "Recognition Engineering, "Corona Co, Ltd, 1993

[5] Masashi Sugiyama, "Statistical Machine Learning: Pattern Recognition Based on Enerative Model, "Ohmsha, Ltd, 2009

未利用海藻資源からのバイオエタノール生成

学籍番号：07-22101　氏名：ヒョウ　ウンテキ　指導教員：中崎　清彦

1 目的

近年、石油代替燃料としてバイオエタノールが注目されており、食糧と競合することのないバイオマスからエタノールを効率よく生産する方法の開発が期待を集めている。そのため、リグノセルロース性資源からのエタノール生成が多く試みられているが、通常のリグノセルロース性資源は、セルロースやヘミセルロースの糖化を阻害するリグニンを除去するための前処理が必要であり、エタノール生産コストや生産エネルギーを上昇させることが問題となっている。本研究では、リグニン含有量が低いバイオマスとして海藻に着目し、海藻からのエタノール生成について検討した。また、海藻は一旦糖化してエタノールに発酵するので、糖化で生成する糖を高濃度化することにより、引き続く発酵で生成するエタノールの高濃度化を試みた。

2 実験方法

2.1 使用した海藻、酵素、および酵母

海藻として、緑藻綱、および褐藻綱に属するアナアオサ、およびチガイソを用いた。アナアオサには、グルコースを構成糖とする多糖類であるグルカンとして、セルロースとでんぷんが合わせて 22.0%含まれており、チガイソにはグルカンとしてセルロースと β-1,3-グルカンが合わせて 24.5%含まれていることを確かめている。

糖化酵素としては、*Trichoderma viride* 由来の Meicelase（CEPB-5394, Meiji Seika Kaisya Ltd., Japan）を使用し、酵母としては、*Saccharomyces cerevisiae* IAM 4178 を使用した。

2.2 メイセラーゼのグルカン分解活性

アナアオサとチガイソに含まれるグルカンであるセルロース、でんぷん、および β-1,3-グルカンをメイセラーゼが分解可能か確かめるために、試薬のセルロースパウダー（Avicel）、でんぷん（Starch, Soluble）、β-1,3-グルカン（Curdlan）の糖化を試みた。0.1M クエン酸緩衝液にメイセラーゼを 1 g/L となるように溶解し、それぞれの試薬のグルカンを 20g/L となるように添加して反応させた。pH を 5.5、温度を 50°C、100 rpm の条件で 120 時間糖化した。また、糖化で生成したグルコース濃度を HPLC により測定した。

2.3 海藻の連続糖化

海藻にメイセラーゼを作用させて糖化し、海藻中グルカンからグルコースが生成可能か確かめた。pH を 5.5 に調整した 0.1M クエン酸緩衝液にメイセラーゼを 5 g/L、海藻粉末を 300 g/L となるように添加し、50°C で 120 時間糖化した。

引き続いて、糖化液を再び次の糖化に用いる連続糖化により、生成するグルコースの高濃度化を試みた。糖化後の海藻を遠心分離により固液分離し、上澄み液を糖化液として回収した。さらに、回収した糖化液にメイセラーゼを 5 g/L、新たに用意した海藻粉末を 300 g/L となるように添加して再度糖化をおこなった。なお、糖化期間中は均一な反応進行のために 24 時間毎にリアクタ内をスパーテルにより混合・攪拌した。また、1 回目、および 2 回目の糖化で生成したグルコース濃度を HPLC により測定した。

2.4 連続糖化した海藻の発酵

連続糖化した海藻に酵母を作用させ、エタノールが生成可能か確かめた。連続糖化後の海藻に yeast extract を 3 g/L、Polypepton を 5 g/L となるように添加し、*Saccharomyces cerevisiae* IAM 4178 を 10^8 CFU/mL となるように接種して 30°C で培養した。また、培養にともなって変化するグルコース、エタノール、および副生成物であるグリセロール濃度を HPLC により測定した。

3 結果と考察

3.1 メイセラーゼのグルカン分解活性

メイセラーゼによるセルロースパウダー、でんぷん、β-1,3-グルカンの糖化におけるグルコース濃度の経時変化を Fig. 1 に示す。いずれのグルカンを用いた場合もグルコースが生成し、120 時間後にはセルロースパウダー、でんぷん、β-1,3-グルカンからそれぞれ 14.2、11.1、8.93 g/L のグルコースが生成した。この結果から、メイセラーゼがこれらのグルカンを加水分解可能であることが確かめられた。

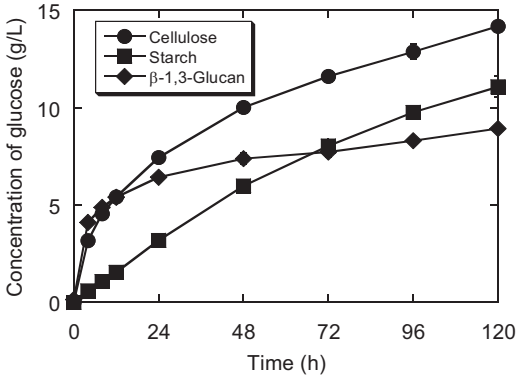

Fig. 1 The courses of glucose concentration during the enzymatic hydrolysis of various types of glucans. Error bars for the concentrations of glucose indicate a 95% confidence interval for the averaged values (n = 3).

3.2 海藻の連続糖化

アナアオサとチガイソの連続糖化における糖化 1 回目、および 2 回目の 120 時間後のグルコース濃度を Fig. 2 に示す。1 回目の糖化 120 時間後にはアナアオサから 43.1 g/L、チガイソから 67.7 g/L のグルコースが生成したことから、メイセラーゼがアナアオサやチガイソ中のグルカンを分解可能であることが確かめられた。なお、アナアオサ、およびチガイソ中グルカンのグルコースへの変化率は、それぞれ 58.8%、および 82.9%となった。脱リグニン処理を施していない木材粉末の糖化においては、セルロースの変化率が 13%となっていることから[1]、海藻中の

グルカンが酵素により分解されやすいことがわかった。これは、海藻中のリグニン含有量が低いためであると考えられた。

2 回目の糖化 120 時間後にはアナアオサから 78.8 g/L、チガイソから 123 g/L のグルコースが生成し、どちらも 1 回の糖化で生成したグルコース濃度の 1.8 倍となった。このことから、連続糖化によりグルコースの高濃度化が可能であることが確かめられた。

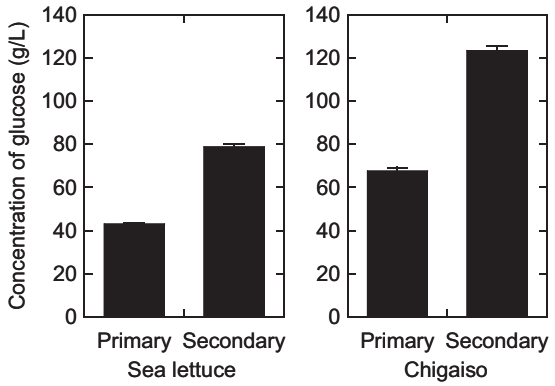

Fig. 2 Comparison of glucose concentrations after the successive saccharifications of sea lettuce and chigaiso. Error bars for the concentrations of glucose indicate a 95% confidence interval for the averaged values (n = 3).

3.3 連続糖化した海藻の発酵

連続糖化したアナアオサ、およびチガイソの発酵におけるグルコース、エタノール、グリセロール濃度の経時変化をそれぞれ Fig. 3、および Fig. 4 に示す。アナアオサでは、発酵 24 時間後のエタノール、およびグリセロール濃度がそれぞれ 30.0、および 6.91 g/L となり、グルコースからのエタノール収率は理論収率の 73.9%となった。また、チガイソでは、発酵 72 時間後に 12.4 g/L のグルコースが残存し、エタノール、およびグリセロール濃度はそれぞれ 34.4、および 17.2 g/L となったことから、エタノール収率は 59.8%となった。ここには詳細を示さないが、1 回糖化したアナアオサ、およびチガイソの発酵では、エタノール収率はそれぞれ 86.6、および 75.9%であったので、連続糖化により、その後の発酵におけるエタノール収率が低下することがわかった。これは、副生成物であるグリセロールの収率が高くなったためであると考えられた。なお、グルコースからのグリセロール収率は、1 回糖化したアナアオサ、およびチガイソの発酵においてそれぞれ 0.06、および 0.10g-glycerol/g-glucose であったが、2 回糖化した後の発酵ではそれぞれ 0.09、および 0.15g-glycerol/g-glucose となった。浸透圧が高い条件で酵母を培養するとエタノール収率が低下してグリセロール収率が上昇することが報告されていることから[2]、連続糖化において糖化液に溶出する物質の濃度が高くなったことにより発酵時の浸透圧が高くなり、グリセロール収率が高くなったことが考えられた。

以上の結果、連続糖化によりエタノール収率が低下するものの、エタノールの高濃度化が可能であることが確かめられた。

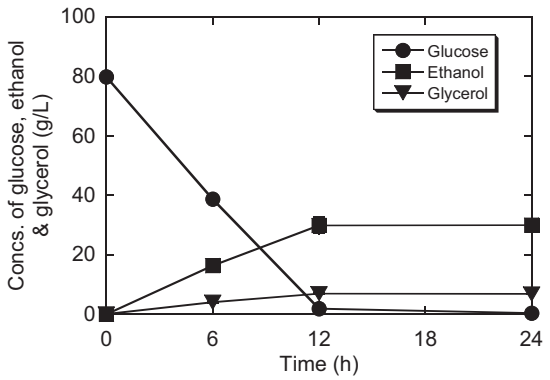

Fig. 3 The courses of the concentrations of glucose, ethanol, and glycerol during the fermentation of sea lettuce hydrolysate prepared by successive saccharification. Error bars for the concentrations of glucose, ethanol, and glycerol indicate a 95% confidence interval for the averaged values (n = 3).

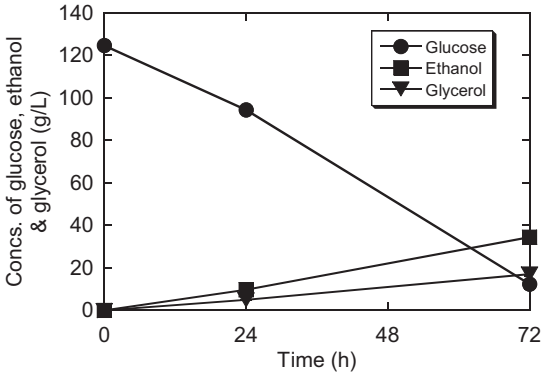

Fig. 4 The courses of the concentrations of glucose, ethanol, and glycerol during the fermentation of chigaiso hydrolysate prepared by successive saccharification. Error bars for the concentrations of glucose, ethanol, and glycerol indicate a 95% confidence interval for the averaged values (n = 3).

4 結論

本研究では、リグニン含有量が低い海藻からのバイオエタノール生成と連続糖化によるエタノールの高濃度化を試みた。まず、海藻をメイセラーゼで糖化することによりグルコースが生成可能であり、連続糖化によりアナアオサから 78.8 g/L、チガイソから 123 g/L と高濃度のグルコースを生成することができた。このことから、2 回目の糖化における酵素に対する阻害は小さいことが確かめられた。また、連続糖化によりグルコースを高濃度化することで、エタノール収率が低下するもののエタノールも 30 g /L 以上に高濃度化することができた。

References

[1] Yamashita, Y., et al.: Effective enzyme saccharification and ethanol production from Japanese cedar using various pretreatment methods. J. Biosci. Bioeng., **110**, 79-86 (2010)

[2] Modig, T., et al.: Anaerobic glycerol production by *Saccharomyces cerevisiae* strains under hyperosmotic stress. Appl. Microbiol. Biotechnol., **75**, 289-296 (2007)

Experimental study on grip-release mechanism

of slanted multi-beam structure with Ti-Ni super elastic wire

Student number:04B04186 name: Kazuhito EMURA supervisor: Kunio TAKAHASHI

February 17, 2012

1. Introduction

Geckos can quickly move on wall and ceiling against gravity. It has been said the ability depends on a lot of hairs with two level nano-scaled structure on their foot surface, called seta-spatula [1]. By this structure, it is possible to absorb surface roughness and to grip various surfaces by Van der Waals force [2][3]. Large gripping force causes difficulty in the release of surfaces. The geckos use tangential force to control the gripping force. It is suggested that the beam and the contact plane are required to mimic the function of the gecko fingers [4]. The effect of the beam curvature on the gripping force is investigated using the beam theory and the experiments with a single beam structure [5][6]. A prototype multi-beam structure is demonstrated by Wang [7]. However, the beams are vertical and too hard to absorb the surface roughness.

In the present study, a multi-beam structure with soft and slanted beams is made using Ni-Ti wire, the gripping function is investigated, and discussed with the beam theory.

2. Mechanism to control grip and release

It is assumed that all beams are equal to each other and the dynamics of multi-beam structure are equivalent to superposition of one of single beam and the criterion of adhesion crack is whether maximum normal stress is larger than critical stress.

Assume that top of elastic beam contacts with flat rigid surface, applying normal force F_n to the structure cause stress distribution at contact area as shown Fig.1. If tangential force F_t is applied with F_n, the maximum stress decreases and the structure can grip the surface. In this way, the beam structure can control grip and release. .

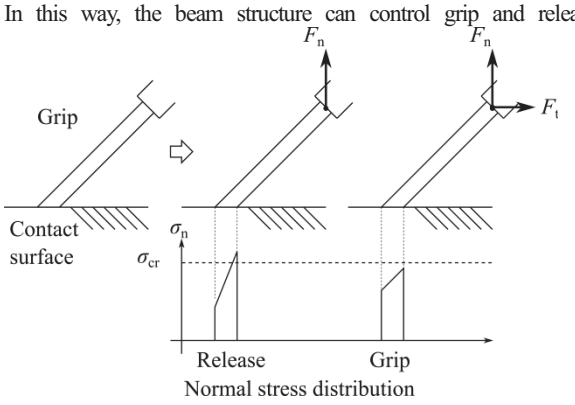

Fig 1 Grip and release mechanism

Correlation between F_t and F_n about gripping area is expressed as Fig.2.[8] In Fig.2, l is length, d is diameter and θ is slant of beam. S is area and Z is the section modulus of contact surface. F means resultant of F_t and F_n and φ is angle between vertical and resultant.

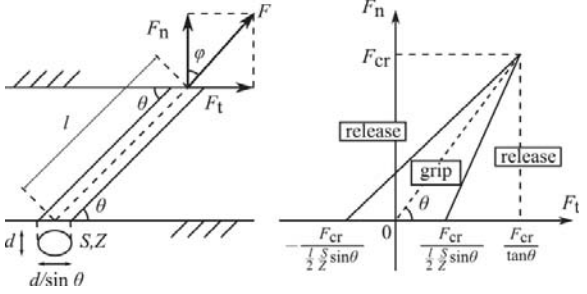

Fig 2 Correlation between F_t and F_n

3. Making Prototype and Measurement of gripping area

3.1 Large adhesion force by absorbing surface roughness

Wide real contact area cause large adhesion force. If contact surface has a roughness, contact area and adhesion force will be declined. But beam structure enables to absorb surface roughness by deformation as shown Fig.3 and gets wide real contact area. Deformation causes internal stress that disturbs adhesion force. So the structure is made up of slanted and soft beams that is easy to absorb surface roughness and generates large adhesion force.

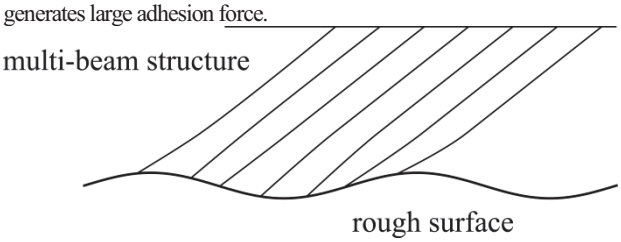

Fig 3 Absorb surface roughness

3.2 Process of making

Based on theory of multi-beam structure considered above, prototype was made as slanted and soft beams. Beams were made of nitinol wire that had super elasticity for repeatedly use.

The following illustration as shown Fig 4 is process of making.

1. Line the wires at equal space and put them between cupper and tin sheet and fix them by pressure welding.
2. Polish the tops of them and make same plane

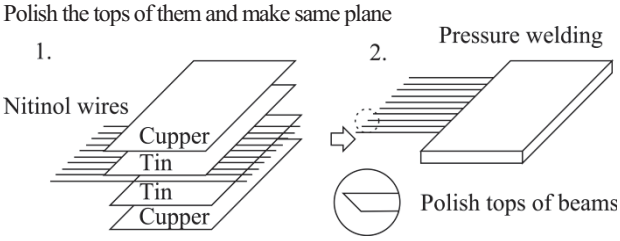

Fig 4 Process of making

3.3 Method of measurement of gripping area

Fig.5 shows schematic illustration of experiment system. Because balance can measure vertical force, adhesion force was measured as F by vertical displacement in condition that structure contacted tilting table. Experiment was carried out as following condition in Table.1 and following process.

Number of beam	10
Angle of beam to surface θ	45(deg)
Length of beam l	1.2(cm)
Diameter of beam d	0.10(mm)
Thickness of sheet	0.5(mm)
Angle of tilting table φ	5 to 65 (deg)each 5(deg)
Speed of displacement	1 μm/sec
Resolution of displacement	1μm
Resolution of balance	1mgf

Table.1 Condition of experiment

Urethane sheet 0.5mm thick as adhesives was pasted on tilting table. Parallel between tops of beams and contact surface was judged by visual observation through microscope.

Vertical 1μm displacement away from the tilting table at contact point and 9 seconds wait were repeatedly applied to the structure at contact point. Contact point was defined as the point when measured value of valance was changed obviously by displacement approaching to tilting table.

The value was declined by drawing up. Change of the value was regarded as force that structure generated to contact surface. And the

point of the maximum absolute value was regarded as the detachment point.

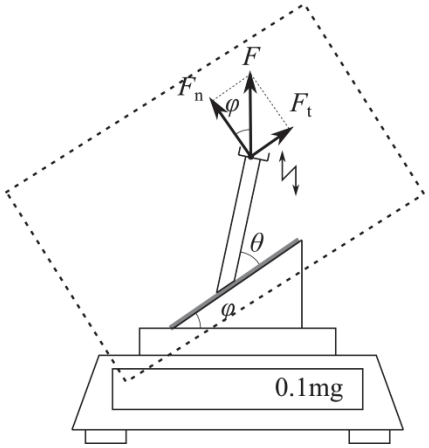

Fig .5 System of experiment

4. Consequence of Experiment

The experimental and theoretical consequences of gripping area between F_t and F_n are shown in Fig 6.□ is the detachment point in experiment. Each points are calculated from measured F and angle φ. And dash lines are theoretical consequence calculated from each elements and average of $F_{\varphi=45}$. The theoretical gripping area is narrow as 1% of experimental consequence.

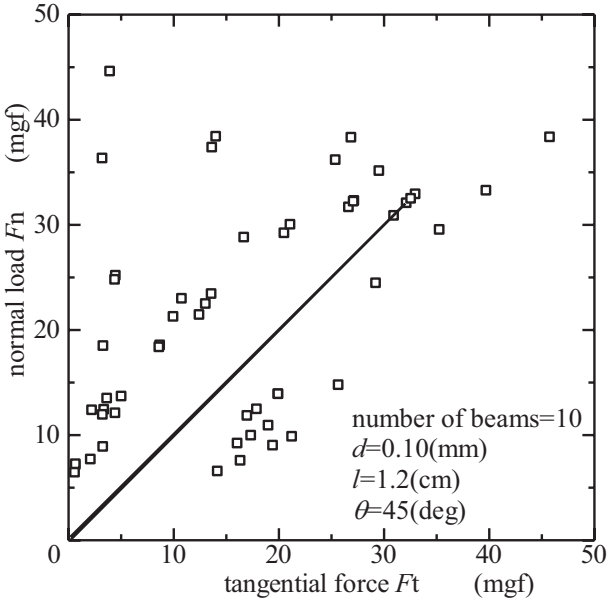

Fig.6 Gripping area between F_t and F_n

3. Discussion

As shown in Fig.6, it can be said that angle of resultant is near 45 degree might be good to grip. For example this structure can grip 20mgf weight applying tangential force between about 15mgf to about 25mgf and it can release applying tangential force under about 15mgf or over about 25mgf. That is to say multi-beam structure can control grip and release by applying tangential force.

It can be said that theoretical and experimental consequence have similar tendency that this structure may be good to grip applying F in the direction of beam axis. Theoretical gripping area is too narrow to control, on the other hand experimental gripping area may be enough to control. It is suspected that there is another criterion of adhesion crack. Causes that affect the criterion are;

1. Shearing force
   By Mieses yield criterion, criterion of adhesion crack may be affected by not only normal stress but shearing stress.
2. Condition of contact
3. Thickness of urethane sheet
   Angle of tilting table causes difference in displacement of distance between tops of beams and contact surface. It means that contact condition is different each time.
   And Watanabe's model is based on beam theory. Thickness of urethane sheet is beyond beam theory.

5. Conclusion

In this study, experiment of grip-release mechanism using multi-beam structure with super elastic wire was carried out. Based on this study, we concluded that slanted multi-beam structure is useful for control grip and release.

The gripping area between tangential force and normal load was investigated the theoretical and experimental consequence. Compared these consequence, we conclude that another criterion of adhesion crack have to be proposed.

Reference

[1]Walker.G. Adhesion to smooth surface by insects a review, Int . J.adhesion and adhesive 13: 3-7.1993.

[2] K.Autumn, W.P.Chang, R.Fearing, T.Hsieh, T.Kenny, L.Liang, W.Zesch, R.J.Full. Adhesive force of a single gecko foot-hair. Nature405:681-685.2000

[3] K.Autumn, M.Sitti, A.M.Peattie, W.Hansen, S.Sponberg, Y.A.Liang, T.Kenny, R.Fearing, J.N.Israelachvili, R.J.Full,. Evidence for van der Waals adhesion in gecko setae. PNAS99(19):12252-12256.2002

[4] K.Takahashi, J.O.L.Berengueres, K.J.Obata, S.Saito. Gecko's foot hair structure and move quickly. International journal of adhesion & Adhesive 26 (2006)639-64

[5]Jun'ichi Watanabe, "Measurement of adhesion force of the structure mimicking gecko foot hair for designing ceiling-walking robot", Tokyo Institute of Technology 2006

[6]Junichi Watanabe,"Effect of stiffness and shape on release mechanism mimicking gecko foot-hair", Tokyo Institute of Technology 2008.

[7]Miaomiao Wang,"Experiment on Prototype of Quick-release Mechanism Using Multi-beam Structure", Tokyo Institute of Technology 2009.

[8]Jun'ichi Watanabe, Kunio Takahashi "Release mechanism Mimicking Gecko Foot-hair",14th symposium on Microjoining and Assembly Technology in Electronics, February 5-6 2008, Yokohama 369-372

Selective Catalytic Reduction of Nitrogen Oxides with Propene over $(Ti,Zr)_2O_4$ catalyst supported by Mo

Student Number: 06-08084 Name: DongIl KIM Supervisor: Hirofumi HINODE, Chris SALIM

1. Introduction

Nitrogen oxides (NO, NO_2 and N_2O) are major sources of atmospheric environmental problems such as photochemical smog, acid rain, ozone depletion and greenhouse effects. Furthermore, presence of nitrogen oxides in the atmosphere can cause problems to human health. Most of the NO_x comes from automobiles (48.5%) and power plants (46.2%) using fossil fuels [1].

Nowadays, three-way catalysts (TWC) are generally used to reduce NO_x in automobiles. This method can reduce NO_x with high efficiency at specific air to fuel (A/F) ratio. However, the development of lean-burn engines that have higher fuel economy and cleaner emissions requires catalyst for NO_x reduction that can function also at higher A/F ratio which cannot be achieved using TWC only. One potential method to reduce NO_x in exhaust gas is selective catalytic reduction of NO using hydrocarbon as reducing agent (HC-SCR of NO) [2]. Previous study showed that TiO_2 supported Mo catalyst was effective in SCR of NO [3]. Another study reported that, TiO_2-ZrO_2 composite used as support material exhibited higher catalytic activity towards HC-SCR of NO when compared to bare TiO_2 [4].

Therefore, in this study, the catalytic activities of $(Ti,Zr)_2O_4$ supported Mo catalysts prepared by two different methods, impregnation (IM) and manual mixing (MM), were investigated for HC-SCR of NO_x using propene as reducing agent.

2. Experimental

$(Ti,Zr)_2O_4$ catalyst was prepared by co-precipitation method using $Zr(NO_3)_2.2H_2O$ (Wako) and $[(CH_3)_2CHO]_4Ti$ (Wako) as precursors with the same molar ratio for Ti and Zr [4]. First, $Zr(NO_3)_2.2H_2O$ was dissolved in 35 ml deionized water with continuous stirring and the pH was controlled by addition of HNO_3 (pH=0.5-1.0). Then $[(CH_3)_2CHO]_4Ti$ was added to the solution and the pH was changed by addition of NH_3 solution (pH=9-11). The resulting mixture was filtered, dried at 100℃ for 8 h and calcined at 550℃ in air for 4 h.

In the case of IM method, $(NH_4)_6Mo_7O_{24}.4H_2O$ (Wako) was dissolved in 50 ml of deionized water and mixed with $(Ti,Zr)_2O_4$. Then the mixture was stirred at room temperature for 12 h and dried at 80℃ for 12 h. The catalyst prepared by IM method was designated $Mo/(Ti,Zr)_2O_4$.

In the MM method, Mo precursor used in IM method was calcined first at 400℃ prior to mixing with $(Ti,Zr)_2O_4$ prepared earlier. The mixing was carried out by hand using a mortar and pestle with a little amount of ethanol. All prepared catalysts were calcined at 550℃ in air for 4 h. Finally, the catalysts were crushed and sieved to 0.71-1.00 mm [4]. The catalyst prepared by MM method was designated MoO_3+$(Ti,Zr)_2O_4$

The SCR activity experiments were carried out in a fixed-bed flow reactor. The reactant gas was composed of 1500 ppm NO, 10% O_2, 1500 ppm C_3H_6 and He as a balance gas. 0.8~1.2 g catalyst was used with a corresponding space velocity of 13000 h^{-1} and a total gas flow rate of about 4 mL/s. The temperature was changed stepwise from 150℃ to 550℃.

NO and NO_2 concentration were analyzed by NO_x analyzer (Shimadzu, NOA-7000). N_2O, CO_2 and CO were analyzed by gas chromatograph (GL Science, GC-323w for N_2O; GL Science, GC-390 for CO_2 and CO). The catalysts were characterized by TG-DTA, XRD, N_2 adsorption (Autosorb 1MP/TSU, BET analysis) and SEM-EDS.

3. Results and discussion

Figure 1 shows the conversion of NO to N_2 over TiO_2, ZrO_2, MoO_3, $(Ti,Zr)_2O_4$ catalysts. $(Ti,Zr)_2O_4$ catalyst shows the highest activity at 450℃ among all the

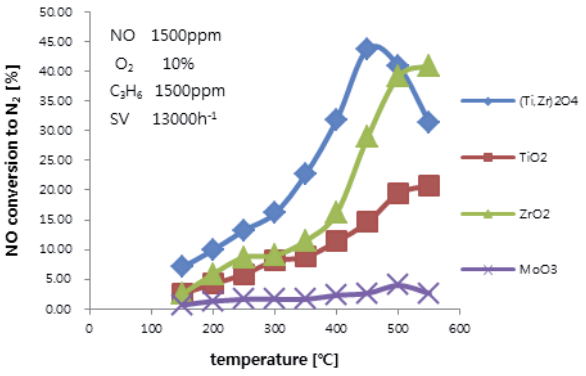

Fig.1. Catalytic activity of TiO_2, ZrO_2, MoO_3, $(Ti,Zr)_2O_4$ for the reduction of NO to N_2 using C_3H_6 as a reductant.

catalysts followed by ZrO_2 and TiO_2 while MoO_3 showed the lowest conversion to N_2.

Figure 2 shows the conversion of NO to N_2 over $Mo/(Ti,Zr)_2O_4$ catalyst by IM method with Mo loading levels from 0-30 wt.%. Metal loaded catalyst showed lower catalytic activity than unloaded $(Ti,Zr)_2O_4$ catalyst. It is possible that the addition of Mo metal on the $(Ti,Zr)_2O_4$ support by IM method reduced the exposed surface of $(Ti,Zr)_2O_4$ available for reaction thus reducing its catalytic activity [3].

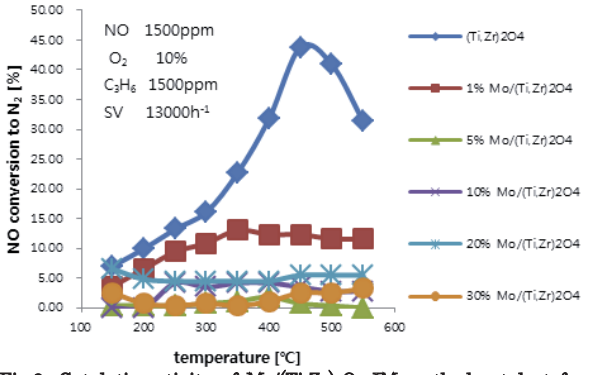

Fig.2. Catalytic activity of $Mo/(Ti,Zr)_2O_4$ IM method catalyst for the reduction of NO to N_2 using C_3H_6 as a reductant.

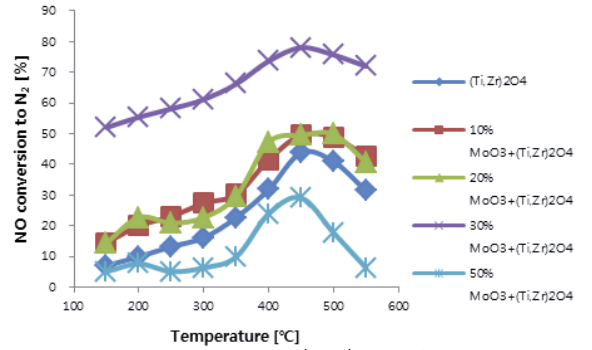

Fig.3. Catalytic activity of $MoO_3+(Ti,Zr)_2O_4$ MM method catalyst for the reduction of NO to N_2 using C_3H_6 as a reductant.

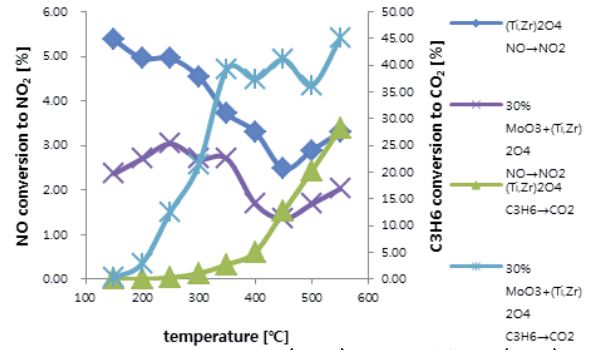

Fig.4. Catalytic activity of $(Ti,Zr)_2O_4$, $30\%MoO_3+(Ti,Zr)_2O_4$, catalyst for the conversion of NO to NO_2 and C_3H_6 to CO_2 using C_3H_6 as a reductant.

Figure 3 shows the conversion of NO to N_2 over $MoO_3+(Ti,Zr)_2O_4$ catalysts by MM method with Mo loading levels from 0-50 wt.%. Catalyst with 30% MoO_3 showed the highest catalytic conversion at 450℃ followed by 10% and 20%. However, further increase of Mo loading to 50% showed a decrease in activity as compared to the bare $(Ti,Zr)_2O_4$ catalyst.

Figure 4 shows the conversion of NO to NO_2 and the conversion of C_3H_6 to CO_2 using the $(Ti,Zr)_2O_4$ and 30% MM method $MoO_3+(Ti,Zr)_2O_4$ catalysts. Addition of 30%Mo by MM method increased the conversion of C_3H_6 to CO_2 while decreasing the conversion of NO to NO_2. This suggested that addition of Mo improved the selectivity of NO reduction to N_2 as shown in Figure 3.

It was reported by Ch. Fountzoula et al.[3] that addition of MoO_3 to bare catalysts improves its mechanical strength through chemical and structural promoters which enlarges the temperature window of the SCR reaction [3]. The synergistic effects could also be observed in the result of this study seen between MoO_3 and $(Ti,Zr)_2O_4$.

4. Conclusions

The catalyst prepared MM method $MoO_3+(Ti,Zr)_2O_4$ catalyst showed catalytic activity towards selective catalytic reduction of NO to N_2 with C_3H_6 as reducing agent. Compared to the IM method, catalyst prepared by MM method exhibited higher catalytic activity. The catalysts prepared by MM method showed optimum ratio of Mo addition at 30%. It is possible that MoO_3 high oxidation ability improved the catalytic activity of $MoO_3+(Ti,Zr)_2O_4$ as suggested by previous study.

References

[1] Norio Arai Techno-System Corp (1997)
[2] R.Burch, T.C.Watling, Appl.Catal.B, 11, 207 (1997)
[3] Ch.Fountzoula et al. Appl, Catal. B, 35, 295 (2002)
[4] Yang Wang; Master Thesis, Tokyo Institute of Technology (2010)

A study the decompositon of nitrous oxide over TiO_2-CeO_2 catalysts

Student Number: 06B20850　Name: Yutaro FUKUCHI　Supervisor: Hirofumi HINODE

1. Introduction

Nitrous oxide (N_2O) is one of the powerful greenhouse gases. Global warming potential per molecule of N_2O is about 300 times that of carbon dioxide (CO_2) [1]. Moreover, it is very stable and has a lifetime of more than 100 years in the atmosphere. N_2O is also identified as a contributor to the destruction of ozone layer in the stratosphere. Although the major sources of N_2O are agricultural byproducts and biomass burning [2], the industrial sources of N_2O such as production of adipic acid, combustion process and automobiles have been increasing [2]. Therefore, the decomposition of N_2O at these industrial sources is important from the environmental point of view.

In our laboratory, activity of the rutile structure titania (TiO_2) for the decomposition of N_2O had been studied, and had shown better activity than that of the anatase structure [3]. And previous study reported that the addition of CeO_2 improved catalytic activity of Nb/TiO_2 catalysts during selective catalytic reduction of nitrogen oxide in the presence of hydrocarbon [4].

In this research, the decomposition of N_2O over manually mixed TiO_2-CeO_2 catalysts was investigated.

2. Experimental

2.1 Catalyst preparation

TiO_2-CeO_2 catalysts were prepared by manual mixing method. Two types of TiO_2 (Toho-1 and Toho-3, Toho Titanium Co.) and two types of CeO_2 (JRC-CEO-1, Santoku Co. and JRC-CEO-2, Daiichi Kigenso Co.) were used. The characteristics of each TiO_2 and CeO_2 were shown in Tabel 1, 2.

During preparation, TiO_2 was mixed with CeO_2 manually in a mortar using small amount of ethanol for better mixing. Then the sample was calcined for 5 hours at 600℃ under air flow.

Table 1 Characteristics of each TiO_2

TiO_2 No.	Surface area [m^2/g]	Particle size [μ m]	Rutile content [%]
Toho-1	32.8	≦0.42	93.3
Toho-3	73.8	≦3.48	95.0

Table 2 Characteristics of each CeO_2

CeO2 No.	Surface area [m^2/g]	D50 [μm]	Purity [%]
JRC-CEO-1	156.9	21.31	99.99
JRC-CEO-2	123.1	4.36	99.97

In order to reduce the pressure drop, the sample was finally pelletized, crushed and sieved into sizes between 0.71 mm to 1.00 mm.

The following nomenclatures for the catalyst samples are used: TiO_2 x-CeO_2 y (a:b) where x and y represent each reference oxide number, and (a:b) means TiO_2:CeO_2 molar ratio. (e.g. $TiO_2$①-$CeO_2$①(1:2) means Toho-1 and JRC –CEO-1 were mixed under TiO_2:CeO_2=1:2 molar ratio).

2.2 Catalytic activity experiment

The catalytic reaction was carried out in a fixed-bed flow reactor under atmospheric pressure. The reactant gas was prepared by mixing N_2O, O_2 and He as a balance gas. Then the mixed gas of 1000 ppm N_2O, 0 or 10% O_2 and He was fed to the catalyst at a flow rate which corresponded to a space velocity of $16000h^{-1}$.

Gas chromatography (GC323w; GL Science Co., with Porapak N, Porapak Q and Molecular Sieve 13X column) was used to analyze N_2O, N_2 and O_2.

2.3 Catalyst characterization

Characterization of catalyst was performed by X-ray Diffraction (MultiFlex), and Scanning Electron Microscope (JSM-5310LV)-Electronic Data Systems (JED-2140).

3. Result and discussion

Figure 1 shows the catalytic activity results of all combinations of TiO_2-CeO_2 at same molar ratio (1:1) for the decomposition of N_2O to N_2 without O_2. Compared to bare TiO_2 (Toho-1, 3) which only decomposed 48% and 45% N_2O at 700 ℃, mixing of CeO_2 improved catalytic activity. And this result shows that JRC-CEO-1 improved catalytic activity better than JRC-CEO-2. Especially, $TiO_2$③-$CeO_2$① (1:1) catalyst decomposed N_2O 100% at 650℃.

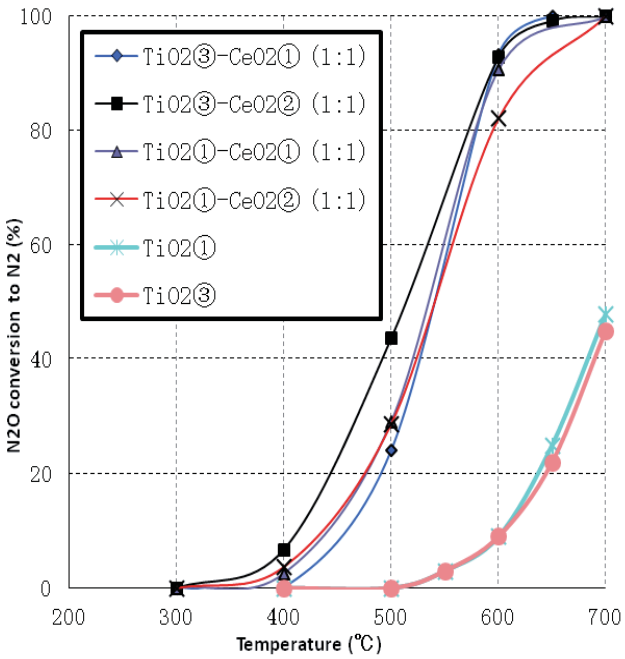

Fig. 1 The effect of mixing of CeO_2 on catalytic activity for the decomposition of N_2O to N_2 without O_2.

Figure 2 shows the catalytic activity result of different molar ratio of $TiO_2$③-$CeO_2$① for the decomposition of N_2O to N_2 without O_2. The catalytic activity of $TiO_2$③-$CeO_2$①(9:1) and $TiO_2$③-$CeO_2$①(1:9) were lower than that of $TiO_2$③-$CeO_2$①(1:1). Particularly, for catalyst with higher molar ratio of TiO_2, the catalytic activity decreased considerably.

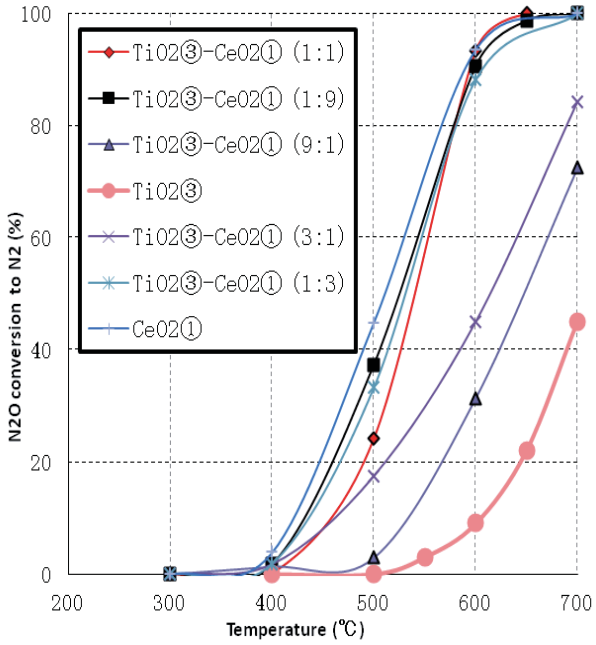

Fig. 2 The effect of molar ratio of $TiO_2$③:$CeO_2$① on catalytic activity for the decomposition of N_2O to N_2 without O_2.

4. Conclusions

Mixing of CeO_2 into TiO_2 improved catalytic activity of bare TiO_2. TiO_2 ③ -CeO_2 ① (1:1) showed the best catalytic activity with the N_2O decomposition achieving 100% at around 650℃.

References

[1]FAO, Livestock a major threat to environment (29 Nov.2006.)

[2] U.S. Emissions Inventory 2010: Inventory of Greenhouse Gas Emissions and Sinks: 1990-2008

[3]K.Yanagida, Master thesis, Tokyo Institute of Technology(2006)

[4]M.Makii, Master thesis, Tokyo Institute of Technology(2008)

Employment data analysis and Relationships of employment support in Tokyo Institute of Technology

Student Number: 07-15526 Name: Akihito TAKANASHI Supervisor: Yukihiko YAMASHITA

1 Introduction

In general, the employment situation of Tokyo Institute of Technology (Tokyo Tech) is better than that of other average public university. However, the rate of passing the interview for Tokyo Tech students falls because of the deterioration of the employment situation in Japan called the secondary employment ice age in recent years.

In addition, students have many problems. Such as the starting time to seek job gets early, they have too much information, and the supports for job hunting are very different among faculties and departments.

In this paper, I clarify the current problems of job hunting in Tokyo Tech, and propose suggestions to improve employment support in Tokyo Tech. This thesis will submit to Department of Academic Affairs where various data are provided.

2 The current state of job hunting

In this section, we show the two axises of the current status of job hunting, in Japan and in Tokyo Tech.

Ratio of job offers to job seekers graduated in March 2011 was 1.28. And students who had appointed job in Feb. To the all in March 2011 is 0.774. Then, about 20 percent college students couldn't get an offer, and graduated from college.

In Tokyo Tech, 33 undergraduate students,125 master course students, and 122 doctor course students graduated without a job offer.Until twenty years ago, a recommendation from Tokyo Tech is equal to a job offer. However, recently the recommendation is equal to pass of the first interview. With the change of human resources that companies seek, they change the interview points from impression to conpetency .

Characteristics of competency interview is that they demand to submit a self-PR statement, called the entry sheet (ES). And they judge the competency from interview with his ES. The general flow of the current recruitment is as follows, 1) Submission of ES and WEB TEST, 2) Group discussion, 3) Personnel interview, 4) Director interview, and 5)Officer interview.

3 Actual conditions of employment support

Purpose of this paper is proposing suggestions to employment support in Department of Academic Affairs to improve their job hunting supporting environment. Therefore, in this section, I analyze the status of employment support in Japan and Tokyo Tech.

In general, employment support consists 1) Community support to meet people and companies, 2) Career plan support, and 3) Support for anti-selection. There are several community supports to meet workers and companies, such as society exchange meeting with the OB, visit to OB, corporate seminars, joint seminars, and so on. Career plan support consists of support for self-analysis seminar, career counseling, and course way of working. Support for selection consists of literally, ES, WEB test measures, group discussion (GD), and interview. This section introduces several typical companies that support employment, and explain the trend of employment support.

I explain organizational structure and support in the university, the contents of each support. And I provide the problems of employment support in Tokyo Tech.

4 Employment performance data analysis in Tokyo Tech

At first, I introduce analysis methods of statistics and economics. Next, I show the result of analysis of employment data and the current state of employment support. Finally, I propose a strategy to conduct employment assistance of students for Academic Affairs in Tokyo Tech. I use the GPL software called weka for the analysis mainly. According to the weka, features are extracted from the data. I verify the relationship between the result of analysis and the problems described in Section 3. In addition, organize new the state from Section 2 and Section 3 using an economic analysis of the Strength weakness Opportunity Threat (SWOT) analysis, the Customer Competitor Company (3C) analysis, and Political Economic Social Techno-

logical (PEST) analysis, I suggest the direction of the job hunting support for depertment of academic affairs which they should focus on. (table.1)

5 Conclusion

In the current employment support, there are differences in the mechanism that connects to the OB and companies by departments. It has been strongly affected to job hunting.

I propose to construct an environment which makes easy to seek jobs as a student in Tokyo Tech. Concretely we have to produce seminars in Tokyo Tech not to go to extra seminars to devote time to research, make cooperation stronger among job hunting support offices of departments, and among OB associations.

References

[1] Career Support at Tokyo Tech, "Research of employment situation, Tokyo Institute of Technology Graduation , (2009, 2010, 2011)

[2] Career Support at Tokyo Tech, Employment guidebook, Tokyo Institute of Technology , (2011, 2012, 2013)

[3] Junji TODA (2011) , College Graduates Job Opening Survey (Graduated 2012), Recruitment Trend, http://bit.ly/9B2S1F

[4] Ministry of Health, Labour and Welfare Press release material, "Survey of Employment appointed students, will graduate universities, etc." http://bit.ly/xoS6EK (17,Jan,2012)


```
=== Classifier model (full training set) ===

J48 pruned tree
------------------

内定先 = 鉱業：化学工学 (1.0)
内定先 = 建設業：人間環境システム (68.0/53.0)
内定先 = 食料品・飲料・たばこ・飼料：生物プロセス (23.0/16.0)
内定先 = 繊維工業：機械制御システム (2.0/1.0)
内定先 = 印刷・同関連業：生物プロセス (21.0/18.0)
内定先 = 化学工業・石油・石炭製品：有機・高分子物質 (168.0/146.0)
内定先 = 鉄鋼業・非鉄金属・金属製品：材料工学 (49.0/34.0)
内定先 = はん用・生産用・業務用機械器具：機械制御システム (30.0/26.0)
内定先 = 電気・情報通信機械器具：機械制御システム (244.0/224.0)
内定先 = 電子部品・デバイス・電子回路：物理電子システム創造 (52.0/45.0)
内定先 = 輸送用機械器具：メカノマイクロ工学 (111.0/101.0)
内定先 = その他製造業：機械制御システム (87.0/80.0)
内定先 = 電気・ガス・熱供給業・水道業：電気電子工学 (36.0/30.0)
内定先 = 情報通信業：計算工学 (156.0/134.0)
内定先 = 運輸業・郵便業：情報環境学 (32.0/26.0)
内定先 = 卸売業・小売業：材料物理科学 (10.0/9.0)
内定先 = 金融・保険業：経営工学 (53.0/43.0)
内定先 = 不動産業・物品賃貸業：人間環境システム (3.0/1.0)
内定先 = 医療・福祉：人間環境システム (3.0/2.0)
内定先 = 教育・学習支援業：数学 (7.0/5.0)
内定先 = 学術研究・専門・技術サービス業：建築学 (80.0/69.0)
内定先 = 生活関連サービス業・娯楽業：化学環境 (4.0/3.0)
内定先 = サービス業：社会工学 (11.0/8.0)
内定先 = 公務：建築学 (34.0/30.0)

Number of Leaves  :     24

Size of the tree :      25
```

Figure1: Employment performance data analysis in Tokyo Tech

	【strength】 ・Ties with Tokyo Tech OB organization. ・Teaching experience for Tokyo Tech students	【weakness】 ・Poor the latest information of adoption ・The lack of manpower ・Information gap for each department
【opportunity】 ・Built Tokyo Tech Fron ・Start to mailing news ・Demand of SE	・Enhancement of corporate briefing in Tokyo Tech ・Enhancement of social gathering of OB organization ・Send more information of job hunteing by mailing news	・Exchange meeting of the recruiters and university affairs ・Sharing of information for each department by mailing list
【threat】 ・Intervention of external companies ・Social Recruiting ・Delay of starting job hunting to Decmber	・Exclusive of external companies by a Board of OB ・Assistance by Employment Support Division on internet. ・OB introduction via the Internet	・Joint seminars with outside companies

※ SO：Strategies to maximize strength under the opportunity.
ST：Strategies to avoid threats by taking advantage of strength.
WO：Strategies to take advantage of the opportunity by complementing the weakness.
WT：Strategy to prepare for business contraction or retreat.

Table 1: SWOT Analysis Matrix

A Study on the effectiveness of Ecodriving Program on Fuel Economy

Student Number: 07_16282 Name: Ayuka Takeda Supervisor: Yasunori Muromachi

1. Introduction

In order to mitigate global warming, reduction in emissions of carbon dioxide is one of the major issues in several sectors. In Japan, about twenty percent of the emissions are produced by transport sector and about fifty percent of the emissions of the sector are generated by passenger cars. So, how to reduce the emissions from passenger cars is the most important. Ecodriving is one of the measures for reducing the emissions from passenger cars as well as trucks. Recently, the government and some private organizations actively promote ecodriving program, because the effectiveness of the ecodriving program has often been confirmed in preceding studies, and the program requires less investment in infrastructure development. However, while the preceding studies mostly focused on the ecodriving conducted during the program, the studies on the ecodriving in the real-world have not been conducted much.

The objective of this study is to investigate the effectiveness of the ecodriving program in the real-world by monitoring fuel consumption before and after the program and by analyzing whether the participants of the ecodriving program actually practice ecodriving such as idling stop and gentle start in the real-word.

2. Data Collection

In order to collect fuel consumption (FC) data and Global Positioning System(GPS) data, I asked nineteen drivers to take the ecodriving training program and equipped their cars with the calibrate GPS and FC gadgets before and after the program. Both equipments collected instantaneous data per 0.10 second. Data collection process is shown in Figure 1. I collected the FC and GPS data that came from the three days of pretest or normal driving before the training day, and another three days of posttest or ecodriving after the training day. For collecting the driver's trip data, each driver used his or her own car and route freely.

Figure 1 Data Collection Process

By indicating GPS data on GIS road network map and by matching the location with fuel consumption data, I built the dataset containing the information on fuel consumption during stopping and acceleration after the stopping, stopping time mostly due to intersection signals, and acceleration patter after the stopping for each driver. The data on the stopping is used for investigating the practice of idling stop, while the data on the acceleration is used for studying

Level =5(%)	Idling stop	Gentle-start
Improved	B,H,J,K,	B,H,J,K,Q,R,S
Worsened	N,P	
Not significant	C,D,E,F,G,I,L,M,O,Q,R,S,T	C,D,E,F,G,I,L,M,N,O,P,T

Table 1 The Effectiveness of the Ecodriving Program (B-T indicate each driver's ID)

that of gentle start.

3. The Results of the Analysis

The result of the analysis on the effectiveness of the Ecodriving program is shown in Table 1. In term of idling stop, after the ecodriving program, four out of the nineteen drivers demonstrated reduction in fuel consumption significantly in the real-world. In term of gentle start, seven drivers indicated reduction in fuel consumption significantly. Most drivers were successful in reducing fuel consumption after the program, however, the differences were not statistically significant.

Next, I classified the drivers into the group with large difference, medium difference and small difference. Each group consists of six to eight drivers. Firstly, in the analysis of idling stop, the group with large difference tended to include many female drivers and the group with small difference tended to include many male drivers. In the analysis of gentle start, the tendency was the reverse. Therefore we believe that female drivers practice idling stop, while male drivers practice gentle start more easily.

Second, Figure 2 shows the relationship between the fuel economy improvement during the ecodriving training program and the three groups. In the analysis of idling stop, the group with small difference indicated the largest improvement, while in the analysis of gentle start, the group of medium difference the largest. Therefore, the result of the ecodriving program is not necessarily related with the real-world practice of ecodriving.

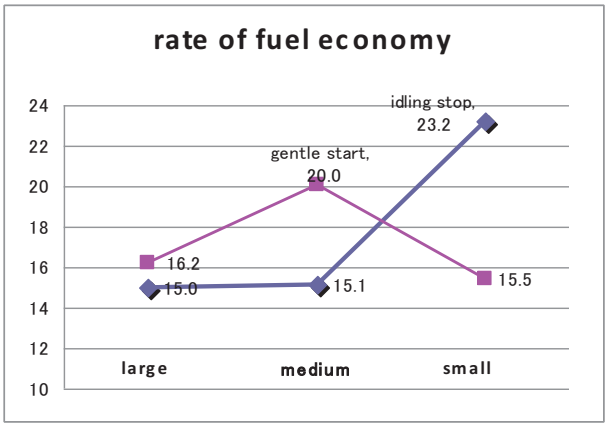

Figure 2 Fuel Economy during the Ecodriving Program and that in the real-world

4. Conclusions

In this study, I investigated the effectiveness of the ecodriving program in the real-world by monitoring fuel consumption before and after the program. According to the results, four out of the nineteen drivers practiced idling stop, while seven conducted gentle start. I also found that female drivers practiced idling stop, while male drivers practiced gentle start more. The relationship between the fuel economy during the ecodriving program and that in the real-world was not so clear.

Reference

1) Changxu, Wu.,Guozhen., Zhao., and Bo,Ou.,2011. A Fuel economy optimization system with applications in vehicles with human drivers and autonomous vehicles. Transportation Research Part D, 16,515-524

2) Kenji Mori and Hiroshi Makishita, 2010. Effectiveness of ecodriving at the time of congestion. Journal of civil planning, Vol.27 No.5, 935-940

Effects of Temperature and Solution Type on Corrosion Behavior at Acceleration Test of Paint-coated Steel Plate with Defect

Student Number: 07-29586 Name: Kenji Wada Supervisor: Nobuaki Otsuki

1. Introduction

Considering economic aspects, there is high demand for methods of estimating life span of real structure. For this purpose, acceleration test has been taken in the past studies.

In this study, offshore structure is focused on. Offshore structures consist of paint-coated steel material and corrosive deterioration is main problem. Especially, macrocell corrosion due to defect of paint surface causes serious problem.

There are two goals in this study.

1) To know about effects of environmental factors (temperature and oxygen concentration) on corrosion of paint-coated steel plate with paint defect.

2) To build an electrical circuit model for macrocell corrosion.

For goal (1), electrical values (such as current density, resistance, and capacitance) are used to estimate corrosion rate. Furthermore, for goal (2), an electrical circuit model is considered by using data from experiments.

2. Experimental Procedure

2.1. Specimens

To focus on macrocell corrosion, paint-coated steel plates with defect at the center are used. Two types of paintings are used, Oil Alkyd (OA, paint not for marine environment, red, 150μm), Tar epoxy (non-specific chemical substance type) (NTE, paint for marine environment, black, 150μm). A steel plate consists of six divided parts which are connected each other by lead wires (Fig. 1).

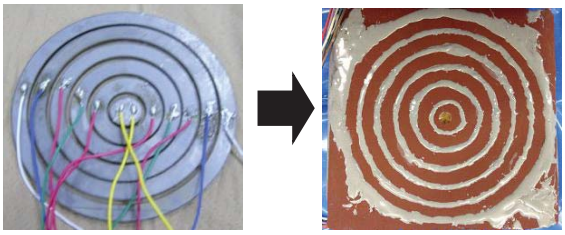

(a) Steel plate (back) (b) Paint coating (front)

Fig. 1 Specimen

2.2. Experiment Setting

(1) Specimens are put into electrolyte (40℃, 3% NaCl) with 4L/min air.

Specimens are arranged inside the container as shown Fig. 2. As time passes, experiments in solution with different temperature are taken as shown in Table 1.

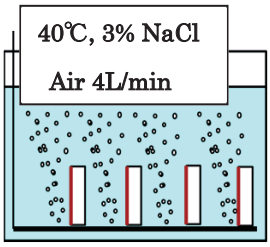

Fig. 2 Immersing Setting

Table 1 Measuring Setting

	O_2 Saturated	High O_2	Low O_2
40℃	①	④	⑤
30℃	②	—	—
20℃	③	—	—

(2) To know the influence of oxygen, concentration of O_2 at electrolyte (40℃, 3% NaCl) is controlled by 3 stages. Specimens with OA are exposed.

2.3. Measurement Setting

Two kinds of electrical measurement are taken with changing temperature and oxygen (Table 1). It is because corrosion is chemical reaction involving corrosion current flow.

(1) AC impedance method for microcell corrosion current

(2)Macrocell corrosion current

3. Result and Discussion

(1) Influence of Temperature on Corrosion at Defect Point

Macrocell and microcell current density became higher at higher temperature.

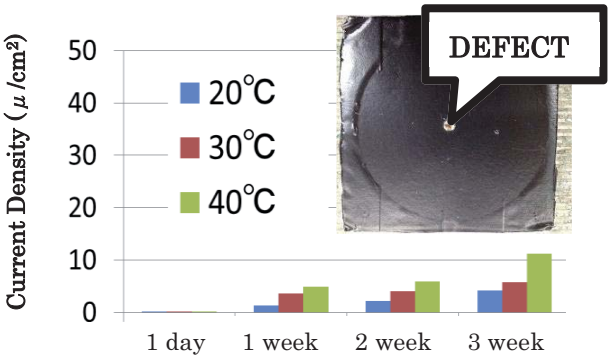

Fig. 3 NTE's Macrocell Current Density at Defect Point (Immersing Temp: 40℃ / Measuring Temp: 20, 30, 40℃)

(2) Influence of Paint Deterioration on Macrocell Corrosion at Defect Point and Comparison (before paint peeling)

As time passed, more current passed through in both of paint type. Besides, decrease of paint resistance happened simultaneously.

Comparing the both result, OA's corrosion rate was much higher than NTE's until OA's paint was broken, and OA's paint resistance was lower than NTE's correspondingly.

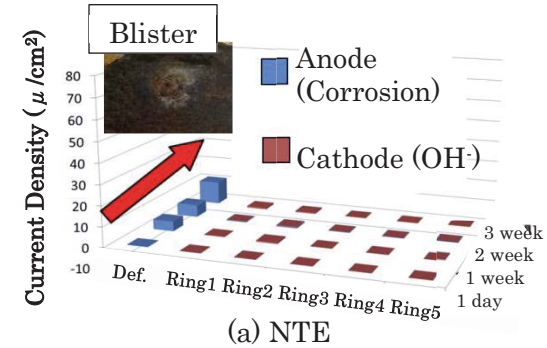

(a) NTE

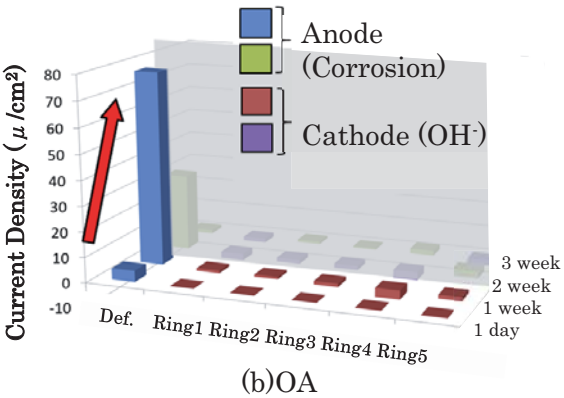

(b)OA

Fig. 4 Macrocell Current Density

(3)Distribution of Paint Deterioration

Inside NTE's specimen, at ring 2, a blister and a strong cathodic tendency were observed. Comparing resistance of this part with ring 5 which kept relatively strong coating, ring2 had lower resistance and was deteriorated harder than ring5.

(4) Influence of Oxygen Concentration

As concentration got higher, corrosion rate also got higher, especially, about microcell corrosion.

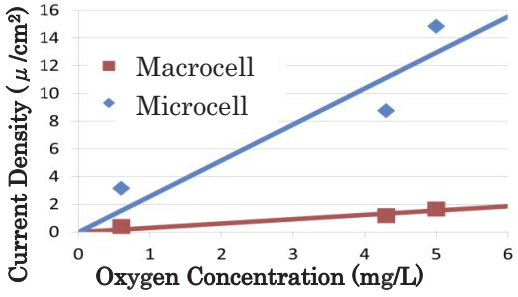

Fig. 5 Current density with different O_2 concentration

(5)Comparison of Experimental Result and Analytical Solution

Fig. 6 shows the analytical model used in this study. From Fig. 7, model and result can match qualitatively.

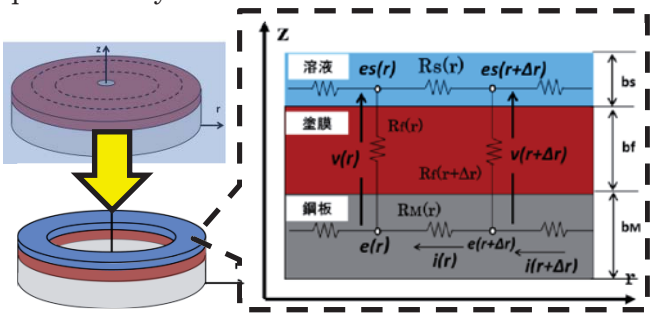

Bessel's equation

$$\frac{d^2v(r)}{dr^2}+\frac{1}{r}\frac{dv(r)}{dr}-ABv(r)=0$$

$$i(r)=-\frac{r}{A}\frac{dv(r)}{dr},\quad A=\frac{1}{2\pi}\left(\frac{\rho_s}{b_s}+\frac{\rho_M}{b_M}\right),\quad B=\frac{2\pi}{\rho_f b_f}$$

Fig. 6 Analytical Model

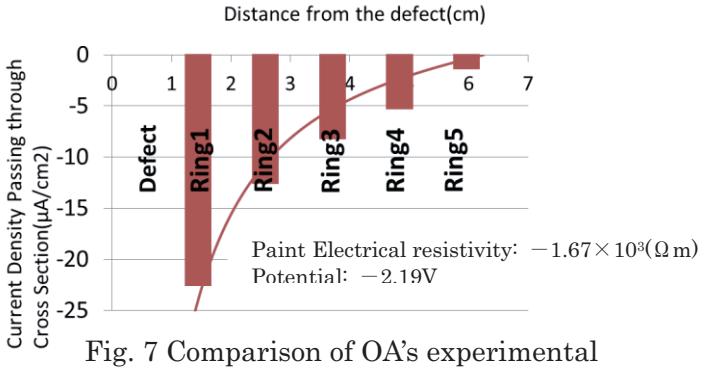

Fig. 7 Comparison of OA's experimental Result with Analytical Solution

4. Conclusion

(1) Macrocell and microcell current density became higher at higher temperature.

As paint deterioration progressed, more current passed through in both of paint type.

Oxygen concentration makes corrosion rate faster, especially, microcell corrosion.

(2) Model and result can match qualitatively.

(Reference)

Committee of Structural Engineering: Guidelines for Evaluation of Durability and Load-Carrying Capacity for Steel Structures under Marine Environment

A study on the operation and maintenance performance of wind power plants owned by public sector in Japan

Student Number：08B06625　　Name：Teppei KATATANI　　Supervisor：Naoya ABE

日本の公共部門による風力発電施設の運営・保守管理体制

片谷 鉄平

1. Introduction

Wind power is one of the prominent renewable energy resources. In Japan, there are 1,814 wind power plants as of March, 2011.[1] However, there are frequent failures and accidents, often resulting in expensive maintenance cost.

About 20% of wind power plants in Japan are operated by the public and third sector; the latter refers to the organizations invested by both public sector and private sector. It is said that about 60% of the plants owned by Japanese public sectors are in financial deficits.[2]

This study focuses on the public and the third sectors which own plant in Japan, especially with emphasis on their performance in operation and maintenance.

2. Objectives

There are three objectives in this study; they are: (1) to clarify a variety of information related to operating wind power plant in public sector, (2) to investigate the influence of the operation and maintenance scheme to the performance of the wind power plant owned by public sector, and (3) to investigate the influence of the operation and maintenance scheme to the frequency of failure and accidents in public sector.

3. Data & Method of Analysis

Table 1 shows the category of the data collected and their sources and details. The sources of the data are mainly the reports by NEDO and by *Hokkaido Sangyo Hoan Kantoku-bu,* and the questionnaire survey that was conducted by the author.

Two methodologies are used for the analysis: survival analysis for the objective (2) and multiple regression analysis with dummy variables for the objective (3).

Table 1：Data for analysis

Category of data	Sources & details
Operation and maintenance scheme in public sector (Frequency of the scheduled maintenance, etc.)	Questionnaire survey to municipalities and 3rd sectors operating wind power plants and selling electricity. (Sample number 67, Respondents 36)
Information of failures and accidents	The reports by NEDO and *Hokkaido Sangyo Hoan Kantoku-bu* (April 2004 ~March 2011), and questionnaire survey (April 2008 ~ March 2011)
Other information (Wind speed, usage period of wind power plant, etc.)	NEDO's map of wind condition anddatabase of wind power plants.

4. Result

4−1. Summary of the questionnaire survey

A questionnaire survey was conducted from Nov, 30, 2011 to Jan, 27, 2012. 67 questionnaires were sent to all plant operators which are in either public or third sectors selling electricity generation and 37 questionnaires were collected (collection rate: 55%.) Among the 37 respondents, 34 were municipalities operating 91 plants and the remaining 3 were the organizations in the third sectors operating 30 plants.

Figure 1 and 2 show the parts of the summary of the survey. With respect to the frequency of scheduled maintenance, 34 plants had it once per year while 54 plants had it twice annually and 23 plants had ad-hoc basis. Distribution of capacity factor, which is the ratio of actual electricity generation divided by the potential generation and is commonly used as an indicator to evaluate the performance of the plants, is shown in Figure 2. Mean value of the capacity factors among the subjects was 15.4%.

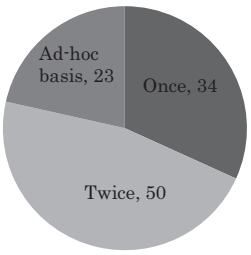

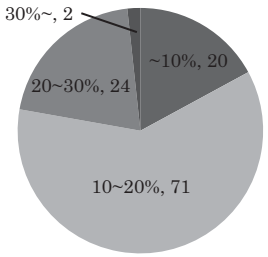

Figure 1(Left)：The frequency of the scheduled maintenance per year between April 2008 and March 2011
Figure 2(Right)：Distribution of capacity factor

4−2. Survival analysis

Firstly, the difference of the survival rates of the plants between those operated by public sectors and non-public sectors in Hokkaido was examined. When survival rates of a certain sample group are lower than those of other groups, then the first group is understood as suffering more accidents and troubles.

Figure 3 shows the result of the analysis, where wind power plants owned by public sectors indicate low survival rates almost consistently compared to those rates owned by non-public sectors. The figure implies that the performance of the plants owned by public sector is inferior to the performance of the plants owned by the non-public sectors.

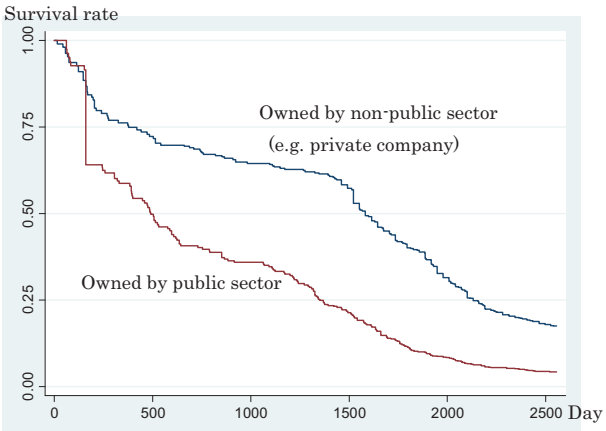

Figure 3：The result of Survival analysis of the plants in Hokkaido

Secondly, the influence of the frequency of the scheduled maintenance to the survival rate of the public sector plants was considered. Figure 4 shows the result and Table 2 shows some statistics of each group classified by the maintenance patterns. From Figure 4 and Table 2, low survival rates of plants which had scheduled maintenance twice per year compared to others that do not depend on the frequency of scheduled maintenance. Some public sectors conducted it twice assumedly because of frequent failures. In fact, average annual operating time of the plants with scheduled maintenance twice per year group is longer than the times of the other two groups by almost 700 to 1,100 hours. In addition, the capacity factor of the plants with scheduled maintenance twice per year group is higher than the values of the other two groups by almost 5%.

Table 2：Some statistics of each group
(Through April 2008 to March 2011)

Valuable	Frequency of annual scheduled maintenance		
	Once	Twice	Ad-hoc basis
Number of wind power plants	34	50	23
Total number of failures and accidents	96	200	89
Average annual operating time [hours]	6,567 sd(2,010)	7,237 sd(1,292)	6,336 sd(2,174)
Average annual capacity factor [%]	12.63 sd(4.64)	17.05 sd(6.49)	12.35 sd(6.32)

※Failures and accidents happened through April 2004 to March 2011.
※sd：standard deviation

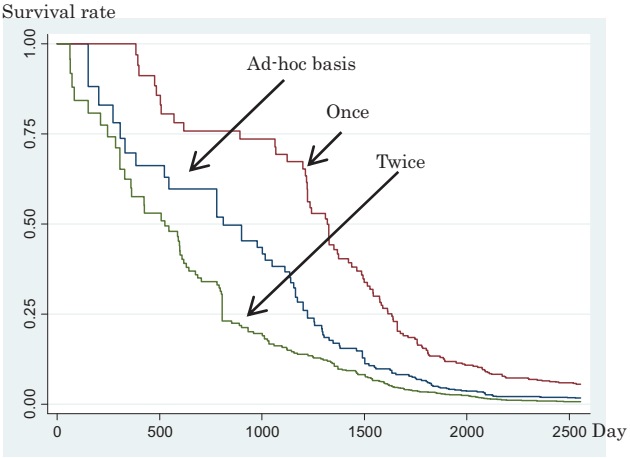

Figure 4：The result of survival analysis of the plants in public sector classified by the maintenance patterns

4−3. Regression analysis

The following regression analysis was conducted by least squares method where the dependent variable is capacity factor (number of samples = 104).

$$y_i = \beta_0 + \beta_1 x_{i1} + \beta_2 x_{i2} + \beta_3 x_{i3} + \beta_4 x_{i4} + \beta_5 x_{i5} + \beta_6 x_{i6} + \varepsilon_i$$

y ：*Capacity factor of wind power plant* [%]
x_{i1}：*Annual average wind speed at* 30m [m/s]
x_{i2}：*Altitude of the base of the wind power plant* [m]
x_{i3}：*The number of months of operation until April* 2011[*months*]
x_{i4}：*Using remote monitoring system* [0 or 1]
x_{i5}：*Conduct scheduled maintenance once/year* [0 or 1]
x_{i6}：*Conduct scheduled maintenance twice/year* [0 or 1]
ε_i ：*Error term* (assumed as normally distributed)

where β_0 is constant and β_k $(k = 1,2,3,4,5,6)$ are coefficients of the explanatory valuables. The option of using remote monitoring system and the frequency of scheduled maintenance are expressed as dummy valuables. If $x_{i4} = 0$, it means remote monitoring system is not used by the plant(i). And if $x_{i5} = x_{i6} = 0$, it means scheduled maintenance was conducted ad-hoc basis year by year.

The result of the regression analysis is the equation below.

$$\hat{y}_i = -18.31^{***} + 5.19^{***} x_{i1} - 0.006^{**} x_{i2} - 0.016 x_{i3} + 4.74^{**} x_{i4} - 3.63^{**} x_{i5} + 3.45^{**} x_{i6}$$

$$\text{Adj } R^2 = 0.415, \quad F \text{ value} = 13.18^{***}$$

Significance levels: ＊10% ,＊＊5% ,＊＊＊1%

The results show that capacity factor is explained by wind speed (positive effect), location (negative effect when an altitude increases), and usage period (negative effect). Furthermore, if an operator would conduct the scheduled maintenance twice per year instead of ad-hoc basis, the capacity factor of plants could have increased by 3.45%. And if an operator would introduce remote monitoring system, the capacity factor could have increased by 4.74%.

5. Conclusion

From the results of analysis above, the following conclusions are obtained.

In terms of survival rate, the performance of plants owned by public and third sectors is inferior to the performance of those owned by non-public sectors. In addition, those plants with twice scheduled maintenance per year constantly indicate lower rates over time compared to those plants with once or ad-hoc scheduled maintenance per year.

However, in terms of capacity factor, those plants which had twice scheduled maintenance show superior performance compared to those which had once or ad-hoc scheduled maintenance.

Thus this study found that lower survival rate does not necessarily mean poorer performance of capacity factor or annual operating time. This study also confirmed that the option of remote monitoring system influences positively on the performance of wind power plants.

As an area of the further study, a cost analysis which focuses on the operation and maintenance scheme would be important to improve the performance of wind power plants.

Reference

[1]NEDO, database “Situation of wind power in Japan”
[2]NHK, News (2010. Nov. 18)

Acid-catalyzed biodiesel production from triolein

Student Number: 08-07783 Name: Xiao HAN Supervisor: Ryuichi EGASHIRA, Hiroaki HABAKI

1 Introduction

Fossil fuels are limited and finite, and the alternative fuel resources have been developed. Biodiesel is attracting an increasing attention and strongly recommended as an alternative diesel fuel because it is renewable. Biodiesel can be produced from renewable biological sources such as vegetable oils and animal fats. Especially inedible vegetable oils such as jatropha oils are recently becoming more attractive because of their environmental benefits. The main content of vegetable oils is triglyceride (TG) and biodiesel is produced by transesterification of the triglyceride. Transesterification is a chemical reaction by triglycerides and alcohol in the presence of a catalyst to form fatty acid methyl esters (FAME) and glycerol. The reaction consists of three consecutive reversible steps, such as the conversion of TG to diglyceride (DG), that of DG to monoglyceride (MG), and that of MG to glycerol. For this reaction a catalyst is usually used for improving reaction rate and shortening reaction time. In the ordinary transesterification process the alkaline catalyst, such as NaOH, is used and some disadvantages of this catalyst have been reported. The vegetable oils originally contain free fatty acid (FFA), causing low productivity of biodiesel and the saponification of the glycerides is also serious. On the other hand an acid catalyst, such as H_2SO_4, is not affected by the presence of FFA and does not saponify FFA and methanol can react to form FAME with the acid catalyst and FFA can be converted to FAME at the transesterification as well. Accordingly it is considered that the pretreatment to remove FFA in the ordinary transesterification process can be reduced by using acid catalyst. However the disadvantage of an acid catalyst was reported to show a slower reaction rate than alkaline catalyst[4]. Therefore this dissertation aims to study the effects of the operational parameters on the acid-catalyzed biodiesel production.

2 Experimental

2.1 Feed oil

The compositions of the jatropha oil are summarized in Table 2.1[4]. Oleic acid is the major component in this oil and triolein was selected as a model feed oil in this study.

2.2 Transesterification

Figure 2.1 and Table 2.2 show the experimental apparatus and conditions in the transesterification. The stirring vessel was employed as a reactor. The specified amounts of triolein, methanol and H_2SO_4 were put in the vessel and the time to start the agitation was defined as the starting time of the reaction. Samples of 0.9ml were taken every 1 hour and then mixed with 1ml of distilled water to stop the reaction. Then the solution was separated into the biodiesel and water phases. TG, DG, MG and FAME contents in the oil phase were determined by using a liquid chromatography. The experimental parameters of the operating temperature, methanol/feed molar ratio, and catalyst/feed mass ratio were changed to study the transesterification reaction in this system.

Biodiesel yield Y was defined by Eq.(1).

$$Y_i = \frac{M_i}{M_{Feed}} \quad (1)$$

Table 2.1 Compositions of the jatropha oil

		mass fraction
Myrstic acid	(C14:0)	0
Palmitic acid	(C16:0)	0.103
Stearic acid	(C18:0)	0.138
Oleic acid	(C18:1)	0.427
Linoleic acid	(C18:2)	0.263
Free fatty acid		0.110

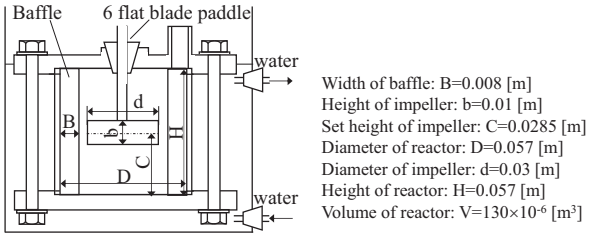

Figure 2.1 Experimental apparatus

Table 2.2 Experimental conditions

Feed			Triolein
Temperature	T	[℃]	40, 60
Methanol/oil molar ratio	n_{MeOH}/n_{Feed}	[-]	12, 24, 30
Catalyst			H_2SO_4
Catalyst/oil mass ratio	$M_{cat.}/M_{Feed}$	[-]	0.01, 0.03, 0.05
Agitating speed	N	[rpm]	600
Reaction time	t	[h]	0~10

3 Results and Discussion

3.1 Effects of experimental conditions on yield

3.1.1 Effect of temperature

Figure 3.1 shows the effects of temperature on yield of FAME. Y increased with the operating temperature from 40℃ to 60℃. However Y decreased from 60℃ to 70℃ because 70℃ was higher than the boiling point of methanol and methanol should have been vaporized. Actually the volume of the solution in the stirring vessel was significantly reduced. Thus the methanol concentration could not be kept enough high to make Y lower.

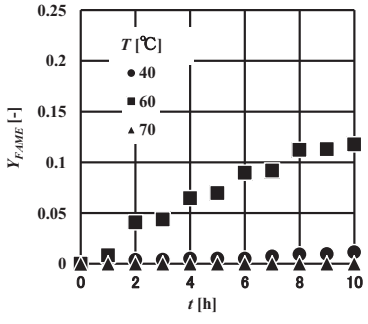

Figure 3.1 Effect of temperature on Yield

3.1.2 Effect of methanol/feed molar ratio

Figure 3.2 shows the effect of n_{MeOH}/n_{Feed} on Y. Y attained 0.205 when n_{MeOH}/n_{Feed} was 30. Higher molar ratio helped FAME to increase in this measurement. However, if too much methanol is used, the concentration of feed will be reduced, which might lead to low reaction rate. Thus, a favorable value of methanol/feed molar ratio must exist and the value should be

of course affected by the other parameters.

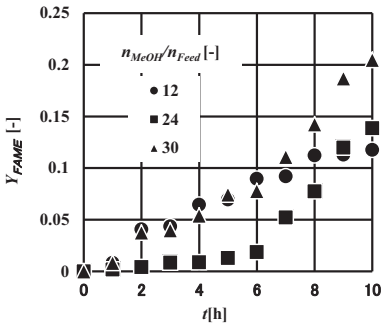

Figure 3.2 Effect of n_{MeOH}/n_{Feed} on Yield

3.1.3 Effect of catalyst/feed mass ratio

Figure 3.3 shows the effect of $M_{cat.}/M_{Feed}$ on FAME's yield. Almost no FAME was obtained when $M_{cat.}/M_{Feed}$ was 0.01. By increasing $M_{cat.}/M_{Feed}$ from 0.01 to 0.03, the yield became much larger. However there was little difference in the FAME's yield when $M_{cat.}/M_{Feed}$ changed from 0.03 to 0.05. Thus excess amount of catalyst don't lead to high yield but a lack of catalyst resulted in a low yield of FAME.

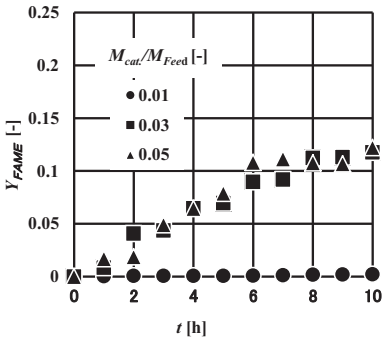

Figure 3.3 Effect of $M_{cat.}/M_{Feed}$ on Yield

3.2 Yield variation of TG, DG, and MG

In the results mentioned above, the effects of n_{MeOH}/n_{Feed} were large and the profiles of TG, DG and MG would be discussed here. Figures 3.4~ 3.6 show the yield variation of TG, DG, and MG when n_{MeOH}/n_{Feed} was changed. Y of TG is almost same in all three cases. Y of TG and DG didn't changed a lot when n_{MeOH}/n_{Feed} was changed, and Y of DG is smaller than MG. It should be noted that the n_{MeOH}/n_{Feed} could have a large influence on the conversion from MG to glycerol and higher n_{MeOH}/n_{Feed} should cause higher Y of FAME.

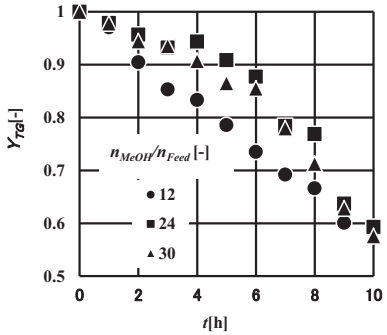

Figure 3.4 Yield of TG

With these considerations the experimental conditions were fixed as T=60℃, n_{MeOH}/n_{Feed}=30 and $M_{cat.}/M_{Feed}$=0.05 to expect high Y of FAME and Y of 0.385 was obtained. It can be speculated that changing the reaction conditions, such as increasing the pressure, reaction time, agitating speed, a higher yield could be obtained.

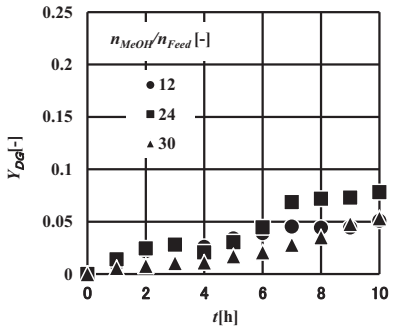

Figure 3.5 Yield of DG

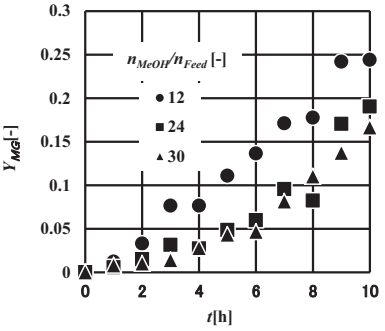

Figure 3.6 Yield of MG

4 Conclusion

FAME can be produced by acid catalyst in a slower reaction rate than alkali catalyst. In the case of acid catalyst, reaction temperature, methanol/oil molar ratio and catalyst/oil mass ratio can affect the yield of FAME.

Higher Y can be obtained by using higher temperature, however, a temperature higher than the boiling point of methanol will cause low Y of FAME due to the evaporation of methanol. Higher molar ratio leads to higher Y effectively. However, the concentration of feed will be reduced and might lead to low reaction rate due to excess amount of methanol. Catalyst mass ratio higher than 0.03 also leads to higher Y but not very obviously.At last, it can be observed that n_{MeOH}/n_{Feed} could have a large influence on the conversion from MG to glycerol.

Experiments using jatropha oils will be needed to confirm the result.

Nomenclature

M	=	Mass	[-]
n	=	Molar	[-]
N	=	Agitating speed	[rpm]
P	=	Purity of product	[-]
t	=	Time	[h]
T	=	Temperature	[℃]
Y	=	Yield	[-]

<Subscript>

cat.	=	Catalyst
Feed	=	Feed
i	=	Component *i*
MeOH	=	Methanol

Reference

[1] Hayashi Tomoki, "Effect of Operating Conditions in Biodiesel Fuel Production from Low-valued Feed", Bachelor Thesis, Tokyo Institute of Technology, 2008

[2]Kotte Sagar Rao· Pradosh Prasad Chakrabarti· B. V. S. K. Rao· R. B. N. Prasad, "Phospholipid Composition of Jatropha curcus Seed Lipids", J Am Oil Chem Soc, 86,197-200(2009)

[3]May Ying Koh, Tinia Idaty Mohd. Ghazi*; "A review of biodiesel production from Jatropha curcas L.oil", Renewable and Sustainable Engery Reviews, 12,2240-2251(2011)

[4] Sinthupinyo Patima, "Comparative Study of Biodiesel Production by Alkaline Transesterification from Low- valued Feed", Master Thesis, Tokyo Institute of Technology, 2007

Crushing sound analysis of snail fossils under compressive loading using audible frequency measurement

Student Number: 08-08073 Name: Shuhei KITAKATA Supervisor: Thirapong PIPATPONGSA

1 Introduction

Many failure mechanisms in brittle materials can produce sound waves due to the crack development and particle crushing. Acoustic emission (AE) has emerged as in-situ techniques to evaluate rock slope stability; however, successful results to predict slope failure are quite few partially because an installed number of AE sensors are not sufficient in the monitoring area. In order to increase number of installment by cost reduction, feasible study on an alternative method using audible frequency measurement is introduced as part of warning system.

Normally, the predominant frequency of sound waves in soil is ranged between 0-40kHz while an audible range is 30Hz-20kHz with best at frequencies between 1-5 kHz for ear's sensitivity. In acoustics, decibel is commonly used to define sound pressure level to a reference value 20 μPa which represents 0 dB for the quietest sound of human hearing threshold in air at 1 kHz. Sound loudness in air can be measured using a microphone and in water using hydrophone.

This research aims to carry out the crushing sound analysis of crushable materials under compressive loading using commercial microphone. Practical applications are planned to carry out at an overseas coal mine. There is a perfect site of coal mine in the north of Thailand where the biggest lignite in the Southeast Asia is deposited. Moreover, a huge bulk of snail fossils were found, therefore the conflict and constraint between energy resource development and geological heritage protection has been arisen. It is expected that a preliminary study of this technique could be useful for alarming damage to fossils.

Fig. 1 Deposit of snail fossils at Mae Moh open-pit lignite mine in Northern part of Thailand

2 Site investigation

The large deposit of snail fossil aging around 12-13 million years has been discovered at Mae Moh open-pit lignite mine in Northern part of Thailand as shown in Figure 1. This snail deposit dominantly composes of freshwater mud snails, named Bellamya, and rare tiny spire snails, Bithynia. Lignite mining at this largest coal mine in the Southeast Asian region is undertaken by Electricity Generating Authority of Thailand (EGAT). The preserved area of snail fossil with layers of up to 12 meters deep in the mining area has been set aside; however, there is a growing concern about influence of mining activities in the vicinity area when excavating to a deeper depth. Therefore, the detailed studies of characteristics of snail fossil are really required in order to preserve this geological heritage while developing the energy resources.

3 Experiments on snail fossil

The site investigation and experiments for this study was carried out at Mae Moh mine during September 13-28, 2011. The disturbed sample of the snail fossil, where located at latitude 18°19′07″ N and longitude 99°41′86″ E, was taken from a subsurface of a location deposited outside the preservation area.

Full body of snail fossils were collected and washed by water. Thirteen sets of oedometer test were conducted on air-dried samples loosely arranged in circular container with diameter 61.8 mm. A whole experimental program with details is given in Table 1

Table 1 Experimental program

№	Loading/unloading steps (kPa)
1	33,98,196,391,815,1630
2	33,98,196,391→196,98,33
3♪	33,98,196,391,815,1630
4♪	33,98,196,391,815,1630,3260→1630,815,391 ,196,98,33
5	33,98,196,391,815,1630,3260→1630,815,391 ,196,98,33
6♪	33
7♪	33,98
8♪	33,98,196
9♪	33,98,196,391
10♪	33,98,196,391,815
11♪	33,98,196,391,815,1630
12♪	33,98,196,391,815,1630,3260
13	33,98,196,391,815,1630,3260→391,33

Note: ♪ = with crushing sound recording

Fig. 2 Specimen of snail fossil in oedometer tests

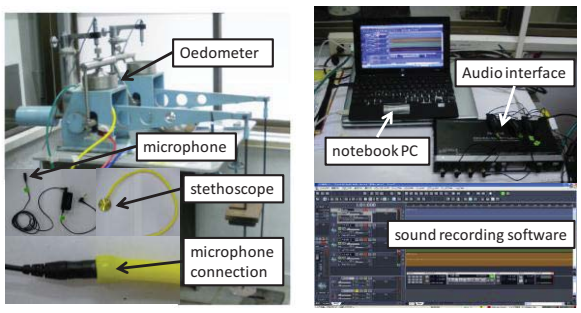

Fig. 3 Sound recording apparatus

As shown Fig.2, oedometer tests were run while crushing sound of fossils was recorded with apparatus shown in Fig.3. Stethoscope used in this study (NURSE SCOPE) with tube ϕ4.4mm×570mm helps transmit the sound to a microphone. Link between tube and microphone is tightly connected to prevent pressure leak. Microphone used in this study (AT9903 Audio-technica) with size ϕ6.4mm×18mm can detect sound frequency between 30Hz-18kHz with sensitivity to sound pressure level -42dB. Four recording channels are linked to audio interface (OCTA-CAPTURE (Roland)), monitored and controlled by sound recording software (Cakewalk Production Plus Pack) thru a notebook computer.

4 Data analysis

Sound wave data in time space were filtered by high-pass filter (HPF) at 3kHz to remove noise as shown Fig. 4. Sound wave pulses with amplitude greater than the defined lowest level were counted over a specific period of time as shown Fig. 5 where crushing sounds were detected as triangular shape Volume change characteristic in terms of void ratio versus applied vertical pressure is shown in Fig.6. Sieve analysis is conducted with result given in Fig.7.

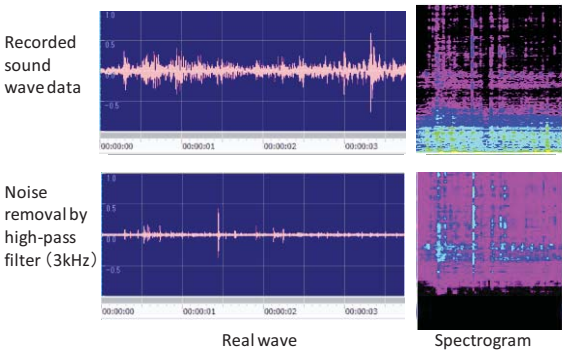

Fig. 4 Sound signal processing (3 second from loading step 3260 kPa in oedoemeter test no.12)

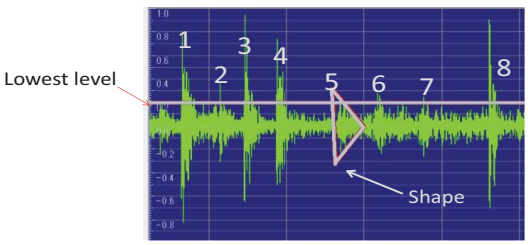

Fig. 5 Wave pulse of crushing sound

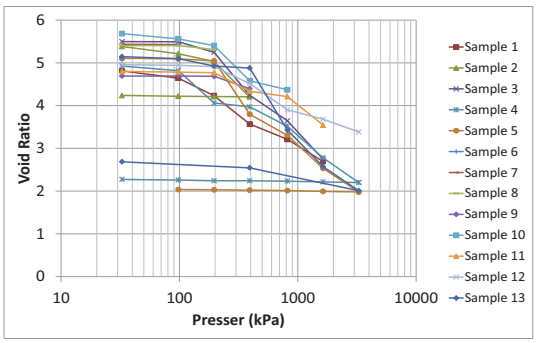

Fig. 6 Consolidation characteristics

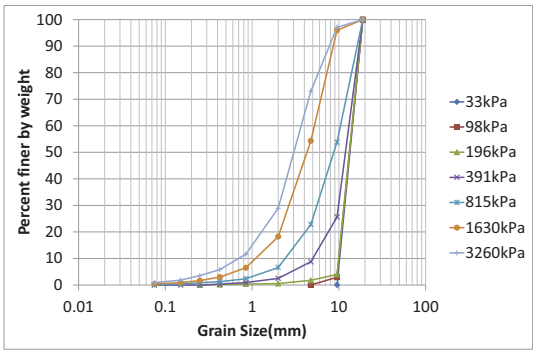

Fig. 7 Grain size distribution

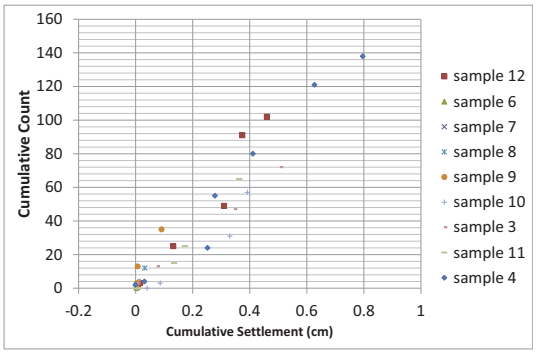

Fig. 8 Cumulative settlement vs cumulative counts of crushing sound

5 Result

As shown in Figs.6-7, a large volume change is observed for pressure between 196-391kPa. Also, this range of crushing pressure is observable by rapid change of cumulative counts of crushing sound. Moreover, the relationship between the cumulative counts and volume change in terms of cumulative settlement can be confirmed as analyzed in Fig.8.

6 Conclusion

This study confirmed that audible frequency measurement of crushing sound of snail fossils can indicate the similar characteristics as observed in oedometer test; therefore, it could be developed to a warning system using microphone installed to a site.

7 References

[1]松岡　元：土質力学，森北出版，1999
[2]地盤工学会「土質試験の方法と解説」，2000
[3]大津　政康：アコースティック・エミッションの特性と理論（第２版），森北出版，2005

Fast Visual Object Categorization by Clustering with Hamming Distance

Students Number: 08_08392 Name: Joowon Kim Supervisor: Yukihiko Yamasita

I Introduction

In recent years, the digital imaging revolution in the World Wide Web facilitates the generation and storage of large collections of images. These images of various scenes include an important information. This exponential growth of the digital image data has created a compelling need for an innovative method for retrieving, recognizing and visualizing images from large collections to use training and education, artificial intelligence, and robotics fields.

Recent advances in computer vision and pattern recognition techniques have given rise to extract such robust and invariant features from images. Usually a large number, perhaps hundreds or thousands, of features are obtained from each image. A vector descriptor, such as the scale invariant feature transform (SIFT) is associated with each features, computed from the intensity pattern [1]. The calculated descriptors are vector quantized by k-means clustering and an image is represented by a bag of these keypoints so that images are searchable in a similar way to bag-of-words in text retrieval.

The idea of bag-of-keypoints has already been applied to generic visual categorization with promising results [2]. In the bag-of-keypoints model, each keypoint is considered independent of all the other keypoints besides the loss of all ordering structure. However, this method does not work well in some cases. In the cases, there exist strongly correlated keypoints in individual images as well as in a collection as a whole. Therefore, it is necessary to exploit the correlation or similarity patterns among the keypoints to improve the retrieval effectiveness. Also, there are a lot of objects in the world and we have more than 100 thousands categories. It requires an intensive learning/training stage for parametric image categorization (e.g. Naive Beyes, SVM classifier). However, it takes too much time to classify using supervised learning methods.

To overcome the limitation, this paper presents a fast visual image categorization method with a new bag-of-keypoints. In this method, Hamming distance is applied to clustering of training data.

II Overview of Proposed Method

The proposed method uses k-means clustering algorithm for building hierarchical training database. The effectiveness of evaluating all images has been considerably low if there are a lot of categories and photos [3]. In general, each category has a similar pattern in bag-of-keypoints so that it is not necessary to evaluate all the training images at the beginning. In this paper, I modify the learning and evaluation stage of bag-of-keypoints algorithm. In the learning stage, we build a three layer hierarchical model of the training images. The first layer consists of the original data. The second layer consists of the representative images extracted from each category by using k-means clustering method and the representative images are clustered again. The third layer consists of the representative images of such clusters. Also we binarize the bag-of-keypoints of the representative images. A bitwise operation is used for comparisons and calculations. Typically, bitwise operations are substantially faster than division, several times faster than multiplication, and sometimes significantly faster than addition. By using Hamming distance, the speed of retrieving should be improved. We evaluate the test images based on clustered training images.

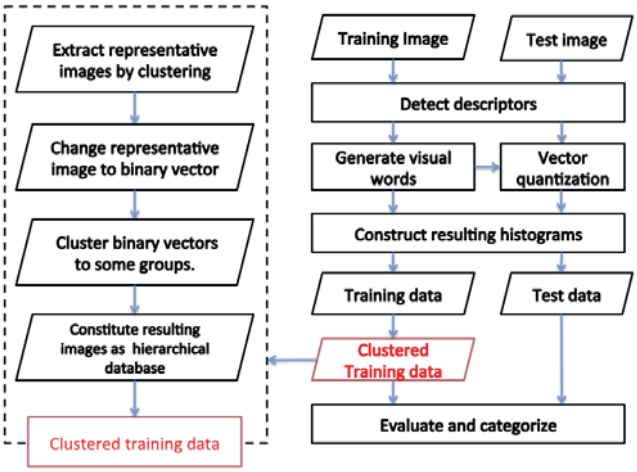

Fig. 1. The proposed method.

The learning algorithm is as follows:

1) Detecting and making descriptors of covariant regions or interest points.
2) Generating visual words by applying vector quantization or clustering based on the descriptors in the training set.
3) Assigning the descriptors to a set of predetermined clusters or visual words in the codebook.
4) Constructing a resulting histogram on individual image, which counts the number discriptors assigned to each cluster and treating the histogram as the feature vector.
5) Clustering the images in each category and extracting some images as the representatives of the each category.

TABLE I
RESULT

		Bag of Keypoints Method						Proposed Bag of Keypoints Method					
Train	cluster	Recog. Rate	Time(ms)	Good Category	Recog. Rate	Bad Categories	Recog. Rate	Recog. Rate	Time(ms)	Good Category	Recog. Rate	Bad Categories	Recog. Rate
15	300	17.11%	2711.48	Soccerball	86.7%	16	0.0%	18.16%	1073.06	DollarBill	86.7%	19	0.0%
	400	17.72%	6133.84	StopSign	80.0%	14	6.7%	19.21%	1085.23	SoccerBall	80.0%	11	6.7%
	500	18.07%	7362.21	windsorchair	73.3%	10	13.3%	22.37%	1888.77	WindsorChair	73.3%	8	13.3%
	1000	18.51%	13527.4	DollarBill	66.6%	8	20.0%	19.30%	3545.69	StopSign	66.7%	10	20.0%
	2000	19.56%	24288.3	Motorbikes	60.0%	6	26.7%	19.65%	4359.68	Motorbikes	60.0%	4	26.7%
30	300	17.46%	5456.88	SoccerBall	93.3%	11	0.0%	24.56%	2292.71	Motorbikes	86.7%	16	0.0%
	400	22.46%	12126.6	Faces	86.7%	19	6.7%	25.26%	2767.04	euphonium	80.0%	9	6.7%
	500	22.72%	14840.9	WindsorChair	80.0%	10	13.3%	26.67%	3332.76	SocceerBall	80.0%	10	13.3%
	1000	23.16%	26844.1	DollarBill	73.3%	8	20.0%	23.95%	5416.3	StopSign	80.0%	4	20.0%
	2000	22.37%	48250.3	Motorbikes	73.3%	3	26.7%	22.63%	9861.84	WindsorChair	73.3%	4	26.7%

6) Transforming the histogram of each representatives resulting image to a binary vector (visual words not 0 is to 1) in the second layer.
7) Building hierarchical database by re-clustering the representative images.

The evaluation algorithm is as follows:

1) Evaluating the similarities between the query and representative images in the third layer. A binary vector is utilized with Hamming distance and the three best clusters are chosen. Next, the similarities between the query and representative images in the three best clusters are evaluated at the second layer and the best 3 clusters are chosen again.
2) Evaluating the similarities between the query and images in the three best clusters. Not a binary vector but a histogram is utilized in an Euclidean distance measure function.

III Experimental Results

The image collection for experiment comprises of 8677 images of 101 manually assigned global categories. It is a larger collection to used for object categorization or image retrieval task in Caltech 101 [4]. To build the visual words based on the k-means clustering, a training set of images is selected before the learning process. The training set used for this purpose consists of 15 and 30 images for each category. To compare the recognition rates between different numbers of visual words, the descriptors are clustered to generate visual words of five different sizes as 300, 400 500, 1000, 2000 units. After the construction process, all the images in the collection are encoded and represented as bag-of-keypoints. For a quantitative evaluation of the categorization results, we selected 15 images for each category in the collection as query images and used the nearest neighbor method for classification. A retrieval is correct if it belongs to the same category as the query image out of the 101 categories as shown in recognition rate. The retrieval time is used as the basic evaluation measure of retrieval performances. The average is calculated over all the queries to generate the table in five different settings.

Table 1 shows the recognition rate on five different codebook sizes. It is clear from Table 1 that the best recognition rates are different depending on the numbers of visual words and clusters. The recognition rates in 30 training images per category are degraded when the sizes are decreased or further increased. Also, Table 1 shows the retrieval speed of the keypoints-based image representation by performing proposed method with Hamming distance and the original method to show the actual improvement in retrieval time of the proposed methods. We obtained more than 5 times faster retrieval speed compare to the original method and also its recognition rates is better than those of the original method. Those results show that it is not necessary to evaluate all images. We can speed up the retrieval process by evaluating between query image and selected images. By analyzing Table 1, we can observe that the performance of the proposed method is much better when there are a lot of training images. The better performances are expected as keypoints are more localized in nature and invariant to viewpoint and illumination changes. We can also observe that the category such as soccer ball or stop sign that do not have irrelevant keypoints performed better than other categories that have many irrelevant keypoints. Overall, the improved result indicates that the retrieval speed by using the proposed method is not negligible and the proposed method can be exploited effectively in large databases.

IV Conclusions

We have investigated fast visual object categorization approach based the bag-of-keypoints that is inspired by the ideas of the text retrieval. In this approach, an interest point is detected and described by the SIFT descriptor at first. Based on the construction of visual words, images are represented as a vector of keypoints. The proposed method evaluates the similarities/correlations between images by the histograms and classifies by the nearest neighbor method using Hamming distance. Experimental results showed that the proposed method improved retrieval speed. However, the precision of the retrieval results is not enough. My method cannot improve the precision compare to Naive Beyes or SVM clasifier.

As future works, we plan to study on a better clustering method for training data to speed up the retrieval time. We need to investigate how to remove irrelevant keypoints in training data.

References

[1] D.Lowe, *Distinctive image features from scale-invariant keypoints.*, IJCV, 60(2), 2004.
[2] G. Csurka, C. Bray, C. Dance, and L. Fan, *Visual categorization with bags of keypoints*, ECCV Workshop on Statistical Learning in Computer Vision, pp. 1-22, 2004.
[3] Oren Boiman, Eli Schechtman, and Michal Irani, *In defense of nearest-neighbor based image classification*, CVPR08, 2008.
[4] L. Fei-Fei, R. Fergus, and P. Perona, *Learning generative visual models from few training examples: an incremental Bayesian approach tested on 101 object categories.*, CVPR 2004, Workshop on Generative-Model Based Vision, 2004.

A Study on Renewable Energy Funds Initiated by NPOs in Japan

Student Number: 08_08676 Name: Keisuke KUSUNOKI Supervisor: Naoya ABE

NPO 主導による再生可能エネルギーファンドに関する研究

楠　恵輔

1. Introduction

In recent years, importance of renewable energy has been increasing. Effects of introduction of renewable energy, such as the creation of employment opportunities, new markets and diversification of energy sources, can be expected. [1] Utilizing these effects, there are some activities trying to contribute to the community using renewable energy by NPOs. These NPOs have built some community wind-mills or installed solar panels with citizens' investment (renewable energy citizens' fund) and subsidy from the government. The method of citizens' fund has advantage of environmental contribution of the citizens, however, it has disadvantage for NPO of much labor cost or risk of fund shortage.

2. Objective

The objective of this study is goal is to investigate the relationship between the characteristics of renewable energy funds and the characteristics of the power plants built by the funds, focusing on the variables such as the amount of the citizens' investment and output capacity and amount (kW, kWh) of each plant.

3. Data & Analysis

This study focused on the renewable energy funds owned by operated by NPOs or local government in Japan, which are for wind power, solar (photovoltaic) power, and small hydro power generation projects. Based on various materials, 19 funds were identified in Japan as of February, 2012. The data and its sources of this study are shown in Table 1.

Table 1 . Data sources

Data category	Data sources
Funds' data: the number of investor; the amount of money to be raised; Amount of investment unit; total amount of investment; investment yield **Power plants' data:** total operating expenses; rated output; electricity generation in a year	Web page of related organizations, relevant literature, inquiry by e-mail or FAX to related organizations
Details of two NPOs	Hearing survey

Two analytical methods were adopted to clarify the goal of this study. Cluster analysis and Principal Component Analysis (PCA) are adequate for dividing the subjects into some groups based on the similarity of their characteristics. Hearing surveys to two NPOs which are involved and maintain renewable energy plants built by the funds supplemented the analysis.

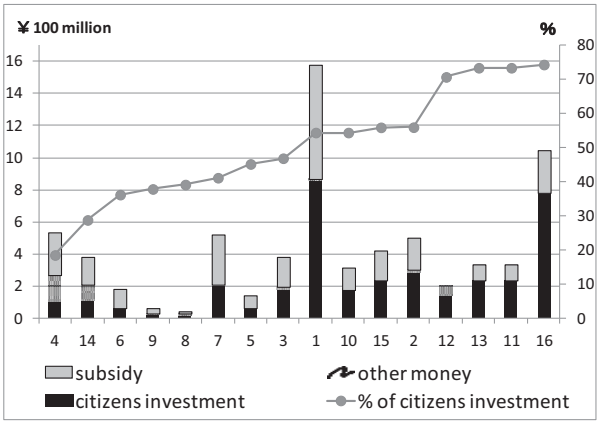

Figure.1 Composition of funds

Fig.1 shows the proportion of the investors of each fund. The majority of these funds are made up of citizens' investment and subsidies from local and/or national government. For example, total amount of Fund #1 is about 16 million Yen, consisting of about 54.4 % from citizens' investment, 45% from subsidy, and 0.6 % from other sources.

4. Results

4.1 Result of analysis

(a) As the result of cluster analysis, it can be divided funds into 6 groups. In Fig.1, horizontal axis and vertical axis means investment yield and the amount money to be raised. Group 1 and Group 2 are special groups because one or another value is an outlier. In Group 3~6, each group are different in investment yield, the amount money to be raised or amount of investment unit. It seems that each fund have been devised for collecting money.

(b) Fig.3 shows the result of PCA. Vectors are eigenvectors of each variable and numbers mean each fund and power plant. The value of cumulative proportion up to second principal component is 75.3, so three-quarter of the entire information has been aggregated into this chart. The meanings of the principal components are inferred from vectors of

each variable. First principal component (horizontal axis) means "power generation potential" and second principal component (vertical axis) means "the depth of the relationship of citizens to the fund" of power plants. These indexes become larger and larger in the negative direction of the axes.

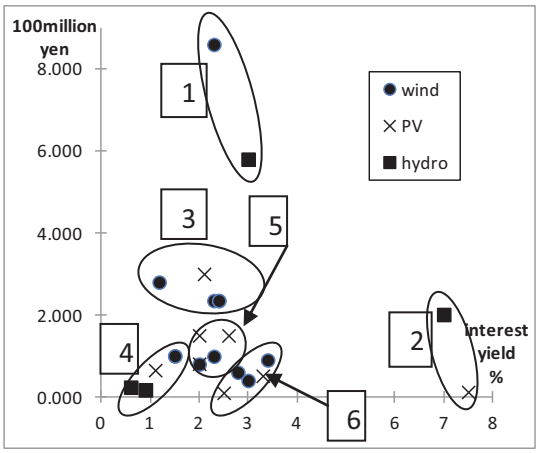

Figure 2. Result of cluster analysis

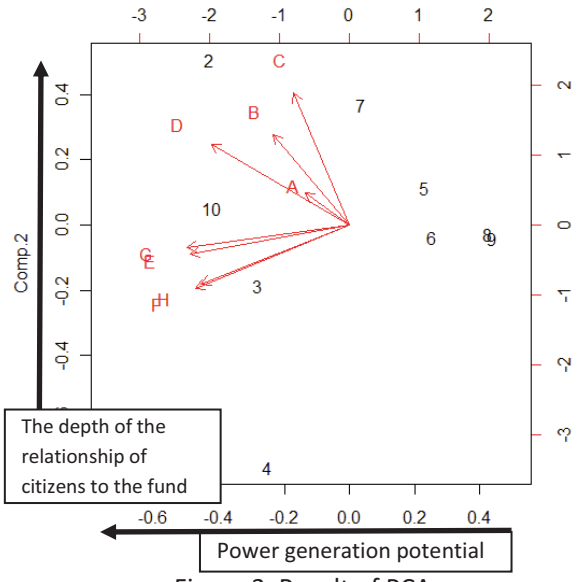

Figure 3. Result of PCA

(c) Finding the remainder between ranking of rated output per citizens' investment and ranking of electricity generation per citizens' investment, it showed "J" in Table.2. These values mean that, if "J">0, power plants at the base of electricity are superior to at the base of rated output. In other words, when judging which power plants generate more electricity, there are differences between judging rated output and actual electricity generation. Operation ratios of samples which ranking have fallen are lower than that of samples of same type.

Table 2. Comparison of the rankings of output capacity basis and actually generated amount basis

#	A	B	C	D	E	F	G	H	I	J
3	w	1500	2543	19	46.9	3.95	3	669	2	1
4	w	1980	3576	21	18.5	3.70	4	668	3	1
6	p	300	379	14	36.2	1.67	6	211	5	1
1	w	7000	13300	22	54.4	4.43	1	842	1	0
7	p	732	864	13	41.2	1.43	7	169	7	0
8	h	20	49	28	39.2	0.46	8	112	8	0
9	h	19	56	34	37.9	0.30	9	90	9	0
5	p	248	293	13	45.2	1.77	5	209	6	-1
2	w	1980	2230	13	56.0	3.96	2	446	4	-2

A: type (w: wind, p: photovoltaic, h: small hydro)
B: rated output [KW] C: electricity generation in 2010 [MWh]
D: operation ratio [%] G: ranking of F
E: citizens' investment per total operating expenses [%]
F: B*D per citizens' investment [KW/￥100,000]
H: C*D per citizens' investment [kWh/￥100,000]
I: ranking of H J: F-H

4.2 Result of hearing survey

Two NPOs' motivation to utilize the scheme of citizens' fund is based on the fact that they cannot get loan finance from financial institutions in common. Then, there is also an advice from the NPO that had built first windmill with a citizens' fund and eventually they had chosen the scheme of citizens' fund. One of the two NPOs is willing continue to utilize this fund scheme for advantage that it can directly involve citizens in activities of diffusion of renewable energy. However, the other NPO indicated reluctance to use the fund scheme again due to the disadvantages; it costs much labor or does not meet the characteristics of a renewable energy project in their views.

5. Conclusion

According to the results of the analysis above and the hearing survey, there are some relationships of trade-off. In fund scheme, relationship between "participation of the citizens" and "labor or cost" is trade-off. The relationship between "the depth of the relationship of citizens to the fund" and "the amount of generation per investment" is also trade-off. As a further study, it is considered that more various funds will appear in the future, so the study should increase samples and analyze them again. The investigation of renewable energy funds owned by NPOs in foreign countries would be also important.

References

[1]Ministry of the Environment, 2010, Basic Energy Plan

A study on the perceptions of drinking water quality and risk in Shenyang, China

Student Number: 08B09368 Name: Lu GAO Supervisor: Naoya ABE

中国瀋陽市における水道水利用者の水質とリスクに対する認識

コウ ロ

1 Introduction

In China, the average water resource capacity per person is only 1/4 of the world and 65% of groundwater and 50% of surface water is polluted respectively.

In the beginning of 1980s, the bottled water entered China market and the consumption of bottled water is increasing every year. At present, the consumption of bottled water in China ranks third in the world and it is increasing at 30% per year. This trend may represent the change of people's perception about the quality of drinking water from the tap.

2 Objective

The objective of this study is to understand the perception of tap water quality and risk in Shenyang, China. A previous study (Doria, 2005) conducted a study about the tap water risk and quality perception in Portugal .He found the factors such as flavour which can impact the perception.

3 Data and Analysis

An interview survey was performed in Shenyang, China, from January 11st to February 1, 2012. Shenyang is one of the 10 largest cities (like Beijing and Shanghai) in China and the water resource capacity per person is the lowest in those cities. In the past, as the biggest heavy industrial city in Northeast China, there are severe environmental problems such as water contamination of rivers in Shenyang. At present, although the water quality becomes better than before, some citizen of Shenyang still worry about it.

In this study, 349 questionnaires sheets were collected and the effective responses are 270 (effective answer rate: 77.4 %.) The sample is composed of 41.5% (112) male and 58.5% (158) female and the mean age is 44.5 years old (youngest: 18, eldest to 73 years.)

One of the questions was about the respondents' opinions about the quality of tap water, which is about the taste, colour, odour of tap water. The survey found that 30% of the respondents replied they don't satisfy with tap water quality, 53% replied that they do not know, and 13% replied that they satisfied with tap water. As for the question of whether respondents think there are health risks associated with drinking tap water at home, 41% of the respondents indicated that there are indeed the risks, 40% respondents replied they didn't know, and just 18% respondents disagree with the statement (see fig1.) Those two results imply that more people concern about the risk of tap water than the quality of tap water in the city.

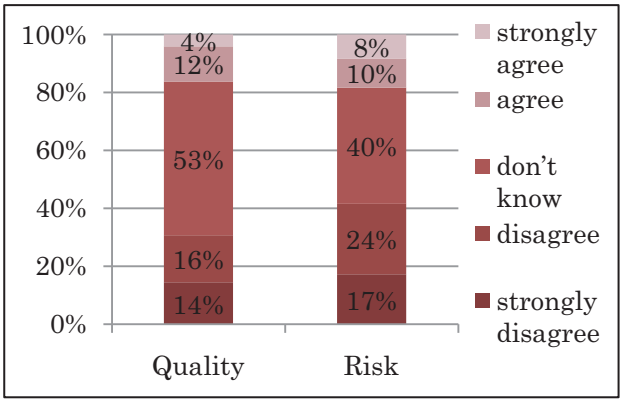

Fig 1 Perception of tap water quality and risk

As for the analytical method, the Structural Equation Modeling (a.k.a. Covariance Structure Analysis) was adopted. This approach is used to analysis structural relation between variables, some of which may be latent. A simple example is shown in Fig2, which is about perceptional structure of people ability of reading and writing based on the levels of intellectual skills and sense of humor. In this figure, in part 1, "Intelligence" is a latent variable that is not directly measured but rather assessed indirectly using "Reading" and "Writing", two measured variable and this part use the factor analysis which can show some measured variable by common factor.

An equation for part 1 was defined as follow.

$$\text{Reading} = a \times \text{Intelligence} + e2$$
$$\text{Writing} = b \times \text{Intelligence} + e1$$

"a" and "b" are factor loadings, which show the relationship between Intelligence and Reading (Writing). e1 and e2 are error terms.

In part 2, "sense of humor" is a result of "Intelligence". An equation for part 2 was defined as follow.

Sense of humor=c×Intelligence+e3

"c" is the path coefficients which show the causal relationship between "Intelligence" and "sense of humor". If the c is big, it means "sense of humor" is large impact by "Intelligence". And the one arrows stand for regression weights and the two arrows stand for correlations among predictors.

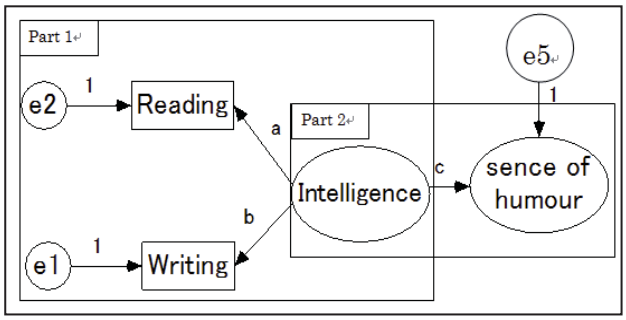

Fig 2 example model

4 Results

The structural equation model that integrates the main variable of this study is presented on Figure 3. Results show that, in Lisbon, Portugal, perceived tap water quality is largely influenced by "flavour", but in Shenyang, China, "risk" has a very important role for perception of tap water quality. On the other hand, in Lisbon, Portugal, perceived tap water risk is largely influenced by "colour", but in Shenyang, China, "flavour" has a very important role for perception of tap water risk.

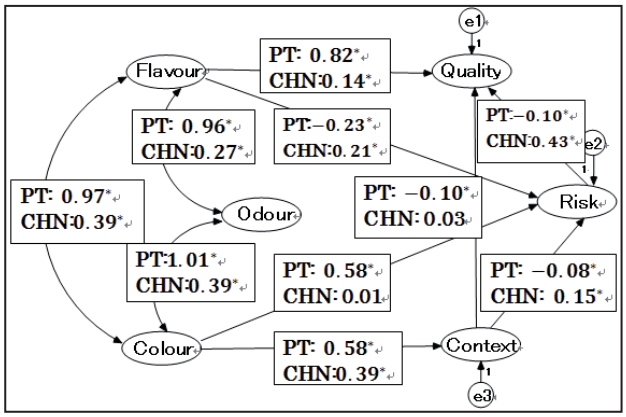

Fig.3 A structural equation model (Portugal and China)

This model is referred from the previous study (Doria, 2005), which investigated the perceptional model about drinking water in Portugal and its fitness indexes are: non-normed fit index (NNFI) =0.964, the comparative fit (CFI) =0.963, the root mean square error of approximation (RMSEA) =0.046. The result of applying the same model framework to the Shenyang' data provided the fit indexes such as NNFI=-0.045, CFI=0.751, RMSEA=0.236 respectively. It means the Chinese data is not explained well by this model.

For this reason, a Modified model was constructed (Fig4). Two variables which are "impurity" and "pump" were added in this model. Results show that, both perceived tap water quality and risk are largely influenced by flavour. Those fit indexes are NNFI=0.868, CFI=0.952, RMSEA=0.094. This model becomes better than before.

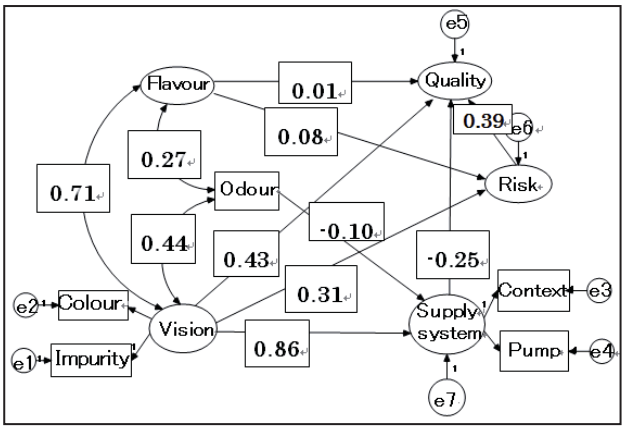

Fig4 Modification model

5 Conclusion

In Portugal, according to Doris (2005), people take variable "flavour" as the medium to perceive the tap water quality. But in China, people consider a variable "risk", which is more general notion, as the medium to perceive the tap water quality. It may mean Chinese people pay more attention to the safety of tap water.

In the modification model which is fit Chinese data, "Vision" is used as the medium to perceive the tap water quality and risk. It may mean Chinese people used the factor which can be visible to perceive the quality and risk of tap water. If the vision was being improved, maybe the perception of tap water quality and risk will become better.

References

Doria, Pidgeon,Hunter, 2005, Perception of tap water risks and quality: a structural equation model approach, Water Science &Technology, Vol 52, No8, PP143-149

Development of time domain channel sounding system of BAN and evaluation of SIMO diversity

Student Number: 08B10012 Name: Sho Kobayashi Supervisor: Jun-ichi Takada, Minseok Kim

1 Introduction

Wireless body area network(BAN) has seen very rapid development in recent years. BAN involves communication between communicating nodes located in, on, or around the human body.In the future Wireless BAN systems are expected to find wide application in medical care, sports,entertainment, or many other fields[4]. BAN Channels are those surrounding the human body, so the affect of human body and human body motion must be considered while studying BAN channels.

In the IEEE 802.15.6 standard different frequency bands are allocated for WBAN applications.Ultra-wideband (UWB)technology is also considered in this standard for usage in WBAN. It constitute communication over very wide bandwidth, enabling high data rate transmissions at very low power. In UWB transmission the signals are usually of very short duration, like a pulse, and we can easily differentiate the signal from its delayed versions. Hence UWB communication has the advantage of being very resilient to multi path fading.

While considering human body motion each body parts moves differently and because of this,to understand the WBAN channel we need to make dynamic multi port channel measurements as opposed to static measurements. To study the UWB WBAN channel,a UWB measurement system was developed and verified to be working properly. Then we conducted an experiment to make on-body WBAN SIMO channel measurement using one transmitting and two receiving antennas. We assumed that the antenna diversity can be evaluated by measuring the correlation between each channel.

2 Configuration of the measurement system

UWB signal measurements, are always done either in time domain or frequency domain[1]. In the case of dynamic channel such as BAN, the signal is always changing and therefore the time domain method of measurement which uses digital sampling oscilloscope with high sampling rate is better because of short measurement time compared to the frequency domain method. The configuration of the measurement system is shown in Figure 1. The transmitter is constructed with a pulse generator (PG) and a band pass filter (BPF). For UWB, the 3.4-4.8GHz and 7.25-10.25GHz bands are allowed to be used in Japan. The receiver is composed of a BPF, a Low noise amplifier(LNA), and an oscilloscope. Due to very low transmitted signal power, we had to amplify the pulse at the receiver to be able to view the signal. The PG and the Oscilloscope were synchronized using trigger signal from signal generator so as to be able to observe the delay time of pulse.

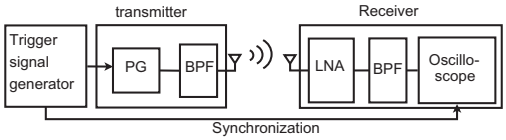

Figure 1: Time domain method

3 Data process

The received signals were observed using the digital sampling oscilloscope. The oscilloscope was controlled using PC. Because of the very low transmitted power, SNR (signal to noise rate)at the receiver is also very low. To be able to find the pulse correctly, SNR has to be improve by averaging[2]. If averaging is done Ntimes, SNR is improved by $10\log_{10} N$dB.

Receiving signal includes the channel transfer function and the system response of the measurement system. We have to therefore remove the system response from the received signal to get the channel transfer function. In this system, the power of PG couldn't not be changed, so we removed it after measurement. Received signal can be mathematically represented as

$$Y(f) = X(f)G_t(f)H(f)G_r(f) \tag{1}$$

$X(f), Y(f)$ are spectra of the transmitted and received signals, and $G_t(f)$, $G_r(f)$ system response of transmitter and receiver. $H(f)$ is transfer function of channel including antennas. On the other hand, when transmitter and receiver are connected through the attenuator$H_{\mathrm{att}}(t)$ as the calibration measurement, the received signal is

$$Y'(f) = X(f)G_t(f)H_{\mathrm{att}}(f)G_r(f) \tag{2}$$

we can then get channel transfer function by following.

$$H(f) = \frac{Y(f)}{X(f)G_t(f)G_r(f)} = \frac{Y(f)H_{\mathrm{att}}(f)}{Y'(f)} \tag{3}$$

Channel impulse response$h(t)$ can be gotten from channel transfer function by inverse Fourier transform.

$$h(t) = \frac{1}{2\pi}\int_{-\infty}^{\infty} H(f)\mathrm{e}^{j2\pi ft}dt \tag{4}$$

4 Verification

4.1 Direct connection

The receiver has 4 port in this system. To confirm the same signal can be received at each port, we compare the signal by connecting the transmitter and receiver directly through

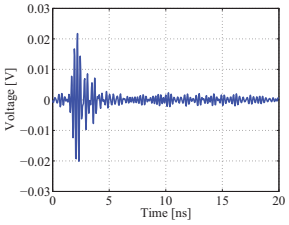

Figure 2: receiver 1

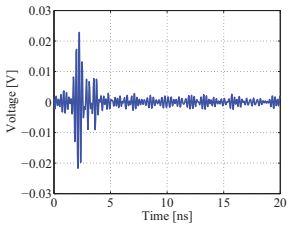

Figure 3: receiver 2

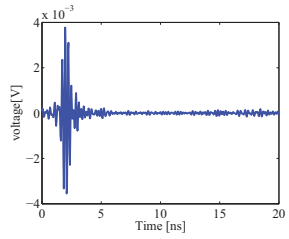

Figure 4: Oscilloscope

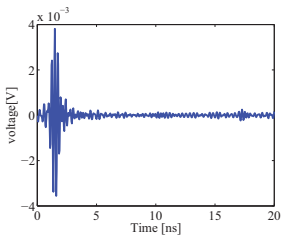

Figure 5: VNA

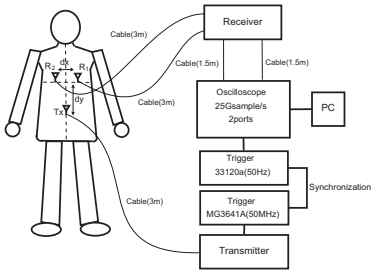

Figure 6: Caption for figures at the bottom

Table 1: parameter

Triggering Signal Frequency	500Hz
sampling frequency	25GHz
Measurement time	about 8.6sec
d_x, d_y	(1,5,10,15,20cm),(10,18cm)

an attenuator. Figure 2 and 3 are the two calibrated signal which were generated by T-branch at the same time at two port. We confirmed that the signals can be received at the same time and their power are the same.

4.2 Free space

Next, I measured the signal in free space and compare the data from VNA which can measure channel transfer function. Figure4 and 5 show each channel impulse response for a distance of 30cm. Almost same voltage level can be observed.

5 SIMO channel measurement

In the experiment, we attached the transmitting antenna on the navel(fixed), and two receiving antennas on the center of chest. We then measured the signal while standing still, walking,and standing up and sitting down. Next, we changed the distance d_x and d_y, and repeated the measurements for the above motion scenarios.

Table 1 is the parameter of this experiment.

From the maxpeak of obtained data, we found out the path gain about each path by subtracting the power. Figure 5 is the case for d_x=1cm andd_y=10cm.

The similar fluctuation can be observed in channel 2. I obtained correlation coefficient of Path gain between channel 1 and channel 2 in each case. The correlation is defined

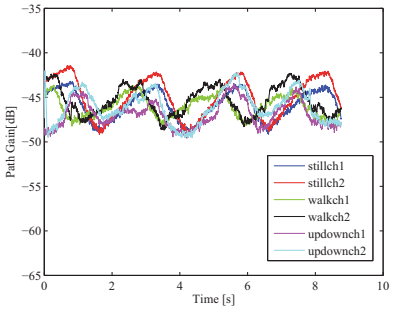

Figure 7: Path gain(d_x=15cm,d_y=10cm)

Table 2: Correlation coefficient(d_y=10cm)

	still	walk	updown
d_x=1cm	0.9482	0.9080	0.8536
d_x=5cm	0.9825	0.9158	0.9313
d_x=10cm	0.9784	0.8856	0.9366
d_x=15cm	0.9846	0.8968	0.8575
d_x=20cm	0.9613	0.7388	0.1724

Table 3: Correlation coefficient(d_y=18cm)

	still	walk	updown
d_x=1cm	0.9058	0.7712	0.8966
d_x=5cm	0.8407	0.5548	0.0858
d_x=10cm	0.6982	0.7056	0.8979
d_x=15cm	0.6033	0.6129	0.5818
d_x=20cm	0.8051	0.6556	0.5354

by

$$R(x,y) = \frac{\sum_{i=1}^{n}(x_i - \overline{x})(y_i - \overline{y})}{\sqrt{\sum_{i=1}^{n}(x_i - \overline{x})^2}\sqrt{\sum_{i=1}^{n}(y_i - \overline{y})^2}} \quad (5)$$

where x_i and y_i represent measurement data, and $\overline{x}$ and $\overline{y}$ denote average of it[4]. Table 2 and 3 shows the results. Though for higher antenna diversity low correlation between the channels are preferred, from the results we observe high correlation even when the distance between the antennas are long.We therefore need to consider other methods such as polarization diversity in front of body.

6 Conclusion

In this research, a UWB time domain channel sounding system for BAN was developed and its accuracy evaluated. Also, We measured the on-body channels and calculated their correlation.

References

[1] Pascal Pagani, Friedman TchoffoTalom, Patrice Pajusco, and Bernard Uguen, Ultra-Wideband Radio Propagation Channels, John Wiley and Sons, Inc, Jan 2010

[2] Huynh Thi Thanh Trieu, Junichi Takada, Katsuyuki Haneda, Kenichi Takizawa " Validating the effectiveness of UWB transmission simulation using a stored channel, "papers of Technical Meeting on Instrumentation and Measurement, IEE Japan, IM-06-16-23 Jul 2006,

[3] Julien Keignart, Chadi Abou-Rjeily, Christophe Delaveaud, and Norbert Daniele " UWB SIMO Channel Measurements and Simulations, " *Microwave Theory and Techniques, IEEE Transactions*, 54 Issue:4, pp.1812-1819, June 2006

[4] Norihiko Katayama, et.al " Channel Model on Various Frequency Bands for Wearable Body Area Network, "IEICE Trans. Comm Vol.E92-B No.2 pp.418-424, Feb. 2009

TiO_2 光触媒による水中のテトラクロロエチレン(PCE)の光分解

学籍番号：08B10443　氏名：左　皓
指導教員：日野出　洋文　サリム　クリス

1. 緒言

地下水汚染物質の中で、有機塩素化合物は代表的な例である。有機塩素化合物は、トリクロロエチレン(TCE)、テトラクロロエチレン(PCE)など、塩素を含む有機化合物の総称で、ほとんどが人工的に合成した化合物で、主に農薬や溶剤として利用されている。環境中で非常に安定であり、生物の脂肪内の蓄積性が高く、一般に毒性が強く、発ガン性の疑いもある有害なものである。生物的に分解されにくいため、一度汚染される環境が元の状態に回復するには長時間が必要である。その上、低濃度のものが大量に地下水中に広がっているため、回収及び除去が非常に困難で莫大なコストと労力が必要となっている。

地下水汚染解決策として、活性炭などの吸着材を用いて、汚染物質を除去する吸着法や土着微生物に酸素や栄養源を与え、その微生物により地下水を浄化させる微生物浄化及び酸化剤と水の反応によりヒドロキシルラジカルを多く発生させ、酸化分解反応の促進を目的とした促進酸化法などの方法がある。活性炭による吸着法は短い処理時間がかかるが、使用された活性炭の二次処理が考えなければならない。微生物浄化法は最初費用が低いが、長い処理時間がかかる。促進酸化法は短い処理時間がかかるし、汚染物の二次処理がいらない。本研究では、促進酸化法の一種として、UV TiO_2 システムが使われている。

最近、光だけで汚染物質を分解できる酸化チタン光触媒が注目されている。光触媒としての酸化チタンは以下の特徴を持っている。

①強い酸化力と超親水性を持つ。
②紫外線照射で有機汚染物が分解できる。
③資源的に豊富である。
④安定した物質で、水に入れても分解しない。
⑤二次汚染の心配がない。

以上を踏まえ、本研究ではエネルギーフリー、環境負荷が低く、簡易な処理法を実現しうる酸化チタン光触媒をゾルゲル法で調製し、有機塩素化合物を除去することを目的としている。

2. 実験

2.1 光触媒の合成

光触媒は、ゾルゲル法で合成した。合成の手順は以下のように示す。

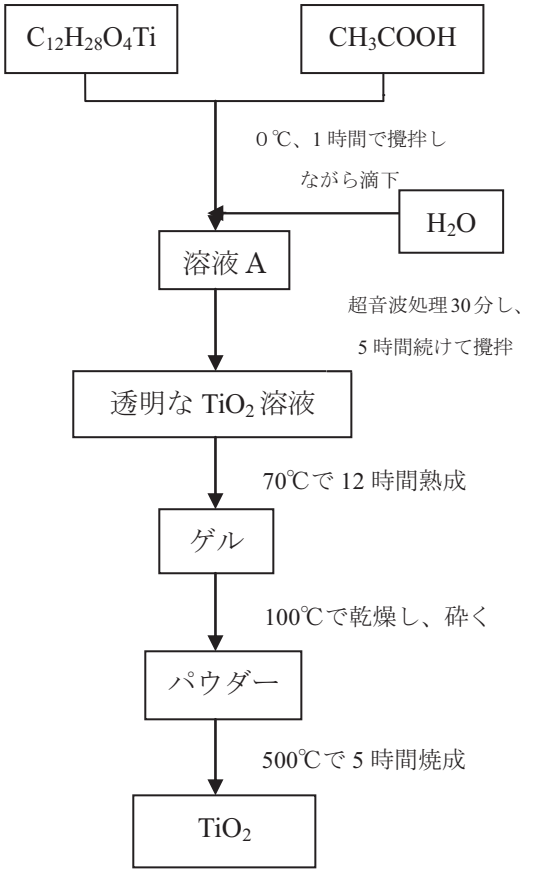

2.2 光触媒のキャラクタリゼーション

合成した光触媒について、TG-DTA、XRD、SEM-EDS、TEM 及び BET 比表面積測定によるキャラクタリゼーションを行った。

表 1 に合成した各光触媒の比表面積及び粒子径を示す。

表 1 各光触媒の比表面積及び粒子径

前駆体:溶媒:水 (モル比)	比表面積 (m^2/g)	一次粒子径 (nm)
1:10:250	94	16.7
1:10:300	102	14.5
1:10:350	110	13.4
1:10:400	98	14.1
Degussa P-25	47	19.6

比較のために、市販の酸化チタンのキャラクタリゼーションも行った。表 1 に示したように、前駆体：溶媒：水のモル率を調整しながら、調製した酸化チタンは異なるサイズの粒子径ができ、市販の酸化チタンより小さい。比表面積が 2 倍以上大きい。したがって、調製した酸化チタンは市販の酸化チタン光触媒より高い光触媒活性を示すことを予測している。

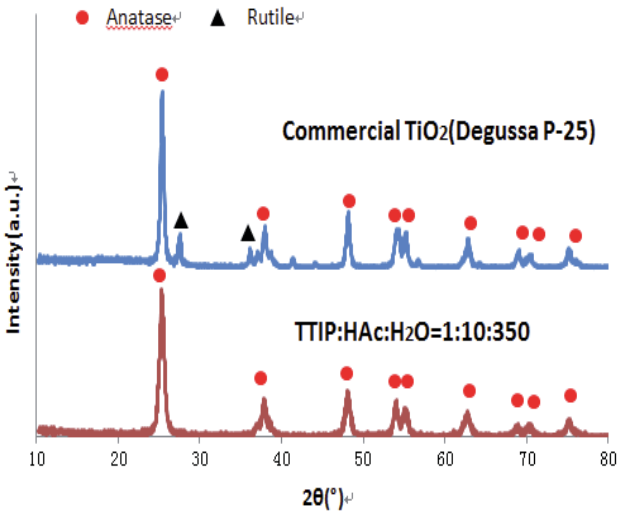

図 1　XRD のパターン

図 1 から見ると、調製した酸化チタンのアナターゼ型のみが確認でき、市販の酸化チタン光触媒はアナターゼ型以外にルチル型も観測された。アナターゼ型の方はバンドギャップが大きく、光触媒としての活性が高いので、アナターゼ型のみ観測された酸化チタンの光触媒活性はもっと高い。

2.3　PCE の光分解実験

UV 源として、100W、波長は 300~600nm の高圧水銀ランプを用いて PCE の光分解実験を行った。PCE の揮発を抑制するために実験では閉鎖系を保ち、UV 照射による光分解実験の前に PCE 溶液と酸化チタン光触媒を吸着平衡に至らせてから、一度可視・紫外線分光法で初吸光度を測定し、それから光照射を行う。PCE の初濃度は 150 ppm で、PCE 水溶液の量は 700 ml、触媒投入量は 0.14 g である。PCE は 201 nm の波長で吸光度が一番高いので、この波長における吸光度を測定した。水のモル率を調整しながら、調製した酸化チタン及び市販酸化チタン光触媒による PCE の分解率は図 2 に示す。

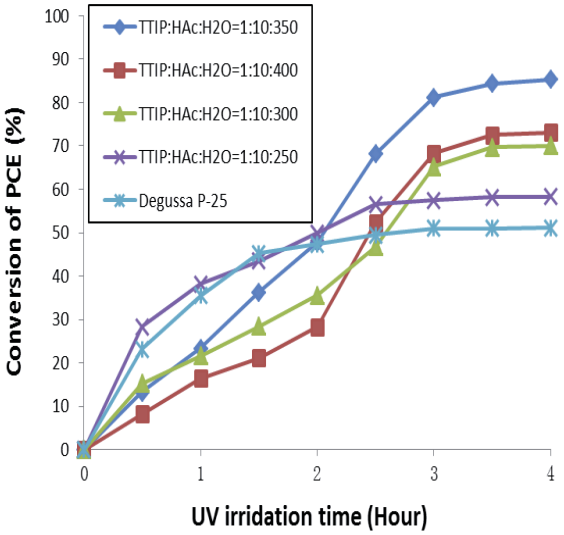

図 2　PCE の分解

図 2 に示したように、前駆体：溶媒：水(モル比)＝1:10:350 における合成した酸化チタンは一番高い光触媒活性を示した。この時、PCE の分解率は 85%である。市販の酸化チタン光触媒は一番低い分解率 51%を得た。

3.　結論

ゾルゲル法でナノサイズの酸化チタン光触媒の合成ができ、一次粒子径は 13.4~16.7nm である。PCE の光分解の実験において、前駆体：溶媒：水のモル率を調整しながら、合成した酸化チタン光触媒は異なる光触媒の活性を示した。前駆体：溶媒：水＝1:10:350 の時、合成した酸化チタンの粒子径が一番小さく、比表面積が一番大きく、PCE に対する分解率が一番高く、より高い光触媒活性を示した。

参考

[1] N. Venkatachalam, Materials Chemistry and Physics 104(2007)454-459
[2] Go Ishida, the dissertation for master degree of engineering, Tokyo Institute of Technology, 2010
[3] Zhiwei Wu, the dissertation for master degree of engineering, Tokyo Institute of Technology, 2008

タケからのバイオエタノール生成における微細化とアルカリ処理の効果

学籍番号：08-12287　氏名：徐 芸萌　指導教員：中崎 清彦

1 目的

近年、石油代替燃料として、食糧と競合することのないセルロース性資源からバイオエタノールを効率よく生産する方法の開発が期待を集めている[1]。一方、タケは成長が速く、林地や畑への侵食が問題となっていることから、竹林の整備と伐採したタケの有効利用のための技術開発が求められている。本研究では、タケに微細化処理とアルカリ処理を施すことによりセルロースの分解性を向上させ、同時糖化発酵 (SSF) によるタケからのバイオエタノール生成を試みた。

2 実験方法

2.1 使用したタケ、酵素および酵母

タケは静岡県浜松市で採取した孟宗竹を竹粉砕機 (チッパリーナ、丸大鉄工株式会社)により粉砕し、チップにしたものを使用した。また、タケの糖化において、タケに含まれるセルロースとメイセラーゼの反応性を向上させるため、タケチップを微細化処理した。常温生竹微粉製造機(PA-Z、丸大鉄工株式会社)によりタケチップを粒径 300～500 μm、および、50 μm 以下の粉末になるよう、それぞれ微細化して使用した。酵素としては、明治製菓に提供を受けた *Trichoderma viride* 由来のメイセラーゼ(Meicelase CEPB-5394、明治製菓株式会社)を使用した。酵母にはパン酵母である Baker's yeast (*Saccharomyces cerevisiae*)を用いた。酵母は 30℃で 3 日間、YM 寒天培地(glucose,10g ; Polypepton,5g ; Yeast extract,3g ; Malt extract,3g ; agar,20g ; distilled water,1L ; pH 6.2)上で培養後 4℃の冷蔵庫で保存した。

2.2 タケの酸・アルカリ処理

タケに含まれるリグニンを除去し、セルロースの分解能を向上させる目的でタケ粉末を酸・アルカリ溶液で処理した。酸・アルカリ処理は 4%H_2SO_4、1%NaOH、1%$Ca(OH)_2$水溶液に 50 μm タケ粉末を 100 g/L となるように添加し、オートクレーブで 135℃、90 分間加熱することによりおこなった。引き続き、濾過により固液分離し、固体試料を蒸留水で洗浄した後乾燥させた。ただし、1%$Ca(OH)_2$処理では、濾過による固液分離の前に乳酸による中和をおこない、$Ca(OH)_2$を可溶化させて取り除いた。

2.3 タケの液体糖化

2.1 および 2.2 で微細化処理、および、酸・アルカリ処理したタケの糖化をおこなった。0.1 M クエン酸緩衝液にセルラーゼを 1.0 g/L、調製したタケを 20 g/L となるように添加し、温度条件 35℃で糖化を開始した。また、糖化で生成したグルコースの濃度を HPLC により測定した。

2.4 フロログルシノール染色によるタケ中リグニンの可視化

タケに含まれるリグニンをフロログルシノール染色により可視化し、NaOH 処理によってタケに含まれるリグニンが除去されているかを確認した。メタノール 5 mL と蒸留水 5 mL の混合溶液にフロログルシノール 38 mg を加えて溶解し、塩酸 5 mL を加えて染色溶液とした。未処理の 50 μm タケ粉末、および、アルカリ処理した 50 μm タケ粉末 1 mg に染色溶液をそれぞれ 40 μL 滴下した。約 1 分間静置した後、タケ粉末を顕微鏡で観察した。

2.5 NaOH 処理タケ粉末の固体培養 SSF

1%NaOH 処理した 50 μm タケ粉末の固体培養 SSF をおこない、高濃度のエタノール生成を試みた。Yeast extract、Polypepton、メイセラーゼを溶解した 0.1 M クエン酸緩衝液に 1%NaOH 処理タケ微細粉末を添加し、Baker's yeast を接種して温度条件 35℃で培養を開始した。なお、Yeast extract は 3 g/L、Polypepton は 5 g/L、1%NaOH 処理タケ微細粉末は 300 g/L となるように添加した。また、メイセラーゼの濃度は 5、10、15 g/L でおこなった。96 時間培養し、グルコース濃度とエタノール濃度を HPLC により測定した。

3 結果と考察

3.1 タケの糖化における微細化の効果

タケチップ、300～500 μm タケ粉末、および、50 μm タケ粉末の糖化における 96 時間後のグルコース濃度を Fig. 1 に示す。グルコース濃度は、50 μm タケ粉末で最大の 2.09 g/L となり、タケの粒径が小さいほど生成するグルコース濃度が高くなることが確かめられた。以上の結果、タケを微細化することによってセルロースと酵素の反応性を高めることができた。

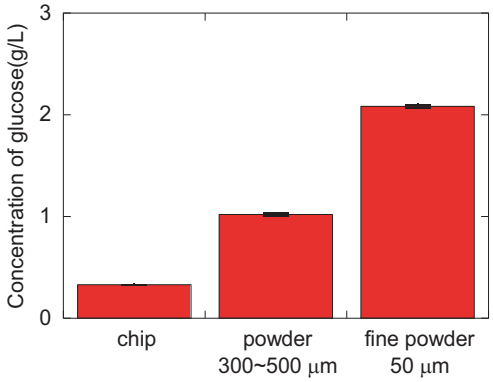

Fig. 1　タケチップ、300～500 μm タケ粉末、および、50 μm タケ粉末の液体糖化における 96 時間後のグルコース濃度 (n=3)

3.2 タケ粉末の糖化における酸・アルカリ処理の効果

酸・アルカリ処理した 50μm タケ粉末の糖化におけるグルコース濃度の経時変化を前処理なしの結果と比較して Fig. 2 に示す。4%H_2SO_4、1%NaOH、1%$Ca(OH)_2$のいずれの前処理においても、グルコースが前処理なしに比べて高濃度に生成したことから、

酸・アルカリの前処理はセルロースの糖化を促進する効果があることが確かめられた。中でも 1%NaOH 処理は特に効果が高く、タケ微細粉末中セルロースの分解率は 77.6%となり、前処理なしの 13.0%から大幅に増加した。

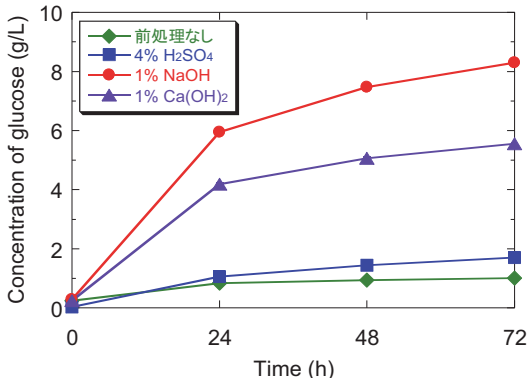

Fig. 2　酸・アルカリ処理したタケ微細粉末の液体糖化におけるグルコース濃度の経時変化 (n = 3)

3.3 タケの液体糖化における NaOH 濃度の影響

1%NaOH および 5%NaOH 処理を施したタケチップ、300～500 μm タケ粉末、および、50 μm タケ粉末の液体糖化における 96 時間後のグルコース濃度を Fig. 3 に示す。いずれも NaOH 濃度を高くすることでグルコース濃度は高くなったが、タケチップと 300～500 μm タケ粉末でグルコース濃度が 2 倍になったのに対し、50 μm タケ粉末では 1.1 倍と上昇幅が小さく、1%NaOH 処理でも高いグルコース濃度を得られることがわかった。

Fig. 4 にフロログルシノール染色によりリグニンを可視化した 50 μm タケ粉末の顕微鏡写真を示す。未処理の 50 μm タケ粉末では赤色に染色された部分が多く、リグニンが多く含まれていることが確かめられた。一方、1%NaOH、および、5%NaOH 処理した 50 μm タケ粉末は染色されず、リグニンが除去されていることが確かめられた。これより、50 μm タケ粉末においては、NaOH 処理における NaOH の濃度が 1%あれば、十分にリグニンを除去する効果があることがわかった。以上の結果、タケを 50 μm に微細化することによって、NaOH 処理の効率を高め、低い NaOH 濃度でリグニンが除去可能であることが確かめられた。

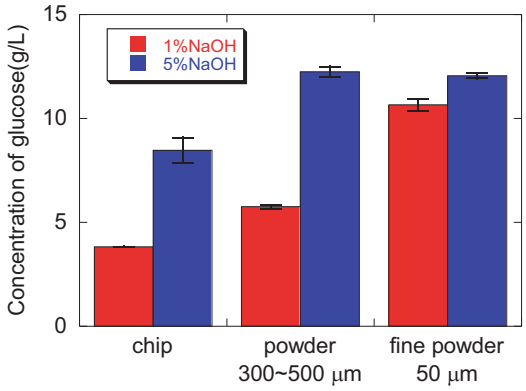

Fig. 3　1%NaOH、5%NaOH 処理したタケの液体糖化における 96 時間後のグルコース濃度 (n=3)

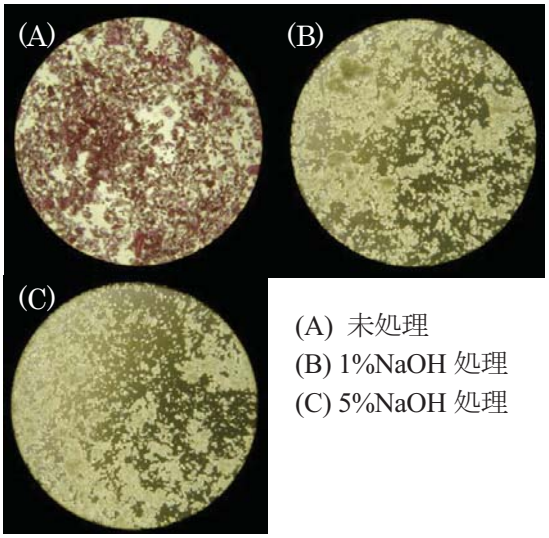

Fig. 4　フロログルシノール染色による 50 μm タケ粉末中リグニンの可視化 (倍率 200 倍)

3.5 NaOH 処理タケ粉末の固体培養 SSF

1%NaOH 処理タケ粉末を用いた固体培養 SSF における培養 96 時間後のグルコース濃度とエタノール濃度を Fig. 5 に示す。生成したエタノールの濃度は酵素濃度 5、10、15 g/L でそれぞれ 30.7、40.1、45.4 g/L となった。以上の結果、1%NaOH 処理した 50 μm タケ粉末の固体培養 SSF において、酵素濃度を増加させることでエタノールは 45 g/L 以上の高濃度化が可能であることが確かめられた。

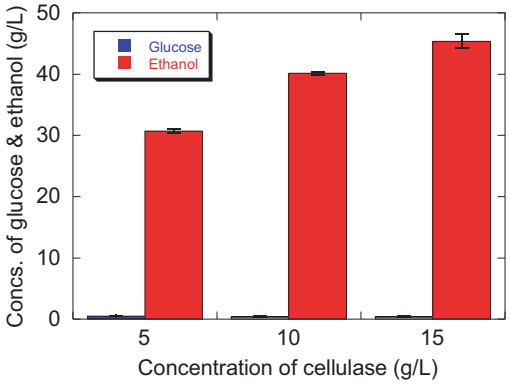

Fig. 5　1%NaOH 処理タケ微細粉末の固体培養 SSF における培養 96 時間後のグルコース濃度およびエタノール濃度 (n=3)

4 結論

本研究では、タケを50 μmに微細化することによって、NaOH処理の効率を高め、低いNaOH濃度でリグニンが除去可能であることを確かめた。また、1%NaOH処理した50 μmタケ粉末を固体培養SSFすることにより、約45 g/Lの高濃度エタノールが生成可能であることを明らかにした。

References

[1] 森川 康、第9回 酵素応用シンポジウム、セルロース系バイオマスの酵素糖化の現状と将来、http://www.amano-enzyme.co.jp/jp/company/pdf/9/theme-7.pdf

Investigation of carbonation depth of real structures in The Philippines and Laos

Student number: 08_13743 Name: Satoshi Takaki Supervisor: Nobuaki Otsuki

1. Introduction

Nowadays, carbonation of concrete is serious problem. After losing alkalinity of concrete, passive states of the surface on the steel bar could be broken, and become to be corrosion. To prevent deterioration, maintenance is very important against carbonation of concrete. And it is necessary to predict deterioration by carbonation for maintenance.

However, carbonation of existing structures has not been investigated yet, especially in Southeast Asia wherein it is a high temperature and heavy rain.

Therefore, this study aims, (1) To evaluate the carbonation depth in the Philippines and Laos existing structure. (2) To evaluate effect of temperature and environments in carbonation speed coefficient.

2. Carbonation speed

Carbonation is a chemical reaction as equation (2.1) between calcium hydrate in concrete and CO_2 in atmosphere.

$$Ca(OH)_2+CO_2 \rightarrow CaCO_3+H_2O \cdots\cdots\cdots\cdots (2.1)$$

From the previous research[1], carbonation depth was calculated the following formula (2.2).

$$X = A\sqrt{t} \cdots\cdots\cdots\cdots\cdots\cdots\cdots\cdots (2.2)$$

"X" represents carbonation depth, "t" material age and "A" is called carbonation coefficient which is affected by environments and concretes. Coefficient "A" also depend on diffusion speed of carbon dioxide in concrete. Therefore carbon dioxide is difficult to penetrate when concrete is wet, because of full of water in fine pores. From previous research [3] carbonation of concrete without roof is more slowly about twice than with roof.

Additionally, there are many painted concrete as investigation objects in this study, from that reason, we apply formula (2.3)[4] to carbonation depth of painted concrete.

$$X = A(\sqrt{t+R^2}-R) \cdots\cdots\cdots\cdots\cdots (2.3)$$

$$\left(A = \sqrt{2D_cC/H} \quad , \quad R = D_c/A(D_f/d) \right)$$

This formula is based on Fick's 1st Law. "X" and "A" is same as formula (2.2) . "R" is value of resistance of paint against carbonation. "D_c" and "D_f" is carbon dioxide diffusion in concrete and paint. "C" is CO_2 concentration of surface on concrete. "H" amount of calcium hydrate by a unit volume. And "d" is paint thickness.

Formula (2.5) is what formula (2.3) is transformed into.

$$A = X/\sqrt{t - X(H/C)(d/D_f)} \cdots\cdots\cdots\cdots (2.5)$$

From this formula, coefficient "A" is determined by substituting value of "D_f", "C", "H", "d".

3. Sight Investigation and results

3.2 Investigation method

Carbonation depth was measured according to NDIS 3419, "Method of test for neutralization depth of concrete in structures with drilling powder"[5](figure.1). More than three specimens of each part were prepared (figure.1). During drilling, the powder were exposed in phenolphthalein solution, the carbonation depth was measured when the powder changed red-purple.

Fig.1 Method of test for neutralization depth

3.3 Observation site

(1) In the Philippines

8 structures in near metro Manila were investigated. There are 6 education facilities: the age of 14, 15, 16, 25, 30, 35years, and one house: the age of 40years, one church: the age of 60years.

(2) In Laos

5 structures in Vientiane were investigated. There are 5 educational facilities: age of 46

(3) In Japan

To compare carbonation speed between countries we used carbonation data in Japan[6]. There are 2 educational facilities: age of 18, 49years, 2 medical facilities: age of 13, 29years, 2 office: age of 13, 23years, 4 houses: age of 21, 23, 24, 26years, and 1 hotel: age of 24.

4. Result and Discussion

4.1 Present condition

Figure.2 shows carbonation depth in each building. As you can see, carbonation depth is big in Japan compare with in Philippine and Laos. Furthermore,

carbonation depth is big in Laos compare with in The Philippines. It was consider that it is much

4.2 Effect of precipitation and paint

Figure.3 shows carbonation speed coefficient in case of not painted concrete and painted concrete. As you can see, it is obvious that carbonation depth is small in case of painted concrete in all countries. Especially in the DLSU building, painted carbonation depth become 1/4.24 times compare to no painted carbonation depth. It was consider that, in the DLSU building, repaint was conducted every five year, therefore, the paint was kept in good condition.

Figure.4 shows effect of precipitation. And Figure.5 shows effect of temperature. From these figure effect of precipitation is larger than temperature.

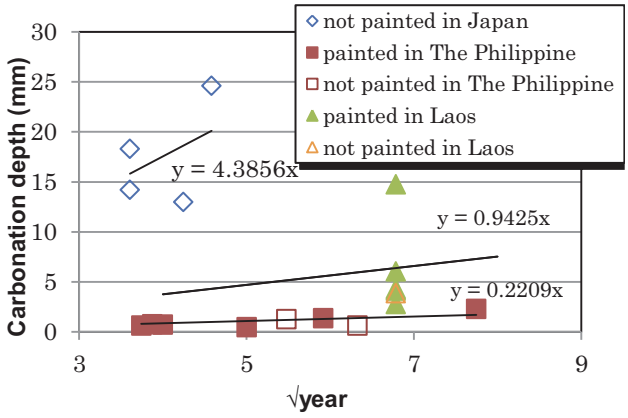

Fig.2 carbonation depth each countries

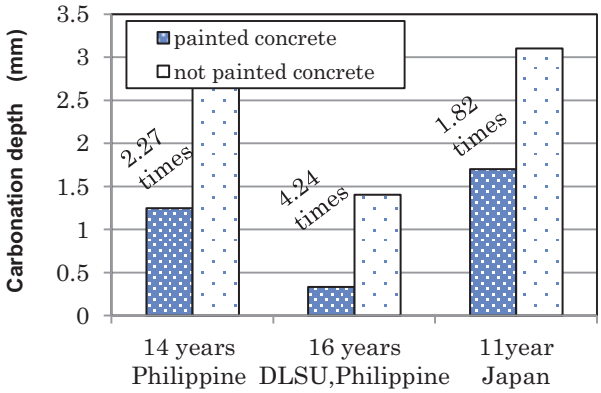

Fig.3 Paint resistance by comparing same concrete[7]

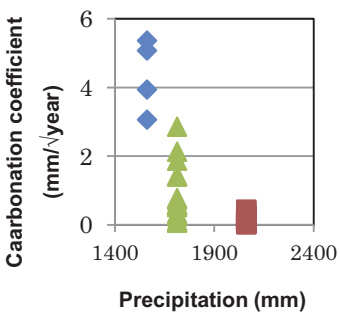

Figure.4 Effect of precipitation

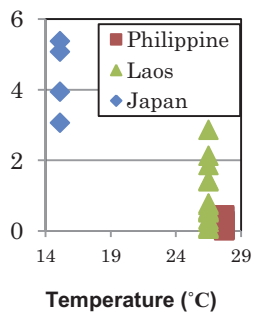

Figure.5 Effect of temperature

5. Conclusion

The conclusions of this study are as follows:

(1) Carbonation speed in the Philippines and Laos is small compare with in Japan.

(2) There is effect of paint and precipitation.

【Reference】

[1]Nobuaki Otsuki and Shinichi Miyazati (2003) .コンクリート材料. Asakura Publishing.

[2]Kenichi Hisaka (1996). 物理化学. Asakura Publishing

[3]Takeru Tsuich,Michihiko Abe, Tadatsugu Kage, Takuya Hasegawa ; “屋外暴露による中性化に及ぼす各種環境条件の影響”, Architectural Institute of Japan

[4]Masanori Kono, Keisuke Masuda, Takanori Okihashi Yusuke Nakamura; “Study on the Prediction of Carbonation Progress of Concrete Considering the Aging of Coating Materials for Textured Finishe on Diffusion Theory”, Cement Science and Concrete Technology

[5]NDIS 3419, “Method of test for neutralization depth of concrete in structures with drilling powder”, The Japanese Society for Non-Destructive Inspection

[6]Kasami Hideo; “Carbonation of Concrete and of Rainforcing Bars in Exiting Structures up to 55 Years Old”, Architectural Institute of Japan

東アジア-北米航路のコンテナ荷動き量予測モデル

学籍番号：08-15498　氏名：タニ　ウン　指導教員：花岡伸也

１．はじめに

世界定期コンテナ航路において、アジア－北米、アジア－欧州、アジア域内の荷動き量が多く、重要な航路と認識されている。2011 年 11 月のアジア 18 国と地域(日本、韓国、台湾、中国、香港、マカオ、シンガポール、フィリピン、マレーシア、インドネシア、タイ、カンボジア、ベトナム、シャンマー、インド、パキスタン、スリランカ、バングラデシュ)発の北米航路では、中国（64.6%)、韓国(5.6%)、日本（5.1%)、台湾(4.0%)の東アジアが上位４ヶ国を独占しており、全体の約８割の荷動き量を占める。

北米往航の荷動き量は「荷動きの伸び率は実質経済成長率の３掛け」ということが知られている。米国の実質 GDP と北米往航荷動き量の相関係数は 0.89 と強い正の相関がある。このように、GDP を利用すれば荷動き量との関係から将来の大まかな予測を行うことが出来る。しかし、GDP はデータの頻度が四半期ごととのため、月次レベルの予測を行うことができない。月次レベルの予測が可能になると、船社の供給量予測に活用でき、より実用的である。

本研究では、月次レベルの経済指標データを用いて、東アジア 4 ヶ国（中国、韓国、日本、台湾）積み米国揚げの北米航路の荷動き量予測モデルを構築する。構築したモデルから荷動き量への波及経路を明らかにし、荷動き量に最も影響する変数を特定する。さらに、その経済指標は何期後に荷動き量に影響を与えるか解明する。最後に、中国、韓国、日本、台湾発北米着の 4 航路のパラメータを比較する。

２．研究の方法

2.1 手法

時系列データを用いて、何期前の変数が荷動き量に影響を与えるかを考察する。現在の荷動き量を過去の値で説明するベクトル自己回帰（VAR）モデルを用いる。

VAR モデルで用いる時系列データは定常でなければならない。山本(1998)は定常の三つの条件として、①データの平均が時間を通じて一定、②データの分散が時間を通じて一定、③データの自己共分散が時間を通じて一定、を挙げている。トレンドを持った変数、つまり不定常な変数同士を推計すると、本来それほど相関は高くなくても当てはまりがよくなる。両変数のトレンド要因を取り除いて推定するほうがより正確な推計が出来るため、データの定常性を事前に確認する必要がある。データの定常性には、単位根検定によって確認できる。

本研究は、ADF(Augmented Dickey-Fuller)検定を EViews によって行う。ADF 検定の考え方は（2－1）式を推計してα＝１かどうかを調べる。α＝１であれば単位根が存在することになる。ｔはタイムトレンドであり、推計期間の始まりを１として、１ずつ増えていく変数である。

$$X_t = \alpha X_{t-1} + \sum_i \beta_i \Delta X_{t-i} + \mu + \delta t + u_t \quad (2-1)$$

単位根検定の結果、データが定常の場合はそのまま VAR モデルを求めてよいが、不定常の場合は定常にする。経済変数の回帰分析では、非定常な時系列は階差や成長率（対数階差）をとることにより、定常になることが多い。

階差：$\Delta y_t = y_t - y_{t-1}$

成長率：$r_t = \frac{y_t}{y_{t-1}} - 1 = \log y_t - \log y_{t-1}$

データを定常にした後、VAR モデルのパラメータ推定を行う。

2.2 利用データ

東アジア－北米航路の荷動き量に影響すると考えられる経済指標は、①荷動き量（日本海事センター）、②東アジア各国の対米ドル為替レート（ニューヨーク連邦準備銀行）、③米国の鉱工業生産指数(FRB:連邦準備制度理事会)、④アジア－北米のコンテナ運賃（中国国際海運網）、以上の四つである。なお、括弧内はデータの出典である。荷動き量の単位は TEU で、他のデータは指数である。

３．結果と分析

3.1 結果

ADF 検定の結果、不定常と判定されたデータを対数や対数階差を取ることにより定常化した。表１はデータの定常化後、再度 ADF 検定を行った結果を示している。

表１　定常化後のADF検定の結果(中国航路)

変数量 / 代入数値		鉱工業生産指数	為替レート	コンテナ運賃	荷動き量
原数値	t	-2.43	-1.22	-2.48	-3.49
	R^2	0.38	0.02	0.08	0.15
対数	t	**-2.45**	-1.05	-2.30	-6.71
	R^2	**0.38**	0.02	0.07	0.77
対数階差	t	-1.64	**-8.35**	**-8.75**	**-6.71**
	R^2	0.47	**0.51**	**0.53**	**0.77**

各変数において、アンダーラインを付けた数

値は、すべての代入数値の中で比較的 t 値と決定係数が高い。したがって、それらの数値には単位根が存在しない可能性が比較的高いと示唆され、VAR モデルのパラメータ推定に用いる。これより、中国航路は鉱工業生産指数の対数値、為替レート、コンテナ運賃、荷動き量の対数の階差を用いて推定する.

日本、韓国、台湾航路では、為替レートと荷動き量のデータについて、全て対数階差対応を取って定常化したデータを用いる。

VAR モデルを推計するとき、何期前までラグを取るか決定する必要がある。本研究では、一般的に使われている赤池情報量基準（AIC）を用いて決定する。分析の結果、各国の最適ラグ数の結果は、中国と韓国が２、日本が６、台湾が５となった。ラグ数が小さ過ぎると誤差項の作用が大きくなることと、各地域のモデルを比較するために、ラグ数は４に合わせた。

以上のようにして、ADF 検定によりデータを定常化し、AIC によりラグ数を決定したうえで、VAR モデルを構築した。t 値などの統計量から、統計的に有意でないラグ変数を除き、荷動き量を Y、コンテナ運賃を X、為替レートを Z、鉱工業生産指数を W、c を定数項とすると中国、韓国、日本、台湾それぞれの VAR モデルは以下のようになる。

中国：

$$Y_t = -0.209Y_{t-1} - 0.167Y_{t-2} + 0.241Y_{t-3} + 1.688Z_{t-1} - 2.844W_{t-4} - 0.191c$$

(R^2=0.249)

$$X_t = -0.180X_{t-1} - 0.236X_{t-2} + 1.789\mathrm{W}_{t-4} - 0.173\mathrm{c}$$

(R^2=0.155)

$$Z_t = 0.016Y_{t-1} - 0.244Z_{t-2} - 0.361Z_{t-3} + 0.291W_{t-1} - 0.114c$$

(R^2=0.307)

$$W_t = -0.018X_{t-1} - 0.026X_{t-2} + 0.025X_{t-3} + 1.105W_{t-1} - 0.250W_{t-4} + 0.058c$$

(R^2=0.986)

日本：

$$Y_t = -0.760Y_{t-1} - 0.864Y_{t-2} - 0.549Y_{t-3} - 0.269Y_{t-4} + 0.933X_{t-4} - 4.474W_{t-1} + 3.040W_{t-4} - 0.636c$$

(R^2=0.562)

$$X_t = -0.192X_{t-1} - 0.229X_{t-2} + 0.304Y_{t-2} + 0.237\mathrm{Y}_{t-2} - 0.614Z_{t-2} - 0.099\mathrm{c}$$

(R^2=0.269)

$$Z_t = 0.178Z_{t-1} - 0.222Z_{t-3} + 0.690W_{t-1} - 0.760W_{t-2} + 0.527W_{t-4} - 0.021c$$

(R^2=0.187)

$$W_t = -0.022X_{t-1} - 0.030X_{t-2} + 0.023X_{t-3} + 0.020Y_{t-4} + 1.142W_{t-1} - 0.261W_{t-4} + 0.053c$$

(R^2=0.987)

韓国：

$$Y_t = -0.133Y_{t-2} - 0.203Y_{t-4} - 0.372Z_{t-2} - 3.102W_{t-1} - 0.260c$$

(R^2=0.178)

$$X_t = -0.197X_{t-1} - 0.316X_{t-2} + 0.153Y_{t-1} + 2.012\mathrm{W}_{t-4} - 0.311c$$

(R^2=0.237)

$$Z_t = -0.209Z_{t-1} - 2.050W_{t-2} + 0.343c$$

(R^2=0.266)

$$W_t = -0.021X_{t-1} - 0.033X_{t-2} + 0.064Z_{t-4} + 1.013\mathrm{W}_{t-1} - 0.218W_{t-4} + 0.019Y_{t-1} + 0.039c$$

(R^2=0.989)

台湾：

$$Y_t = -0.611Y_{t-1} - 0.292Y_{t-2} - 0.250Y_{t-3} - 0.213Y_{t-4} - 2.217Z_{t-4} - 0.586c$$

(R^2=0.394)

$$X_t = -0.199X_{t-1} - 0.228X_{t-2} + 1.982W_{t-4} - 0.217c$$

(R^2=0.200)

$$Z_t = 0.713Z_{t-1} - 0.481Z_{t-2} + 0.459Z_{t-3} - 0.048X_{t-2} + 0.051\mathrm{c}$$

(R^2=0.453)

$$W_t = -0.021X_{t-1} - 0.029X_{t-2} + 0.019X_{t-3} + 0.016X_{t-4} + 0.182Z_{t-4} + 1.115W_{t-1} - 0.164W_{t-4} + 0.049c$$

(R^2=0.988)

3.2 結果の比較と考察

以上の結果から、各変数の関係および荷動き量への波及を考察する。各航路では、最も今の荷動き量に影響があるのは 1 期前から 4 期前までの荷動き量で、鉱工業生産指数にも影響を受けている。その中でも、航路によって異なる結果が出た。中国航路では、4 期前の W と 1 期前の Z も今期の荷動き量に影響がある。韓国航路では、2 期前の W と 2 期前の Z が荷動き量に作用する。日本航路では、1 期と 4 期前の W と 4 期前の X から今期の荷動き量を予測することができる。台湾航路は、4 期前の Z が荷動き量に関係している。

４航路において、為替レートは他の指数にあまり影響を受けていないことがわかる。鉱工業生産指数は今期の値が 1 期前と 4 期前の指数に対して強い自己相関性を持っていることを示している。今期のコンテナ運賃は 1 期前の荷動き量と 4 期前の鉱工業生産指数に作用をうけている。

４.結論

東アジア－北米航路について、中国、日本、韓国、台湾の４航路について VAR モデルを用いて荷動き量予測モデルを構築した。その結果、航路間の相違点と共通点を考察出来た。しかし、利用したデータ以外に、CLI（OECD の景気複合先行指数）、船腹量、LEI（経済先行指数）も荷動き量に影響する可能性がある。これらの数値を用いれば、より信頼性の高いモデルを構築出来る可能性がある。これらの変数を用いてモデルを構築することが今後の課題である。

参考文献

[1]飯塚信夫・加藤久和(2008) : EViews による経済予測とシミュレーション入門，日本評論社。
[2]山澤成康(2010)：実戦計量経済学入門，日本評論社。
[3]山本拓（1988）: 経済の時系列分析，創文社。

SAFETY SPACE FOR CAR AND MOTORCYCLE IN THE MIXED TRAFFIC FLOW IN VIETNAM

Student ID: 08_15972 Name: Chu Van Hung Adviser: Shinya Hanaoka

1 Background

In recent years, the number of accidents and deaths related to transportation has increased. From results of from the traffic accidents analyses in Hanoi from 2005 to 2008, it was found that the number of deaths due to traffic accident per 100,000 persons in Vietnam is the highest in the world. The main reason owes to not keeping safety distance and reckless driving. In the capital Hanoi, the rate of collision between car and motorcycle is 48% among collision types between vehicles.

Therefore, it is needed to research more about the interactions of movements between car and motorcycle and their safe distances which the drivers should keep to avoid a possible accident when another vehicle in front brakes suddenly. The results of this research are very useful in understanding the characteristics of driving safety for the mixed traffic flow in the developing countries.

2 Concept of safety space for motorcycle and Car

The safety space for a subject motorcycle and a subject car is assumed to have a shape of an ellipse, which boundary is determined by the influence of other vehicles that affect the driving behaviors of the subject vehicle. Threshold safety space is defined as the smallest safety space that a subject vehicle (car or motorcycle) can adopt in order to avoid a possible accident. If the vehicle in front go in to the threshold of subject vehicle, rear-end crashes may occur when the vehicle in front suddenly brakes.

Suppose that a subject vehicle α travels at speed v_α at time t. If an influential vehicle β increases or decreases its speed to $v_\beta$at time t, then vehicle α will adjust its accelerationa_α, with a lag of reaction time T; to be equal to a vector derivative of a level of safety V_β for the current positionof β with respect to a relative speed vector $\overrightarrow{v_{\alpha\beta}} = \overrightarrow{v_\beta} - \overrightarrow{v_\alpha}$ as follow:

$$a_\alpha(t+T) = -\nabla_{\vec{v}_{\alpha\beta}} V_\beta \quad \textbf{(1)}$$

Equation (1) can be rewritten as:

$$a_\alpha(t+T) = -\nabla_{\vec{v}_{\alpha\beta}} A_i exp\left(-\left(\frac{x^2}{a_i{}^2} + \frac{y^2}{b_i{}^2}\right)/B_i\right) \quad \textbf{(2)}$$

Where: A_i and B_i are parameters;x, y are the distances between vehicles α and β measured on the x-axis and y-axis, respectively.

$t = time$,T=0.5s

$\tau_m, \tau_c$is relaxation time of subject motorcycle and subject car, respectively ,l_m, l_c are the lengths of motorcycle or car respectively.

Relaxation time is defined as total of reaction time and braking time of subject vehicle.

Case1: $i = 1$ Car runs in front of subject motorcycle:

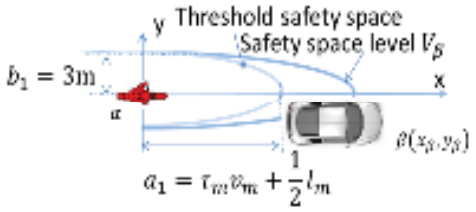

Figure1: Safety space levels for motorcycle when car runs in front of subject motorcycle.

Case2: $i = 2$ Motorcycle runs in front of subject motorcycle:

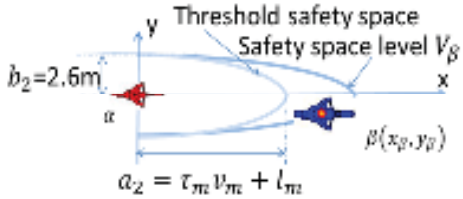

Figure2:Safety space levels for motorcycle when motorcycle runs in front of subject motorcycle.

Case3: $i = 3$ Motorcycle runs in front of subject car:

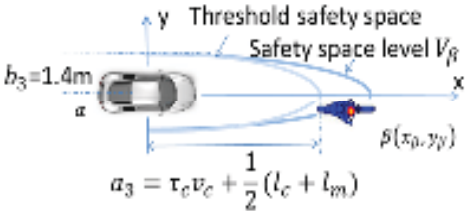

Figure3: Safety space levels for Car.

3 Data collection and parameter calibration

The survey was conducted on 30th December 2010 in Ho Chi Minh City, from 3:30 pm to 5:30 pm, to observe traffic during the peak hours.

Data on the trajectories of vehicles over time was extracted from the recorded video files using the SEV computer software.

For the case1 and case 2 considering motorcycle as subject vehicle, we used 290 observations for 37 motorcycles.

Table1: Derived parameters for case1.

Parameter	Estimate	Std. Error	95% Confidence Interval		t value	R square
			Lower Bound	Upper Bound		
A_1	6.160	1.988	2.255	10.065	3.098	0.131
B_1	0.858	0.297	0.275	1.442	2.889	
τ_m	0.357	0.071	0.219	0.496	5.057	

Table2: Derived parameters for case 2.

Parameter	Estimate	Std. Error	95% Confidence Interval		t value	R square
			Lower Bound	Upper Bound		
A_2	5.685	4.040	-2.250	13.621	1.407	0.131
B_2	0.520	0.426	-0.317	1.357	1.221	
τ_m	0.357	0.071	0.219	0.496	5.057	

For the case considering car as subject vehicle, we used 335 observations for 42 cars.

Table3: Derived parameters for case 3

parameter	Estimate	Std. Error	95% Confidence Interval		t value	R square
			Lower Bound	Upper Bound		
A_3	1.626	0.194	1.245	2.007	8.381	0.317
B_3	20.338	8.143	4.344	36.332	2.498	
τ_c	1.760	0.918	-0.043	3.563	1.917	

Sequential quadratic programming of SPSS software was used to estimate parameters (Table1, 2, 3).

$A_1, B_1, A_2, B_2, A_3, B_3$ are parameters in equation **(2)** of cases $i = 1,2,3$.

From t-value of parameters, we understand that the proposed model formulation have high reliability. The value of relaxation time $\tau_m = 0.357$s means that when driving on mixed traffic flow of Vietnam, motorcycle drivers should pay high attention, use braking often, and response rapidly to avoid rear-end crashes to happen.

Relaxation time τ_c=1.76s of car is higher than the motorcycle. It means that in mixed traffic of Vietnam, the motorcycle shows zigzag movement; therefore, the car keeps a larger safety space than motorcycle.

4 Discussions

With average speed of subject motorcycle=7.56m/s threshold safety of subject motorcycle will be drawn as below:

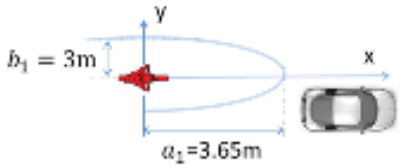

Figure4: Threshold safety space for subject motorcycle of case 1.

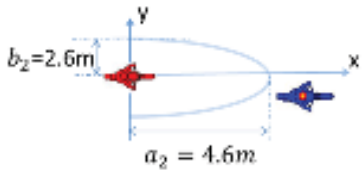

Figure5: Threshold safety space for subject motorcycle of case 2.

With average speed of subject car=7.16m/s threshold safety of subject car will be drawn as below:

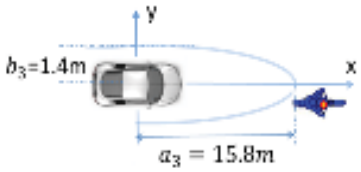

Figure6: Threshold safety space for subject car of case3

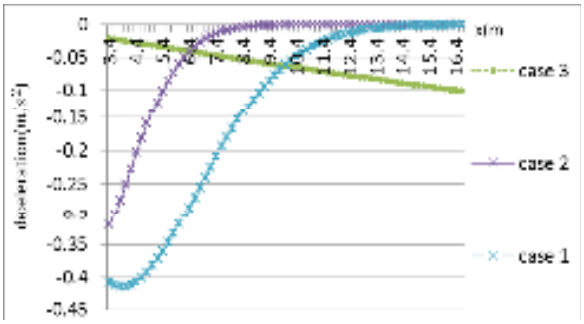

Figure7: Decelerations of subject vehicles for the case of $i = 1,2,3$ depend on the distance of subject vehicle from another vehicle ahead.

From Figure 7, we understand that, for case 1, when a car approaches nearer the subject motorcycle, the subject motorcycle will decelerate more than that of the case 2, when another motorcycle approaches the subject motorcycle in the same distance.

Deceleration of subject car (case 3) is different with the deceleration of subject motorcycle in case 1 and case 2. Owing that the size of car is bigger than the size of motorcycle and because of subject car is tend to keep a long safe distance with the motorcycle on ahead, so after identify that the motorcycle on ahead approached, subject car will decelerate larger from a far distance on ahead.

5 Conclusions

By using the concept of safety space for car and motorcycle and considering the interaction between them, this research achieved to construct a model driving behavior of vehicles considering 3 cases: The case of when car runs in front of subject motorcycle, the case of when motorcycles run on ahead of subject motorcycle and the case of when motorcycles run on ahead of subject car.

This research also estimated parameters from proposed mathematic model and quantified threshold safety space for car and motorcycle.

By comparing the acceleration of car and motorcycle, this research could explain the difference between driving behavior of car and motorcycle when the influencing vehicle on a head change its speed.

Enhancement of the composting of sub-critical water-treated food waste using acetic acid-degrading yeast

Student Number: 08-16470 Name: Songhua Zheng Supervisor: Kiyohiko NAKASAKI

1 Introduction

In the preliminary experiment, it was confirmed that composting of the sub-critical water-treated food waste (STFW) cannot be performed successfully in short time enough to carry out practically. It is known that when the pH of the raw composting material is low, it takes extremely long time for the composting [1], therefore, the low pH characteristic of the STFW was considered to cause the delay in the composting time. It was also confirmed previously that high concentration of acetic acid is contained in the STFW, which is one of the components that decrease the pH of STFW. In this study, isolation of acetic acid-degrading microorganisms and modification of the STFW using the isolated microorganisms for the enhancement of composting of STFW were attempted.

2 Materials and methods

2.1 Acetic acid-degrading microorganisms

Compost product was used as inoculum and added to BS medium containing 0.3% of acetic acid. After the cultivation at 30 °C for 4days, the culture was spread on the BS agar medium containing 0.3 % acetic acid and incubated for 30°C for 4day. Colonies appeared on the agar medium were isolated as acetic acid-degrading microorganisms.

2.2 Acetic acid degradation by the isolates in a liquid medium

Isolated strains RB1 and CM1 were inoculated to TS medium where acetic acid was added. Then, cultivation was carried out at 30°C for 48 h. aliquot of samples were withdrawn and subjected to the measurement of acetic acid concentration by HPLC.

2.3 Dependence on pH for the degradation of acetic acid by RB1

STFW was sterilized prior to the inoculation of strain RB1. Lab-scale experimental set-up consisted of a mini-reactor and an incubator to maintain the temperature at 30°C. Air was supplied at the flow rate of 5.5 ml/min and the exhaust gas was captured to measure the gas volume and CO_2 concentration once daily. Four runs with different pH values of 5, 6, 7, and 8 adjusted by addition of $Ca(OH)_2$ were conducted for 5 days during which the cell density of strain RB1, pH, and concentration of acetic acid were monitored every 24 h.

2.4 STFW composting

Inoculation of strain RB1 was carried in tandem with pH adjustment to 5.0 by addition of $Ca(OH)_2$ to the sterilized STFW at the start of experiment. Composting temperature was set at 30°C during the first 5 days. At day 5, pH of compost was adjusted to 8.0 and seeding materials of Alles G was inoculated. Then, incubation temperature was raised to 60^{o}C and kept constant throughout the composting of 7 days. The degradation of organic matter was monitored by CO_2 emission. The details of composting system is shown in Fig 4.

3 Results and discussion

Two yeast strains that can degrade acetic acid were isolated and named CM1 and RB1. A picture of the colonies of the RB1 is shown in Fig. 1.

Fig. 2 shows the course of concentration of acetic acid in the TS medium where RB1 and CM1 were inoculated. The initial concentration of acetic acid was 5.5 g/L and after 48 h cultivation, it decreased to 1.3 g/L for the culture with RB1 and to 2.2 g/L for the culture with CM, suggesting the higher degradation ability of RB1 compered to that of CM1. Based on the results, we focused the RB1 and preferable pH condition for RB1 to degrade acetic acid in the STFW was investigated.

Fig. 1 The picture of the colonies of RB1.

Fig. 3 shows the course of acetic acid concentration in the STFW of which pH was adjusted to the intended values during the experiment. RB1 showed highest acetic acid-degrading capability in the experiment at pH 5 where the concentration of acetic acid decreased from 0.0173 g/g-ds to 0.0047 g/ g-ds. Therefore, composting of STFW after the degradation of acetic acid contained in STFW by RB1 at the condition of pH 5 was carried out in large scale apparatus.

Fig. 4 shows the courses of emittion rate of CO_2 and cumulative emittion of CO_2 during the experiment using large scale apparatus. The cumulative emittion of CO_2 increased steadily during the experiment and it was confirmed that the composting of STFW was successfully conducted in 7 days that was short time enough to carry out practically after the pretreatment by RB1 for 5 days.

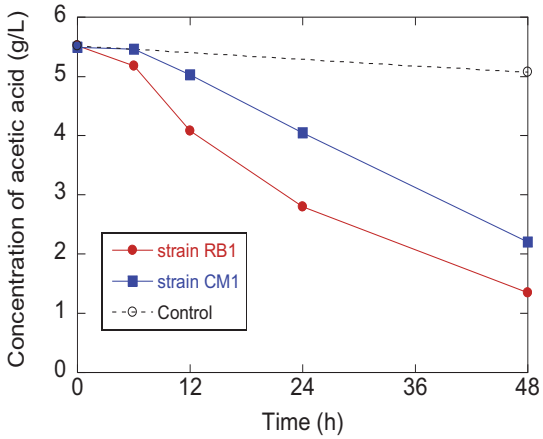

Fig. 2 The courses of acetic acid concentration in TS medium inoculated with RB1 and CM1.

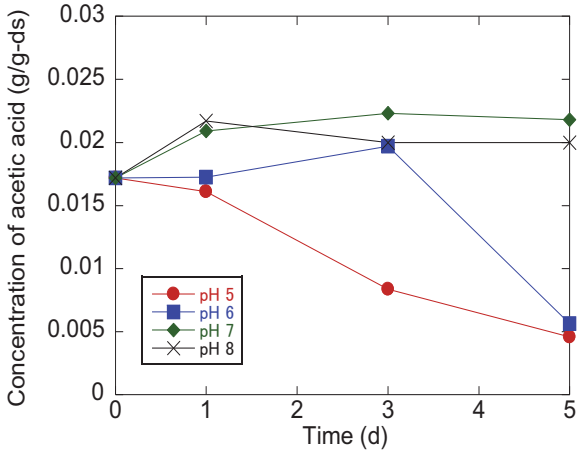

Fig. 3 The courses of acetic acid concentration in STFW of which pH were adjusted at 5, 6, 7 and 8.

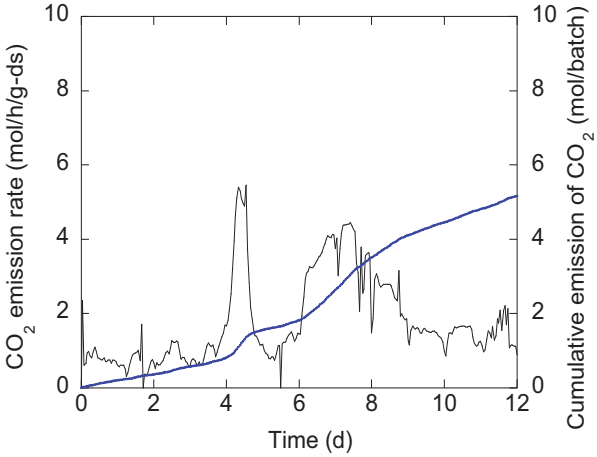

Fig. 4 the courses of emittion rate of CO_2 and cumulative emittion of CO_2 during the experiment using large scale apparatus.

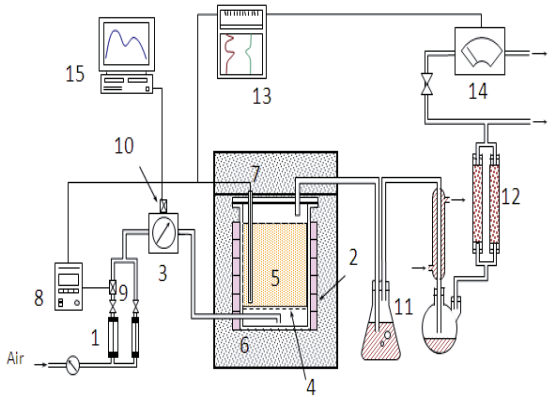

1. Flow meter	6. Styrofoam insulator	11. Ammonia trap
2. Ribbonheater	7. Thermocouple	12. Silicagel adsorber
3. Gas meter	8. Temp.controller	13. Recorder
4. Perforated plate	9. Solenoid valve	14. CO_2 analyzer
5. Reactor	10. Pulse transmitter	15. Micro-computer

Fig. 5 Schematic diagram of the experimental set up with a large scale apparatus.

4 Conclusions

Acetic acid-degrading microorganism of CM1 and RB1 could be isolated and it was clarified that RB1 have higher acetic acid-degrading ability than CM1. Furthermore, composting of STFW could be carried out successfully in short time enough to conduct practically after the pretreatment of STFW by RB1 at the condition of pH5 that was determined to be preferable for RB1 to degrade the acetic acid.

References

[1] K.R. Keehan : PB Report, 479-491 (1991)

Consideration of stress distribution in an antlion's nest using advantage of angle of repose

Student Number: 08B16760 Name: Lin TANG Supervisor: Thirapong PIPATPONGSA

1 Introduction

Inverted conical sand valley represents a fundamental problem in geo-mechanics whose stress distribution has not been clearly solved. This problem can represent a condition of antlion's nest (see Fig.1) for small scale and a condition of open-pit mine (see Fig.2) for large scale. Spider and antlion are only insects which can trap other insects. In Geotechnical Engineering's view point, antlion employs advantage of angle of repose to trap small insects by digging conical pits in loose sand. When a small insect, commonly an ant, falls into the pit, its weight causes instability of the pit; hence cascading the victim down to the bottom of the pit where antlion is waiting for. Despite of different scale and boundary conditions, complicated problem on stress distribution in open-pit mine would be able to simplify to that of antlion's nest. Therefore, investigation of antlion's nest and its physical model was conducted in this study.

2 Trajectories of principal stresses

Granular slope inclining at an angle of repose physically exhibits the steepest angle of descent relative to the horizontals where slope face is on the verge of sliding. The fixed principal axes (FPA) closure is considered as an ad hoc explanation about trajectories of principal stresses (see Fig.3). Based on the, the angle of major principal direction ψ is assumed to be fixed on each half of the sand valley which is determined from the state of stress adjacent to the failure plane.

3 Experiments and results

The experiment includes two parts, antlion's nest experiment and sand crater physical modeling.

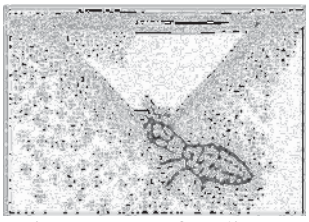

Fig.1 Image of antlion catching an ant

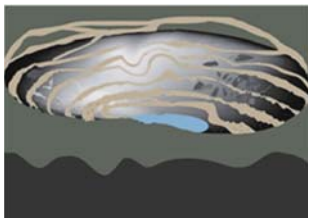

Fig.2 Illustration of open-pit mining

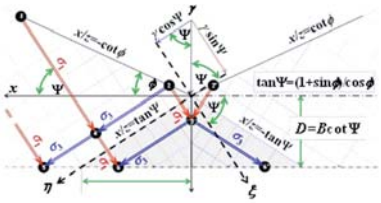

Fig.3 Networks of principal stresses in sand valley under the closure of FPA

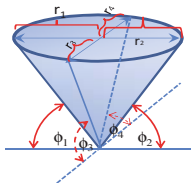

Fig.4 Description of geometry of antlion's nest

3.1 Antlion experiment

The material used in antlion experiment is silica sand 8 and 6. Ten healthy antlions were putted into 10 paper cups filled with sand. The height of pit was measured after pit was dig. Angle of repose can be computed from maximum and minimum width of the pit. The geometry of angle φ1, φ2, radius r1, r2 in principal axis and angle φ3, φ4, radius r3, r4 in second axis are described in Fig.4. Experimental results for angle φ, radius r, void ratio e, relative density D_r are shown in Table1, showing that density of silica sand no.8 is relatively larger than that of no.6 Box shear test was carried out to find friction angle of both sand and reported to Table 2 with other sand's properties.

Table1 experiment results in antlion's nest

average	r1(cm)	r2(cm)	r3(cm)	r4(cm)	angle1 (deg)	angle2 (deg)	angle3 (deg)	angle4 (deg)	e	Dr(%)
silica sand 8	1.00	1.35	1.02	1.25	39.47	31.17	38.51	33.15	0.82	81.21
silica sand 6	1.33	1.80	1.38	1.63	44.49	35.88	43.31	38.74	0.90	53.94

Table 2 physical nature of silica sand 8 and 6

material	angle of friction(deg)	e_max	e_min	Gs
silica sand 8	ϕ =32.7	1.333	0.703	2.65
silica sand 6	ϕ =35.6	1.132	0.711	2.65

Table 3 Testing program of physical model of sand crater in a rectangular bin

Test	1	2	3	4	5
[1]SPM	[2]AP	AP	[3]DP	AP	DP
[4]H_f	20	20	20	30	30

Note: [1]SPM=sample preparation method; [2]AP=air pluviation technique; [3]DP=dry deposition technique; [4]H_f=final height of excavation

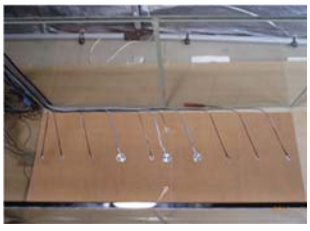

Fig. 5(a) Outline of embedded gauges (left)

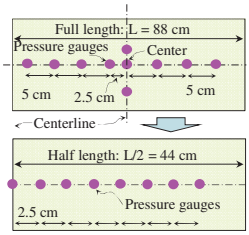

Fig. 5(b) Alignment of pressure gauges (right)

3.2 Physical modeling of sand crater

A summary of the tests undertaken is given in Table 3. The physical model of load transmission beneath the sand crater in the transparent plastic rectangular bin was carried out on 5 samples of dry silica sand no.8. The geometrical dimensions are, length L = 88 cm, width W = 38 cm, and height H_b = 49.5 cm. The scale was stuck on the edge of the bin. A series of low capacities of pressure cells were employed for the

highly accurate and precise measurement of the low pressure induced by self-weight of tested sand stored in rectangular bin. The vertical pressures of the granular material exerting to the floor were measured by twelve miniature pressure gauges, 9 of which have 10 mm in diameter and a maximum capacity of 20 kN/m^2, and other three 25 mm and 20 kN/m^2 as shown in Figs. 5(a) and 5(b). As outlined in Fig. 5, 3 pressure gauges were installed at centerline, 4 on the right and 5 on the left asymmetrically in order to effectively catch a pressure profile by a limited number of sensors. A half plane of the physical model can be simply considered due to its symmetrical geometry. As the sample preparation is one of the most important aspects for soil testing, the uniformity of the sample has been a major concern. Various techniques from theoretical and experimental viewpoints have been proposed to reconstitute homogeneous samples. Therefore, the sand samples of 20 cm and 30 cm height were prepared by two techniques (air pluviation and dry deposition) as described in Table 3 to observe the discrepancy of load transmission underneath the sand crater in rectangular bin. For each technique, sands were deposited in a bin at a constant 2 cm drop height in order to obtain loose samples. Sands as to air pluviation technique were filled in a physical model bin with a rate 2 kg/min pouring from the plastic bottle having the bigger cross section with a small sieve opening of 1 mm at the bottom. In regard to dry deposition technique, sands were spread with a rate 5 kg/min into the center of the bin through cap-opened plastic bottle with a 2.2-cm-diameter nozzle. Then, the vacuum with a sharp tube was used to suck sand along the centerline; therefore, a conical crater was formed by successively sand avalanches inclining at the angle of repose. The sand was excavated until the final depth (H_f) reaches 12 cm.

As shown in Fig. 6, the vertical pressure σ_v measured along the floor of the physical model normalized by its geostatic pressure γH was plotted against χ representing the distance from the centerline along the floor normalized by half length L/2. The diamond, rectangular, triangular, and circular symbols denote a chain of pressures undergoing the excavation stages at depth 0 cm, 4 cm, 8 cm, and 12 cm, respectively.

4 Discussion and conclusion

Angle of repose for loose sand represents its friction angle. By comparing Table1 and Table2, angle formed in antlion's nest is larger than the friction angle; thus indicating that antlion's nest is on meta-stable state, even a little movement can cause collapse of its nest. According to experimental result of physical model, stagnant of pressure change at the center is clearly observed, because the pressure does not transfer to the base for deep overburden layer. However, a central pressure dip can be observed later once the excavation process is continued and passed the critical depth which is consistent with FPA closure.

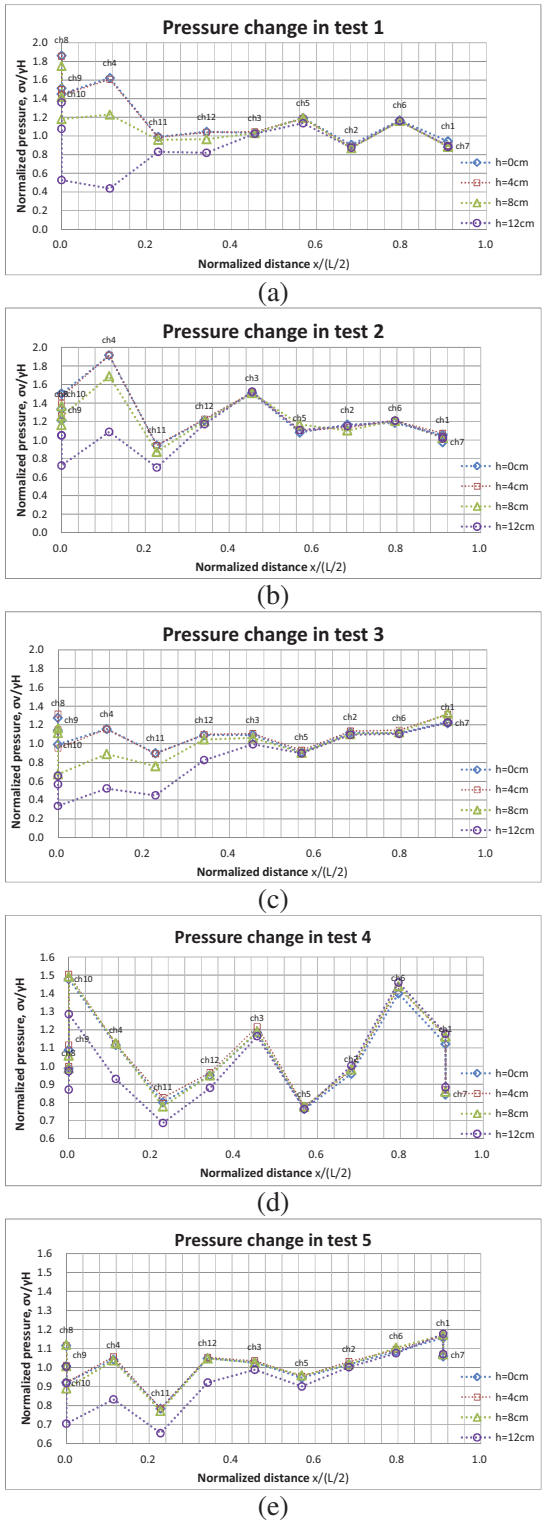

Fig.6 Pressure changes on the base of sand valley during excavation process for Test 1 to Test 5 using silica sand no.8

References

[1] Wittmer, J.P., Claudin, P., Cates, M.E., Bouchaud, J.P., An explanation for the central stress minimum in sand piles. *Nature*, 382(6589), 336-338, 1996.

[2] T. Pipatpongsa, S. Heng, A. Iizuka and H. Ohta, Statics of loose triangular embankment under Nadai's sand hill analogy, *Journal of the Mechanics and Physics of Solids*, Vol.58(10), 1506-1523, 2010.

Magnetic Shielding from Solar Energetic Particles for Manned Deep Space Explorations

Student Number: 08-17787 Name: Yasuhito Nakatani Supervisor: Yoshihiro Mochimaru

1. Introduction

Shielding from Solar energetic particles (SEPs) is one of the most difficult problems for manned deep space explorations. SEPs are high energetic particles emitted from the Sun in case of a solar burst. Most of SEPs are protons. We are protected from SEPs by the earth's magnetic field and its atmosphere. In deep space, however, astronauts are at risk of exposure to SEPs, and could be exposed to more than 1 Sv SEPs during a few days of a solar burst. Big solar bursts occur several times during a 11-years solar cycle.

A major idea to protect astronauts from SEPs is to make walls of spacecraft thick, which is against deep space explorations. Another idea is to generate a magnetic field using superconducting coils for deflecting trajectories of proton colliding with a spacecraft. Figure 1 is a schematic configuration. A magnetic field generated by a loop current in a superconducting coil is expected to deflect protons. The idea has a potential to adopt less mass compared with the former. It was considered that a superconducting coil system requires huge amounts of power to generate a sufficiently intense magnetic field, for deflecting almost all protons.

In this paper, number density distribution of the solar protons around the loop current is investigated, to show effects of the diameter of the coil and those of the location.

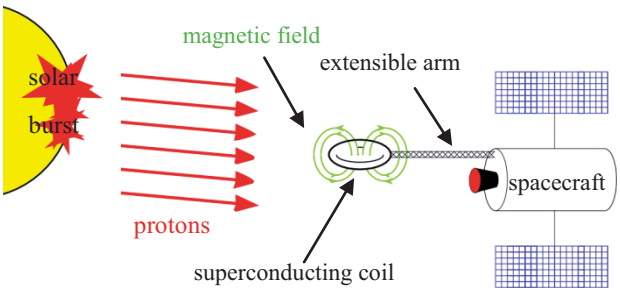

Fig. 1 Magnetic shielding from SEPs.

2. Simulation method

Figure 2 shows a computational space of $10\ \mathrm{m} \times 10\ \mathrm{m} \times 70\ \mathrm{m}$.

SEPs are assumed to be composed only of protons. The solar protons fly into the computational space from $\mathrm{X}-\mathrm{Z}$ plane at $\mathrm{Y}=-20$ m. The protons are velocities parallel to Y axis.

Since protons possessing kinetic energy less than 50 MeV are guarded by the walls of the spacecraft, the target kinetic energy E_k of the proton is assumed to be

$$50 \leq E_k\,/(\mathrm{MeV}) \leq 200 \qquad (1)$$

Proton's particle flux is assumed to be $1.0 \times 10^4\ \mathrm{cm}^{-2} \cdot \mathrm{s}^{-1}$. Their kinetic energy distribution is assumed due to. [2].

The coil is located at the oriin in the computational space. The coil plane is in parallel with $\mathrm{Y}-\mathrm{Z}$ plane. Coil's diameter d is 1.0, 2.0, 3.0, or 4.0 m. The coil current I is 10, 50, 100, 200, 300, or 400 kA. An electrical field generated by solar wind is ignored. Based on this assumption, each proton is affected by the following Lorentz force,

$$\boldsymbol{F} = q(\boldsymbol{v} \times \boldsymbol{B}) \qquad (2)$$

where $\boldsymbol{F}$:Lorentz force, q:electrical charge of a proton, $\boldsymbol{v}$:velocity of a proton, $\boldsymbol{B}$:magnetic flux density.

Equation of Proton's motion is

$$m\frac{d\boldsymbol{v}}{dt} = q(\boldsymbol{v} \times \boldsymbol{B}) \qquad (3)$$

where m :proton's mass. Eq. (3) is integrated by Runge-Kutta method.

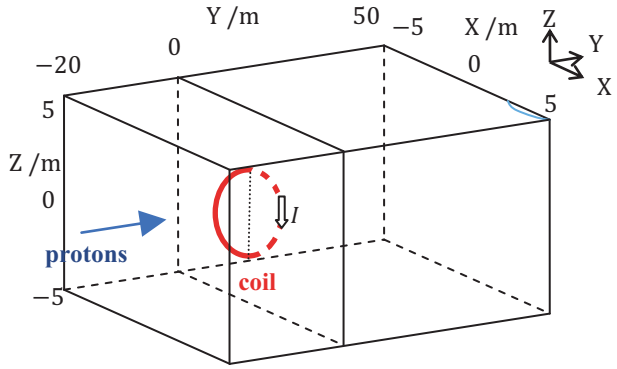

Fig. 2 Computational space (not to scale)

3. Results

3.1. Number density distribution of proton

Figure 3 shows the number density distribution of protons for d=4.0 m and I=200 kA.

The number density drops to a lower value behind the coil. Since the magnetic field's Z component is symmetrical about the coordinate origin, low number density region is symmetrical about $\mathrm{Y}-\mathrm{Z}$ plane at $\mathrm{X}=0$ m. High number density region is found above the low number density region. It is because Z axis plus directional Lorentz force.

The low density region expands along Y axis.

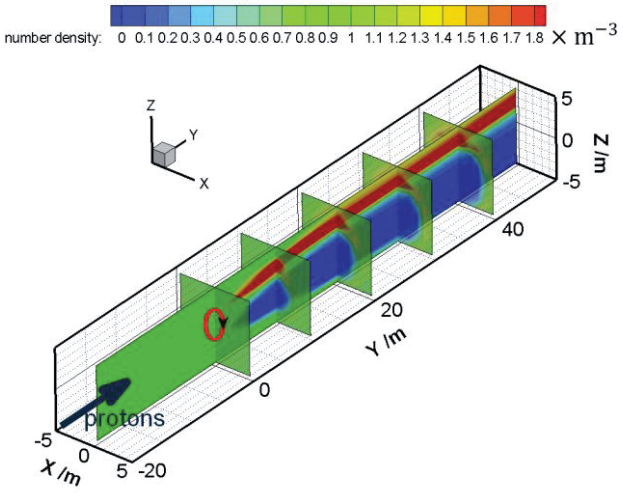

Fig. 3 Number density distribution of protons around the coil (d=4.0 m, I=200 kA)

3.2. Effects of magnetic field intensity

Figure 4 shows the number density distribution of protons for d=4.0 m and I=50 kA.

The low density region decrease in size with decrease in the coil current.

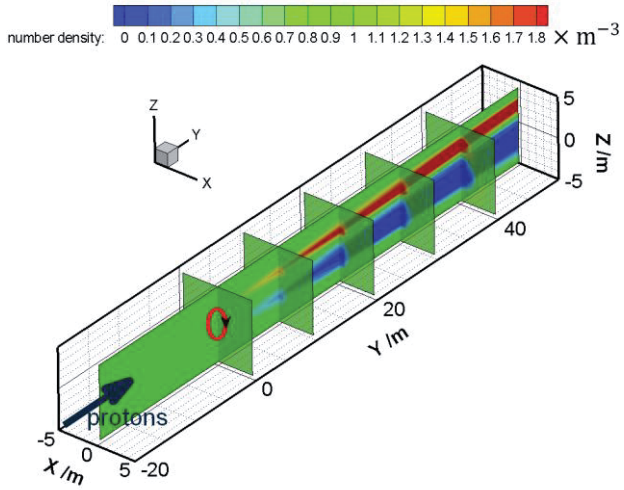

Fig. 4 Number density distribution of protons around the coil (d=4.0 m, I=50 kA)

3.3. Effects of coil's diameter

Figure 5 shows the number density distribution of protons for d=1.0 m and I=200 kA.

The low density region decrease in size with decrease in the coil's diameter.

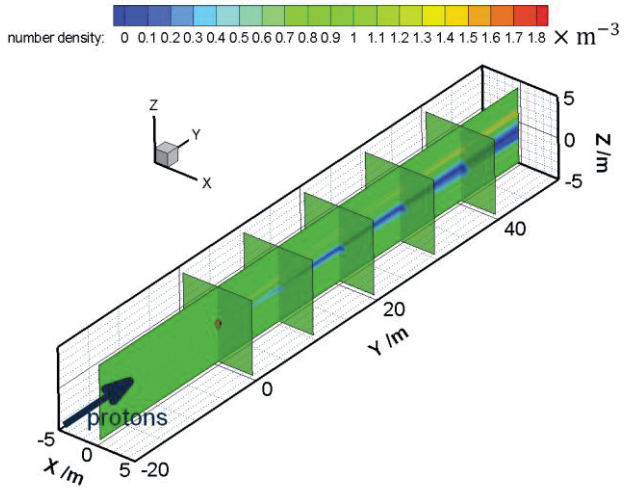

Fig. 5 Number density distribution of protons around the coil (d=1.0 m, I=200 kA)

3.4. Effects of proton's incident angle

Figure 6 shows the number density distribution when the protons have variations of the incident angle in the range of ±7.5 deg in Y-direction. The coil diameter and the coil current are d=4.0 m and I=200 kA, respectively.

In this case, some protons can fly to a region behind the coil without being affected by the magnetic field. Because of that, there is the most appropriate position in Y-direction for the spacecraft.

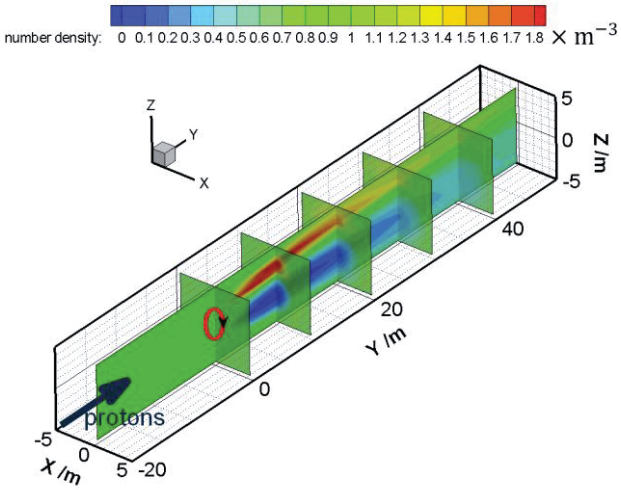

Fig. 6 Number density distribution of protons around the coil (d=4.0 m, I=200 kA,0° ≤ φ ≤ 7.5°)

4. Conclusions

The magnetic shielding could deflect most of the SEPs' trajectories even if the coil current is relatively low. Not only the amount of the current but also the coil's size and the relative position between the coil and the spacecraft are important for the magnetic shielding from SEPs.

References

[1] L. W. Townsend, J. W. Wilson, J. L. Shinn, J. E. Nealy, L. C. Simonsen, "Radiation Protection Effectiveness of a Proposed Magnetic Shielding Concept for Manned Mars Missions", SAE Technical Paper, 901343, 1990

[2] Joseph H. King, "Solar proton fluences as observed during 1966-1972 and as predicted for 1977-1983 space missions", NASA TM X-70508, 1973

[3] P. Spillantini, F. Taccetti, P. Papini, L. Rossi, "Radiation shielding of spacecraft in manned interplanetary flights", Nuclear Instruments and Methods in Physics Research Section A, Vol.443, p.254-263, 2000

[4] Tatsuzo Obayashi, "Solar Terrestrial Physics", SHOKABO, 1970

Effect of operating condition on solvent extraction of La with PC-88A

Student Number: 08_18048 Name: Kazuma NAKAMURA Supervisor: Ryuichi EGASHIRA, Hiroaki HABAKI

1. Introduction

Rare earth metals are mainly used as raw materials for high purity individual rare earth chemicals. Lanthanide elements have major applications in magnets, ceramics, electronics, nuclear technology and so on [1].

Solvent extraction is well known as an effective method for separation of lanthanides on the industrial scale. Due to the growing demand of high purity metals with the developing high-technology industry, establishing the more effective operating condition of solvent extraction is needed. 2-ethylhexyl phosphonic acid mono-2-ethylhexyl ester (PC-88A) is an acidic organophosphorus extractant. PC-88A has been widely used in solvent extraction of lanthanides industry for the separation and purification of the metal ions. However in the previous studies the concentration ranges of rare-earth metals and extractant were much lower than those used in the industrial scale. The rare-earth metal concentrations were so low relative to those of extractant in organic phases that it was assumed that the free extractant concentration could not be affected by the metal extraction. Nishihama et al. [2] reported that in the high concentration region, the extraction reaction was quite different from those in the low concentration ranges.

In the present work, solvent extraction of La with PC-88A is studied. La was selected from the rare-earth metals and the extraction equilibrium of La between the organic phases of PC88A and the aqueous phases in which the proton concentration was adjusted. Moreover the effects of La concentration in the system on the extraction equilibrium were also studied.

2. Experimental

Table1 shows the experimental conditions for distribution equilibrium measurements. The organic solutions were prepared by diluting PC-88A with solvesso150. Solvesso150 is one of the petroleum fractions, rich in aromatic hydrocarbons. The aqueous solution of nitric acid was used as the aqueous phases. La hydroxide was used as La source.

The solute, aqueous and organic phases were put into 50ml conical flasks with screw cop, and stirred with magnetic stirrer for 24h. The two phases were then separated with a separating funnel and the obtained aqueous solutions were analyzed by ICP-AES.

Table1 Experimental condition of La hydroxide extraction

Solute	$La(OH)_3$	
Aqueous phase	Aqueous solution of HNO_3	
Organic phase	Organic solution (solvesso150) of PC-88A	
Mole load relative to aqueous phase	$C_{La,aq,0}$[kmol/m^3]	0, 0.1,0.05,0.025
Concentration of nitric acid in aqueous phase .	$C_{NA,aq,0}$ [kmol/m^3]	0~0.175
Concentration of PC-88A in organic phase	$C_{RH,org,0}$[kmol/m^3]	0.5, 1.0
Volume of aqueous phase	V_{aq} [m^3]	2.0×10^{-4}
Volume of organic phase	V_{org} [m^3]	2.0×10^{-4}
Stirring time	t [h]	24
Stirring speed	v [h^{-1}]	60,000

3. Results and Discussion

3.1 Solvent extraction of La hydroxide

The extraction degree, E, is given by:

$$E = \frac{C_{La,org}}{C_{La,aq,0}} = \frac{D}{1+D} \quad (1)$$

Distribution ratio, D, is defined by:

$$D = \frac{C_{La,org}}{C_{La,aq}} \quad (2)$$

In this study, reaction is assumed to be as follows [3]:

$$La^{3+} + 3\overline{(RH)_2} \leftrightarrow \overline{LaR_3(RH)_3} + 3H^+ \quad (3)$$

where $(RH)_2$ is extractant dimmer, and $\overline{LaR_3(RH)_3}$ is extracted species. $C_{RH,org}$ is an extractant concentration as dimmer.

Dissolution of La hydroxide in water is written as follows:

$$La(OH)_3 = La^{3+} + 3OH^- \quad (4)$$

From Eqs (3) and (4), we have Eq (5):

$$La(OH)_3 + 3\overline{(RH)_2} = \overline{LaR_3(RH)_3} + 3H_2O \quad (5)$$

From Eq (5), K_{ex} is expressed by:

$$K_{ex} = \frac{C_{La,org}\times C_{H,aq}{}^3}{C_{La,aq}\times C_{RH,org}{}^3} = D \times \frac{C_{H,aq}{}^3}{C_{RH,org}{}^3} \quad (6)$$

From Eq (3), concentration of free extractant, $C_{RH,org,}$ expressed by:

$$C_{RH,org} = C_{RH,org,0} - 3C_{La,org} \quad (7)$$

The effect of initial and equilibrium H^+ concentration, $C_{H,aq}$, on the extraction degree, E, is shown in **Fig.1**. **Fig.2** shows the effect of nitric acid concentration, $C_{NA,aq}$, on the extraction degree. All La hydroxide was extracted with aqueous solution of no nitric acid and the organic phase of $C_{RH,org,0}$=0.5kmol/m^3 could extract all La in case of $C_{La,aq,0}$=0.1kmol/m^3.

$C_{H,aq}$ increased after the extraction but Eq(5) means that $C_{H,aq}$ isn't change before and after the extraction. This change may be because of PC-88A dissolved in aqueous phase. The effect of organic phase contact with water is shown in Table2. This result means that $C_{H,aq}$ is decrease without extraction.

Table2 The effect of PC-88A dissolution in 2.0×10^{-4}m^3 water

Organic phase	$C_{H,aq}$
PC-88A 0.02(kmol/m^3)	2.77
PC-88A 0.02(kmol/m^3) + solvesso150 (2.0×10^{-4}m^3)	2.84

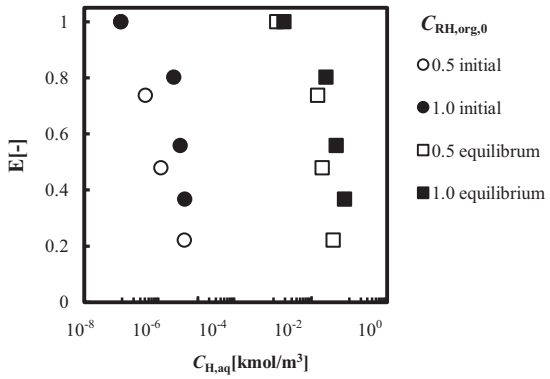

Fig.1 Effect of initial and equilibrium $C_{H,aq}$ on the extraction degree. $C_{La,aq,0}$=0.1 kmol/m^3, $C_{RH,org,0}$=0.5, 1.0 kmol/m^3

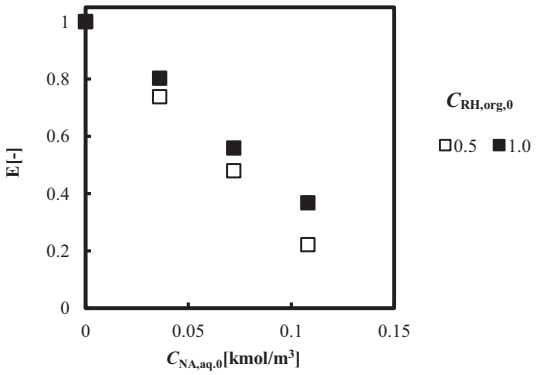

Fig.2 Effect of nitric acid concentration on the Extraction degree. $C_{La,aq,0}$=0.1 kmol/m^3, $C_{RH,org,0}$=0.5, 1.0kmol/m^3

3.2 Measurement of extraction equilibrium constant

Fig.3 shows the effect of free extractant concentration on K_{ex}. When the free extractant concentration was lower than 0.3kmol/m^3, K_{ex} was not constant. In the range of $C_{RH,org}$>0.3kmol/m^3, K_{ex} was almost constant but the value was affected by La concentration.

Fig.4 shows the slope analysis method to determine K_{ex} at each La concentration. K_{ex} could be obtained by the intercepts of the line of which solpe is 3 and pass the all plot. In **Fig.4**, Eq(3) was assumed to be able to apply each conditions where K_{ex} are constant. The obtained K_{ex} was listed in **Table3**.

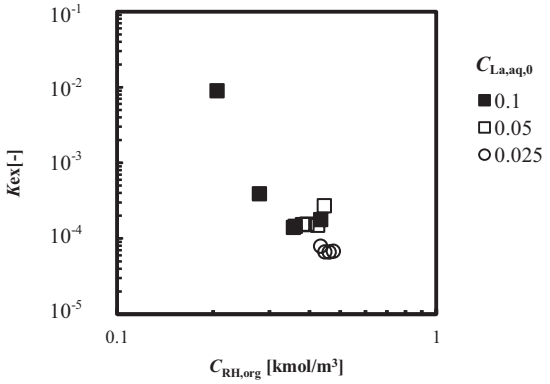

Fig.3 Effect of free extractant concentration on the extract equilibrium constant. $C_{RH,org,0}$=0.5kmol/m^3,$C_{La,aq,0}$= 0.1,0.05, 0.025 kmol/m^3

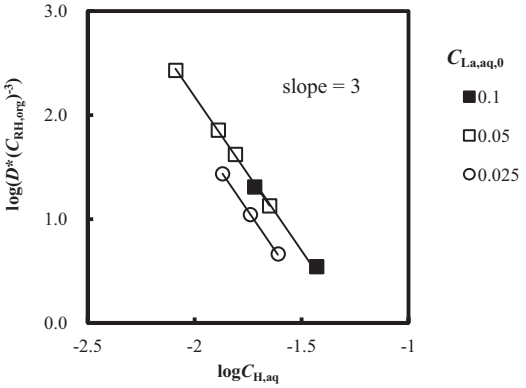

Fig.4 Determination of K_{ex} by using of slope analysis method. $C_{RH,org,0}$=0.5kmol/m^3, $C_{La,aq,0}$= 0.1,0.05, 0.025 kmol/m^3

Table3
Extraction equilibrium constants at each feed La concentration

$C_{La,aq,0}$ [kmol/m^3]	intercepts	K_{ex}[-]
0.1	3.81	1.55×10^{-4}
0.05	3.83	1.48×10^{-4}
0.025	4.18	6.61×10^{-4}

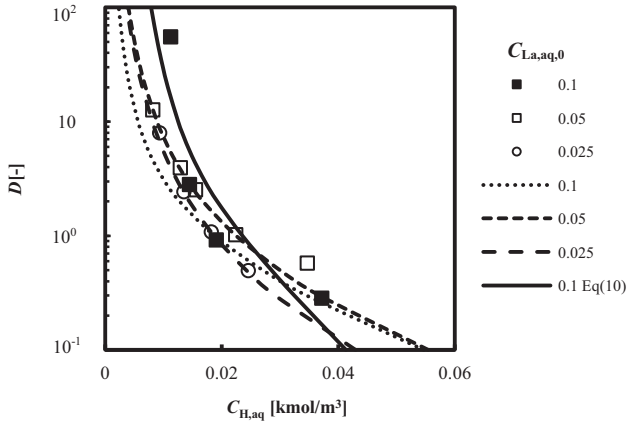

Fig.5 Effect of hydrogen ion concentration on the distribution ratio. The comparison of observed distribution ratio (plot) with predicted distribution ratio (broken and dotted line).

$C_{RH,org,0}$=0.5 kmol/m^3, $C_{La,aq,0}$=0.1, 0.05, 0.025 kmol/m^3

From Eq (6) and (7), the distribution ratio at each hydroxide concentration, could be predicted by $C_{La,aq,0}$ and $C_{RH,org,0}$.

The measured distribution ratios and the predicted distribution ratios obtained by using of the value of K_{ex} in **Table3** are shown in **Fig.5**.

The predicted distribution ratio could express the measured data well when $C_{La,aq,0}$= 0.05kmol/m^3 and 0.025kmol/m^3, but when $C_{La,aq,0}$=0.1kmol/m^3, it cannot express all distribution ratio .

To express the distribution ratio of $C_{La,aq,0}$=0.1kmol/m^3 , the extraction reaction was assumed to be Eq (8).

$$La^{3+} + 3\overline{(RH)_2} = \overline{LaR_6H_{6-m}} + mH^+ \quad (8)$$

Fig.6 shows the slope analysis method to determine m and K_{ex} in Eq(8) .

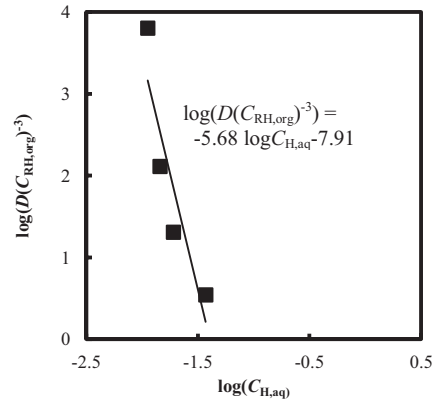

Fig.6 Determine of K_{ex} and m by using of the slope analysis method
$C_{La,aq,0}$=0.1 kmol/m^3, $C_{RH,org,0}$=1.0 kmol/m^3

Fig.6 shows that K_{ex} is $10^{-7.91}$ and m=5.68. The solid line in **Fig.5** compares the predicted obtained from **Fig.4** and **Fig.6** with measured data. **Fig.5** shows that the prediction line obtained from **Fig.6** (solid line) can express the measured plot better than that of from **Fig.4** (dotted line).

4. Conclusions

Extraction La hydroxide with PC-88A by using of solvent extraction was achieved. 0.5kmol/m^3 PC-88A was appropriate to extract 0.1kmol/m^3 feed La hydroxide and nitric acid for pH control was unnecessary.

The ratio of free extractant may have relation to the extraction reaction. And concentration of feed La has relation to the extraction equilibrium constant.

Nomenclature

C_i	= concentration of i	[kmol/m^3]
K_{ex}	=extraction equilibrium constant	[-]
E	=extraction degree	[-]
D	=distribution ratio	[-]
$(RH)_2$	=dimeric species of extractant	[kmol/m^3]

<Subscripts>
0 =aqueous or organic feed solution
aq =aqueous phase
org =organic phase
<Superscripts>
— =organic phase species

References

[1]S.Radhika,B.Nagaphani Kumar,M.Lakshmi Kantam, B Ramachandra Reddy, Liquid-Liquid extraction and separation possibilities of heavy and light rare-earths from phosphoric acid solutions with acidic organophosphorus reagents, Separation and Purification Technology75(2010)295-302

[2]Syouhei Nishihama, Takayuki Hirai, Isao Komasawa, Design of Liquid-Liquid Extraction Process for Separation of Metal ions, KAGAKU KOGAKU RONBUNSHU, 26(2000)497-505

[3]Hsiang-Chien Kao, Pei-Shin Yen, Ruey-Shin Juang, Solvent extraction of La(Ⅲ)and Nd(Ⅲ) from nitrate solutions with 2-ethylhexylphosponic acid mono-2-ethylhexyl ester, Chemical Engineering journal, 119(2006)167-174

都市境界層における大気乱流及びフラックスの年間スペクトル解析

学籍番号：08-18976　氏名：野口淡海　指導教官：神田学

1. はじめに

大気境界層乱流の周期的特性は，フラックス算定や渦スケールを知る際に重要であり，様々な地形上・場所での境界層内の乱流解析が世界中で頻繁に行われてきた．その結果 Kaimal(1977)らは，カンザスでの実験結果に基づき，乱流場でのスペクトル形を提案した．また，スペクトルギャップの有無や，等方性乱流を意味する慣性小領域の存在を示す－2/3 乗則に従う領域の存在なども，追従する研究により確認されている．しかしこれらの多くは，低周波又は短期間の解析によって得られたものに過ぎず，高周波かつ長期観測データの解析から直接示した例は，非常に少ない．それは，解析に莫大なサンプルデータを要することや，取得データの信頼性という点において，長期間(例えば年間レベル)の連続データを取得することが困難であるからである．更に，砂漠・海上・森林等での乱流観測は頻繁に行われてきたが，都市部における乱流観測は，観測用タワーの設置条件等の制約から，世界的に見てもほとんど行われていないという現状がある．

本研究では，都市部居住区に建てられた「久が原タワー」の観測データ(森脇ら，2006)をもとに，1 年間の長期データを用い，高いサンプリング周波数(8Hz)での解析を試みた．

2. 研究の目的

本研究では以下の 3 点を目的とする．

(1)高周波(8Hz)かつ長周期(1 年)の連続データ解析により，慣性小領域から総観場のスケールの連続したスペクトルを示し，スペクトルギャップの有無，慣性小領域の存在などについて直接的な検討を行う．

(2)これまでに解析されたことのない，都市部居住区での長期乱流観測データに基づくスペクトル形を示し，その特徴を見出すとともに，既往の研究との比較を行う．

(3)高性能の観測器(赤外線オープンパスアナライザー)によって得られた二酸化炭素濃度等のスカラー量の長期スペクトルを算出し，スカラー量そのものの乱流特性を発見する．

3. 研究概要

東京都大田区久が原に設置された観測タワーで取得された長期(2001～2007 年)時系列データを利用し，低層住宅地(平均高さ 7.3m)における大気乱流の風速(ベクトル)，スカラー変動スペクトルを算出する．解析には，主流方向風速(u)，主流の水平直角方向風速(v)，鉛直方向風速(w)，気温(t)，二酸化炭素濃度(c)，及び水蒸気濃度(q)の 6 つのデータを使用した．これらは，タワーにおける地上 21, 29m 地点の 2 箇所からそれぞれ得られたものである．8Hz で取得された 1 年間のデータ(データ数 252,288,000 個)を，東工大所有のスーパーコンピュータ TSUBAME2.0 を用いて FFT 演算し，パワースペクトル及びコスペクトルを出力させた．解析原理は，式(1)，(2)で示される通りである．$x(t)$を入力する時系列データとし，$X(\omega)$はその複素フーリエ成分である．スペクトル$S(\omega)$は，その実数部分をとったものである．なお，出力するスペクトルに関しては日野(1977)による平滑化手法を用い，高周波数側のノイズ除去を行った．

$$x(t) = \int_{-\infty}^{\infty} X(\omega) e^{i\omega t} d\omega \qquad \cdots(1)$$

$$S(\omega) = \lim_{T\to\infty} \frac{2\pi X(\omega) X^*(\omega)}{T} = \lim_{T\to\infty} \frac{2\pi |X(\omega)|^2}{T} \qquad \cdots(2)$$

また，タワー観測から得られた時系列データは，降雨やデータの回収に伴い欠損が生じるため，完全な 1 年間の連続データではない．したがって全データのうち，最も欠損の少ない区間(データ欠損率約 6%)を選択した上で，データが欠損している箇所に関しての補完を行った．更に，それぞれの乱流統計量に関しては，風速について主方向変換と McMillen(1998)に従い傾度補正，気温については Liu ら(2001)を参考に横風，湿度補正を行い，二酸化炭素濃度には密度補正を行った．

4. 結果及び考察

(1)データ欠損部の補完に関して

データ欠損部での補完では，欠損箇所に対して以下の 3 種の方法を試みた．

(a)全体での平均値を代入する．

(b)一日前のデータを利用する．

(c)欠損区間に相当する長さの直前のデータを，連続的に利用する．

ここで，試みたこれらの補完方法によるスペクトル形への影響度を表したものを次の図 1 に示す．各補完方法を用いた場合の主流方向風速のスペクトル解析結果で比較しているが，特に大きな違いは見られないことが分かる．しかし，連続性の確保という点に立ち，(c)の方法による補完手法を他の解析で使用した．

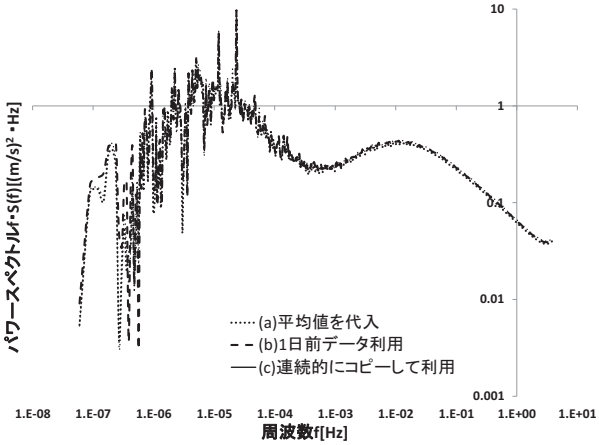

図 1　各補完方法によるスペクトル形への影響

(2)風速変動のパワースペクトル

図 2 は，u,v,w 風速の年間パワースペクトルである．いずれの風速スペクトルにおいても，高周波数側の乱流域にピークを有していることが分かる．このピークの位置は，横軸を無次元化周波数とし，縦軸のスペクトルを u_*の 2 乗で割ることで規格化を行うと，Kaimal の研究結果に基づく普遍形との一致が確認できた．また，この乱流域では Kolmogorov(1941)の次元的な考察，及び後の数々の実験結果により，慣性小領域の存在を示す－2/3 乗則に従う領域の存在が示されたが，この領

域の存在もはっきりと確認できる．つまり，Kolmogorov の理論に従う微細な等方性乱流領域から，1 年周期の低周波領域までを，連続したスペクトル形状によって示すことができたことになる．

加えて，いずれの風速変動においても，明確なスペクトルギャップが 3.0×10^{-4}Hz(約 1 時間)近傍において存在しており，本研究においてその存在が確固たるものとして実証された．更に，周期約 1 日にかけての，スペクトルギャップよりも低周波数域では，再び−2/3 乗則に従う「疑似慣性小領域」というスペクトル形状が確認できる．この結果は，1 日程度のスケールの渦が，1 時間程度のスケールまでカスケードダウンしていることを意味している．この疑似慣性小領域においては，単純なカスケードダウンに従わずに，エネルギーの卓越を示す鋭いスペクトルラインを形成する周期が存在しているが，それが 1 日，半日，1/4 日周期である．この事実より，日周期変動のエネルギー強さが大きく働くことが分かるが，最も卓越する周期は半日となっている．こうした周期の卓越要因には，海陸風等の影響が考えられる．

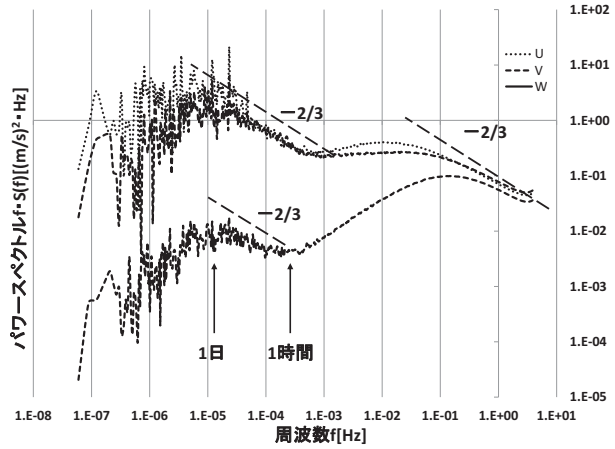

図 2　水平・鉛直方向風速変動パワースペクトル

(3)スカラー変動のパワースペクトル

図 3 は，気温，二酸化炭素濃度，水蒸気濃度の年間変動スペクトルである．気温のスペクトルには，わずかにスペクトルギャップの存在が見受けられるが，二酸化炭素濃度及び水蒸気濃度には明確なスペクトルギャップが見当たらない．これは二酸化炭素，水蒸気などのスカラー変動量は，シアーや浮力等の影響による乱流変動への依存性が小さく，年平均的に見ると一様に存在しているということを意味している．

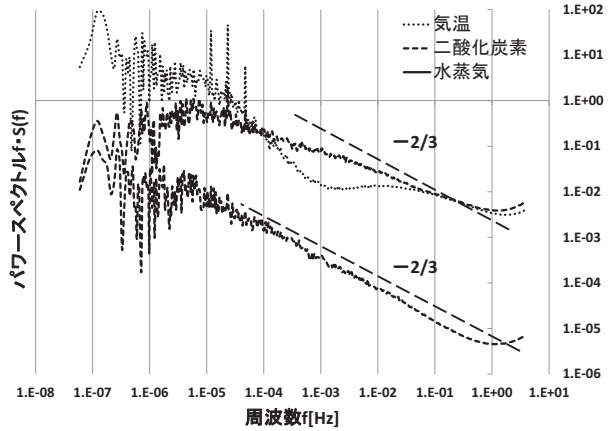

図 3　スカラー変動のパワースペクトル

(4)フラックスのコスペクトル

図 4 は，運動量，顕熱，二酸化炭素，水蒸気フラックスのコスペクトルを，それぞれ年間の共分散値によって規格化したものである．このコスペクトル形においても，乱流域において慣性小領域の存在を示す傾き−4/3 乗に従う領域が存在していることが分かり，また周期約 1 時間近傍における明確なスペクトルギャップの存在も確認できる．コスペクトルにおけるスペクトルギャップは，これまでも約 1 時間程度の周波数帯に存在しているとされ，渦相関法といったフラックス計測の物理的背景として立脚しているが，これを長期間における観測データから示したものは筆者の知る限り存在しない．その原因としては，長期間に渡るスカラー濃度測定が困難で，なおかつこれらの時系列変動をとらえる測定手法が比較的新しいものであるということが挙げられる．なお，本解析でのギャップの存在が示されたことは，フラックスに寄与する渦として，総観的な変動渦までも考慮する必要性が生じ得ることを意味している．

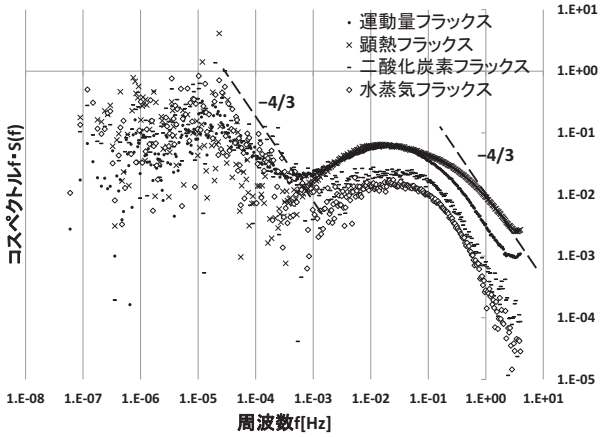

図 4　規格化したフラックスのコスペクトル

5. 結論

高周波数のサンプリング間隔で長期区間の解析を行ったことで，スペクトルギャップ，慣性小領域，疑似慣性小領域の存在を明確に示すことができた．また，都市部においても，乱流場のスペクトル特性は既存の他の接地層から得られた結果と類似したものとなった．更に，スカラー量自体の変動に着目し，二酸化炭素濃度及び水蒸気濃度の長期的な変動特性を見出すことができた．

フラックスのコスペクトルからは，慣性小領域の存在の確認，及び疑似慣性小領域の存在の可能性を示すことができた．

参考文献

J.C.Kaimal(1977) : Horizontal Velocity Spectra in an Unstable Surface Layer

Liu *et al* (2001) : New equations for sonic temperature variance and buoyancy heat flux with an omnidirectional sonic anemometer

日野幹雄(1977)：スペクトル解析

森脇亮ら(2006)：住宅街における冬季夜間の局所的冷気沈降とスカラー濃度プロファイルの形成機構，水工論文集，第 50 巻

チャネルサウンディングへのＩ／Ｑスキューの影響

学籍番号：08B20559　氏名：ファムヴァンフェ　指導教員：高田 潤一, 金ミンソク

1　研究背景

携帯電話に代表される移動通信システムは近年急速に普及し, スマートフォンなどの端末の高速化によって, データのやり取りは音声から, 画像, 動画へと多様化してきている. 将来の移動通信システムでは, さらなる通信速度の高速化が重要な課題となっている. しかしながら良好な伝搬特性から, これまで幅広く用いられてきた 6 GHz 以下の周波数帯は既存の無線通信システムによってほぼ占有されており, さらに通信速度の高速化を実現するためには 6 GHz 以上の高い周波数帯域を活用することが必要と考えられる. また, 複数のアンテナを送受信機で用いて空間的に情報を多重して伝送を行う MIMO (Multi-Input Multi-Output) 伝送の導入も, 周波数資源の確保を併せて必要不可欠である [1].

2　本研究の目的

新たな周波数帯を将来の無線通信システムのために開拓するには、新周波数帯での電波伝搬特性を明らかにすることは不可欠であり, 6GHz 以上の高マイクロ波帯において伝搬路特性を測定, モデル化する必要がある. 本研究では, [2] で開発している測定装置の精度劣化要因となり, ベースバンド回路で生じる IQ スキューをモデル化し, 測定精度への影響を定量的に評価する. さらに解析結果に基づき, 伝搬路測定装置として要求される IQ スキューの精度を明らかにする.

3　IQ スキューによる測定誤差の定式化

3.1　信号モデル

MIMO チャネルサウンダは複数の送受信回路から構成されるが, 本研究では 1 対 1 の送受信系のみを考え, ベースバンド回路の不完全性について議論する. なお, 評価結果は MIMO 装置全体としての影響評価に安易に拡張できる. まず, 図 1 のように受信ベースバンド回路で生じる IQ スキューをモデル化する. 理想的には同相成分 $x_I(t)$ と直行成分 $x_Q(t)$ は 90° 位相が異なるが, ハードウェアの不完全性により誤差 (IQ スキュー) が生じ, 結果としてサウンダの測定精度を劣化させる. 広帯域の伝搬路を測定するためには, 測定帯域内で一様なスペクトルを持つ信号を送信し, 受信側で相関処理を行うことで伝搬路による歪み成分を推定する. ここで, 式 (1) のように N 個の複素正弦波の和で表される広帯域マルチトーン信号を用いる.

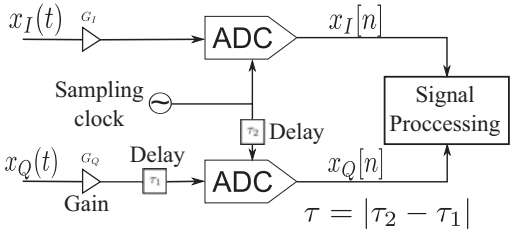

図 1: 受信ベースバンドにおける IQ スキューモデル

$$x(t) = x_I(t) + \mathrm{j}x_Q(t) = \sum_{m=-N/2}^{N/2-1} \Psi_m e^{\mathrm{j}2\pi\Delta_F mt} \quad (1)$$

ただし,$\Psi_m \equiv \Psi_k = e^{\mathrm{j}\phi_k}$,$\phi_k = \dfrac{k^2\pi}{N}(k = 0, 1, \ldots, N-1)$ は Newman 位相 [3],$\Delta_F = 2B/N$,$2B$ は送信周波数帯域幅である. 受信機ではアナログデジタル変換器 (ADC) によってサンプリング間隔 T_s で標本化されたデジタル信号をだーどディスクに保存される. ここでは, 送受信機のベースバンド直結の理想的な構成で,IQ のスキューの影響を評価する. 伝達関数への推定誤差は正規化平均二乗誤差 (NMSE) で定義する.NMSE の解析値は

$$\mathrm{NMSE} = \frac{1}{N}\frac{\sum_{k=0}^{N-1}\left\|\hat{H}_k - H_k\right\|^2}{\sum_{k=0}^{N-1}\|H_k\|^2} \quad (2)$$

ここで,H_k と $\hat{H}_k$ は第 k トーンの IQ スキューがないとある場合の伝達関数である.

$$\mathrm{NMSE} = \frac{2}{N}\sum_{k=0}^{N-1}\left\{\left[1 - \cos\left(2\pi\frac{k\mu_\tau/T_s}{N}\right)\right]\left[\sin\left(\frac{k^2\pi}{N}\right)\right]^2\right\} \quad (3)$$

μ_τ はスキューの平均値である. 式 (3) を用いることで, スキュー影響下での測定誤差の評価が可能となる.

3.2　シミュレーションと結果

IQ スキュー τ が正規分布 $N(\mu_\tau, \sigma_\tau^2)$ に従うと仮定し, シミュレーションにより, 測定誤差を評価した.

図 3a はスキューがないときの理想的なスペクトルで, 図 3b はスキューがあるときで、スペクトルが大きく歪んでいる. 図 3 はシミュレーション (2) と解析値 (3) の NMSE の比較であり, スキューの偏差の影響を示している. 結果からわかるように,$\sigma_\tau < \mu_\tau$ の場合、NMSE はほ

表 1: シミュレーション条件

SNR	50 dB
サンプリング周波数 (F_s)	400 MHz
トーン数 (N)	2048
周波数帯域幅 (B)	400 MHz

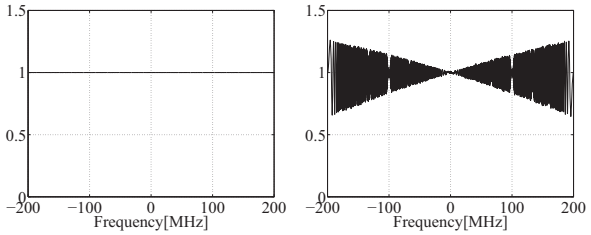

(a) スキューがない場合　(b) $\mu_\tau = 500\,\mathrm{ps}$ と $\sigma_\tau = 10\,\mathrm{ps}$

図 2: 伝達関数の推定結果

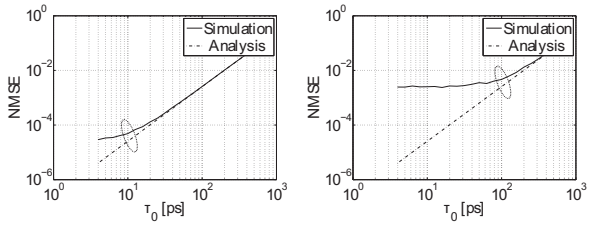

(a) 標準偏差 $\sigma_\tau = 10\,\mathrm{ps}$　(b) 標準偏差 $\sigma_\tau = 100\,\mathrm{ps}$

図 3: NMSE とスキューの関係

ぼ一定の値となる.μ_τ はハードウェアの調整により, ある程度校正することが可能であるが、σ_τ は信号源の性能で決まり調整できない. このことから, スキューの校正に必要とされる精度はスキューの標準偏差と同程度のオーダーであることが判る.

4　システムの評価

4.1　スキューの測定原理

I チャネルと Q チャネルに同じ周波数 f_0 正弦波を入力すると, ハードウェアのの不均一性により出力の信号にスキューが生じる (図 1). スキューによる位相差を求めるために,ADC 出力 $x_I[n], x_Q[n]$ に対して離散ヒルベルト変換 [4] を適用し，複素信号 $z_I[n], z_Q[n]$ を生成する．この複素信号を用いて，次の式でスキューを求める.

$$\tau = \tau_Q - \tau_I = \frac{1}{2\pi f_0}\frac{1}{N}\sum_{n=1}^{N}\arctan\frac{\mathrm{Imag}\left(\frac{z_Q[n]}{z_I[n]}\right)}{\mathrm{Real}\left(\frac{z_Q[n]}{z_I[n]}\right)} \quad (4)$$

ただし,N は入力信号の 1 周期当たりのサンプル数である.

4.2　測定と結果

基準の送信信号は信号発信器 (SG) を使用し, 受信 (Rx) ベースバンドにおける I/Q のスキューを測定した.SG の信号にスキューは無視できると仮定すると, 測定したスキューは Rx の影響であると考えられる送信 (Tx) の I/Q スキューは直接に測定できないため,Tx-Rx 直結によるスキューの測定結果から Tx の I/Q スキューを推定する. Tx と Rx の I/Q スキューはそれぞれ独立に変動すると考えられ，Tx と Rx を接続して測定した I/Q スキューは両者の和で表されるので，その確率分布と Rx の I/Q スキューの確率分布から Tx の I/Q スキューを推定することができる.

表 2: チャネル 1 のスキューの偏差 [ps]

SG-Rx	Tx-Rx	Tx (推定)
5.01	16.5	15.7

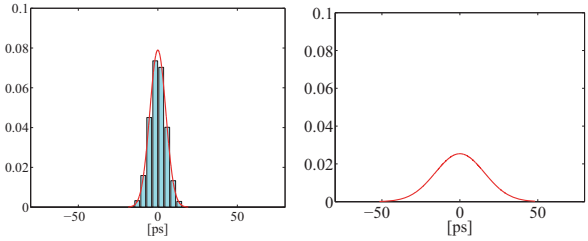

(a) Rx　(b) Tx

図 4: チャネル 1 I/Q スキューの分布

図 4a ように,Rx のスキューのは正規分布とよく一致し,Tx の方が Rx に比べてスキューの変動が大きいことがわかった．これは，Tx と Rx のクロック供給系の回路構成の違いによるものと考えられるが，詳細については今後検討が必要である．また，本システムの IQ スキュー校正におけるしきい値は，平均値で 16.5ps とすればよいことが明らかとなった.

5　結論

本研究では，チャネルサウンダにおける測定精度劣化の要因となる IQ スキューについて検討し，測定誤差をスキューの関数として定式化した．また，実システムで生じるスキューを測定し，ベースバンド回路のスキュー校正におけるしきい値について明らかにした.

参考文献

[1] G. J. Foschini, “Layered space-time architecture for wireless communication in a fading environment when using multiple antennas,” *Bell Labs. Tech. J.*, vol. 1, no. 2, pp. 41–51, 1996.

[2] Takada, Y. Konishi, M. Kim, and M. Ghoraishi, “Development of 11GHz MIMO Channel Sounder with 400MHz Bandwidth using Software Radio Architecture, ” COST 2100 TD(10) 12058, 2010.

[3] S. Boyd, “Multitone signals with low crest factor,” *IEEE Trans. Circuits Syst.*, vol. 33, no. 10, pp. 1018–1022, Oct. 1986.

[4] S. Hahn, *Hilbert Transforms in Signal Processing*. Norwell, MA: Artech House,1996.

INFLUENCE OF CIRCUMFERENTIAL STRAIN OF DISK SURFACE ON PIN-ON-DISK ADHESION CONTACT

Student Number: 08_21493 Name: DOOYOUNG BAEK Supervisor: KUNIO TAKAHASHI

1. Introduction

Applications using the adhesion contact between solids are studied in various fields including joining technology and micro manipulating technology. And, the surface state of elastic body which forms an interface with rigid body is the most important variable in the adhesion phenomenon, because "work of adhesion" (the energy change from surface to the interface per unit area) is used to analyze the adhesion phenomena. In those studies, the influence of deformation of elastic surface on adhesion mechanism is not yet clarified theoretically and experimentally. As practical problems on using adhesion contact for application [3], we discuss the influence of deformation by adding circumferential strain of disk surface on Pin-On-Disk adhesion contact using the JKR theory [1] in this study.

2. Pin-On-Disk adhesion contact model

Fig 1 shows a schematic illustration of the model used in this study based on JKR theory [1].

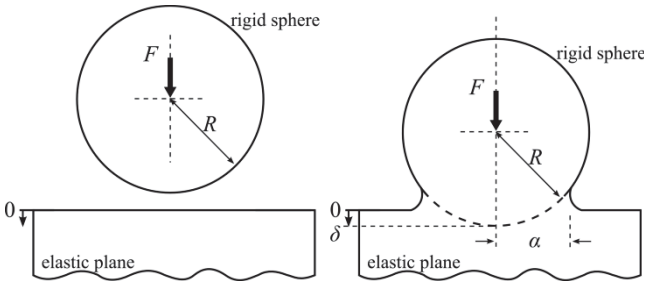

Figure 1 Schematic illustration of JKR theory. ε_r is circumferential strain of disk surface.

The relation between the equilibrium state of total energy E_{total} and the contact radius a can be expressed as

$$E_{\text{total}} = \frac{8}{15}\frac{E}{(1-\nu^2)R^2}a^5 - \frac{2}{3R}\sqrt{\frac{8\pi E\Delta\gamma}{1-\nu^2}}a^{\frac{7}{2}} + \pi a^2\Delta\gamma \qquad (1)$$

where E is Young's modulus, ν is the Poisson ratio, R is sphere's radius, a is radius of contact area, δ is displacement of rigid sphere, F is adhesion force and $\Delta\gamma$ is the energy change from surface to the interface per unit area. The relation between the equilibrium state of displacement δ, force F and contact radius a can also be expressed as

$$\delta = \frac{a^2}{R}\left\{1+\frac{4Ea}{3k(1-\nu^2)}\right\} - \left\{1+\frac{2Ea}{k(1-\nu^2)}\right\}\sqrt{\frac{2\pi(1-\nu^2)\Delta\gamma a}{E}} \qquad (2)$$

$$F = \frac{4E}{3(1-\nu^2)R}a^3 - 2\sqrt{\frac{2\pi E\Delta\gamma}{1-\nu^2}}a^{\frac{3}{2}} \qquad (3)$$

by using the JKR theory [1].

3. Experiment

Experiments to measure the force between the elastic plane and the rigid sphere were carried out by controlling the displacement using experimental system as shown in fig 2. Generator of circumferential strain of disk surface (GCD) was manufactured for this experiment is shown as fig 2(b) and fig 3. A semitransparent silicon rubber sheet of 60×60×10 [mm] and Young's modulus $E = 5.1 \times 10^5$ [Pa] was used as the elastic plane which is set on GCD, and a Plano-convex spherical lens of diameter φ30 [mm] and radius of curvature R=207.6 [mm] was used as the rigid sphere which is set on LFB in fig 2(a). The displacement was applied vertically by stage in fig 2(c), and the radius of contact area during the experiment process was observed using an optical microscope in fig 2(d), and the force was measured by a balance in fig 2(e). The experiment was done in an acrylic box to avoid the effect of dust and moisture, and indoor temperature was fixed at 22°C. First step of experimental procedure is loading the sphere to elastic plane up to 60μm by 1μm step. Second is unloading the sphere by 1μm step to separate from elastic plane. Third is adjusting circumferential strain on disk surface ε_r to 2.5%, 5%, 10% and repeat the experiment from first step. And, wait 30 seconds both on loading and unloading process between 1μm steps.

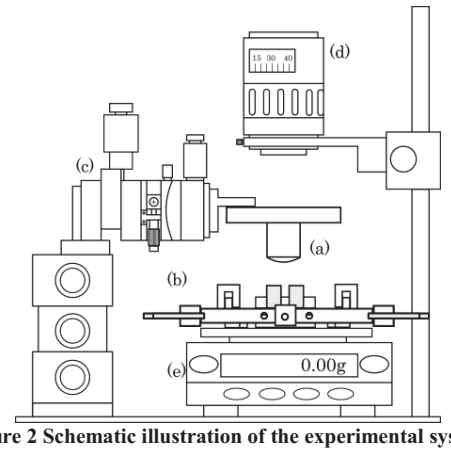

Figure 2 Schematic illustration of the experimental system.

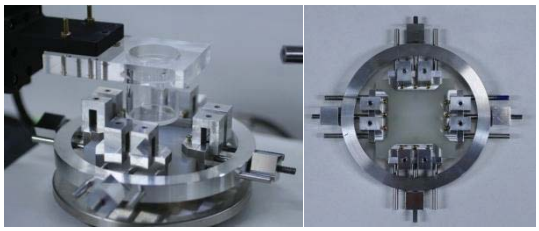

Figure 3 Photographs of Generator of circumferential strain of disk surface(fig 2(b) : GCD)and Lens fixing base(fig 2(a) : LFB).

4. Experimental result and discussion

In the JKR theory, the static condition is assumed. But, discussing the influence on dynamic condition is also needed, because of using elastic adhesion contact on various applications. Therefore, in this study, we carried out the experiment on dynamic condition as the first objective.

As preliminary to discuss the influence of circumferential strain from the experimental result, we need to remove some experimental variables. Experiment result of fig 4 shows dominant trend of occurrence of hysteresis between loading and unloading process is due to the instability caused by the dynamic factor on this experiment. First of all, from change of forces for 30 seconds at each point (a) to (h) in fig 4① and fig 4②, experiment process is carried out before the force be stable. Also, contact radius constant area (c) to (e) in fig 4③ and fig 4④ is observed for the energy gradient in the

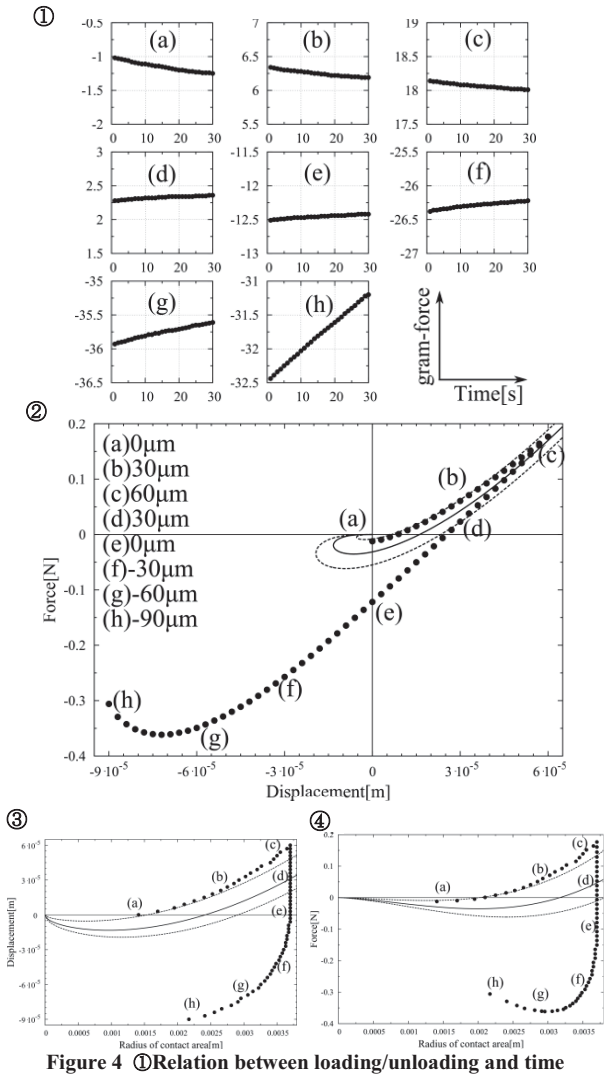

Figure 4 ①Relation between loading/unloading and time dependence of each (a)~(h) point, ②force-displacement, ③displacement-contact area, ④force-contact area.

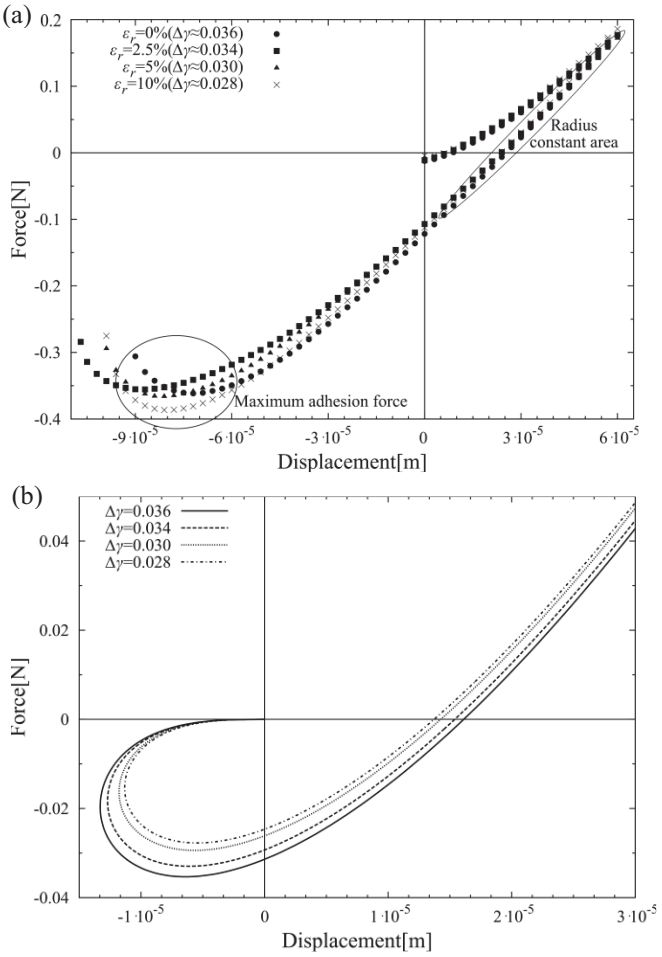

Figure 5 Experimental result of relation between force-displacement when circumferential strain is applied ε_r=0%, 2.5%, 5%, 10% (a), Its theoretical line when Δγ=0.036, 0.034, 0.030, 0.028 (b)

measured values are nearly flat. Therefore, it was considered that the hysteresis is observed commonly in this experiment.

The experimental results of applying circumferential strain on disk surface (ε_r=0%, 2.5%, 5% and 10%) are shown in fig 5(a). We can calculate the parameter work of adhesion which is the important parameter for identify the influence of circumferential strain by energy condition of experimental data and [2]. And work of adhesion is decrease as increasing the circumferential strain of disk surface as shown in legend of fig 5(a), $\Delta\gamma_{0\%} = 0.036$, $\Delta\gamma_{2.5\%} = 0.034$, $\Delta\gamma_{5\%} = 0.030$ and $\Delta\gamma_{10\%} = 0.028$. The relation between force and displacement by using the calculated value of work of adhesion and equation (2), (3) is shown in fig 5(b). As a result of loading process, regularity of decreasing of work of adhesion as increasing the circumferential strain of disk surface is observed in experimental result on fig 5(a). On the other hand, irregularities are observed in unloading process of experimental result on fig 5(a). In addition, maximum adhesion force in unloading process of experimental result is completely irrelevant as shown in fig 5(a). Overall, hysteresis of experimental result is observed in common as analyzed by using circumferential strain on disk surface ε_r=0% of fig 4. And, there is no relationship of maximum adhesion force on fig 5(a) with calculated value of work of adhesion on fig 5(b) completely. But, in the macroscopic point of view, experimental result of fig 5(a) behaves similarly regardless of the circumferential strain on disk surface.

5. Conclusion

The influence of deformation of elastic surface on adhesion mechanism is confirmed by applying circumferential strain on disk surface of pin-on-disk experimentally. There are trend of decreasing of work of adhesion as increasing the circumferential strain. But, unstable conditions of energy both loading and unloading process occurs due to the dynamic elements of the experiment. From perspective of the applications using elastic adhesion contact phenomenon in manipulation, surface strain (or deformation) of elastic body is determined to be almost negligible in dynamic condition, because the effects of surface strain is less than the impact of other factors such as surface washing method, material of elastic body and etc. However, this study needs to be more researched in terms of explain this phenomenon fully by theoretically in static condition.

References

[1] K. L. Johnson, K. Kendall and A. D. Roberts, *Proc. R. Soc. London Ser*. A **324**, 301-313 (1971)
[2] K. L. Johnson, *Tribology Int.* **31**, 413-418 (1998)
[3] Y. Sekiguchi, Tokyo Tech, Dept. I. D. E., Master Thesis (2010)

Optimum Duty Ratio of Boost Switching Regulator for Charging Tiny Electric Energy to Capacitor

Student Number: 08_22021 Name: Yoshito HONDA Supervisor: Kunio TAKAHASHI

1 Introduction

Various kinds of energy sources exist. But some of the sources are hard to be used, because these energy is very small. So, the energy is wasted or unused. In this study, tiny electric energy is defined as electric energy which has too small open circuit voltage or too small short circuit current to use directly. A capacitor is used as a storage devise,since the internal resistance of the capacitor is usually lower than that of rechargeable battery [1]. In order to utilize tiny electric energy, a boost switching regulator is required(Fig.1) to accumulate it [2].

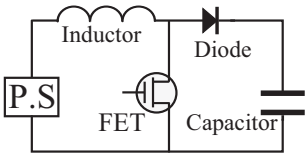

Fig. 1: Boost switching regulator

In this study, the converter is modeled to obtain analytical solution. The optimum duty ratio which maximizes the stored energy into the capacitor per unit time is obtained from the analytical solution of the converter. The relation between the optimum duty ratio and the bounder of the applicable area of the model is discussed.

2 Model of Switching Regulator

In this study, in order to adjust all scale of the energy storage system, a rough model of switching regulator is constructed. The power source is assumed to have the linear I-V characteristics with internal resistance R_{P}. In order to obtain the analytical solution, the inductor is assumed as a resister R_{L} with inductance L, the diode is assumed as a resister R_{D} and the FET is assumed as a switch with resistance R_{S}, respectively. R_1 and R_2 are given by $R_1 = R_{\mathrm{P}} + R_{\mathrm{L}} + R_{\mathrm{S}}$ and $R_2 = R_{\mathrm{P}} + R_{\mathrm{L}} + R_{\mathrm{D}}$. V_{in} is the open circuit voltage of the power source. For the purpose of the accumulation and the utilization of the tiny energy, capacitance is needed to be enough large. So, the capacitor can be assumed as buttery with a constant voltage V_{out}. Because the energy efficiency is not considered in this study, the energy loss of the FET is not taken into the calculation. Then, the model is shown in Fig.2.

During the switch is on 1, the current increases and the energy is stored in the inductor and the current of this time is i_1. During the switch is on 2, the energy is released to accumulate in the capacitor and the current of this time is i_2. T_1 and T_2 are the switching period on 1 and 2, respectively, and the switching cycle T is given by $T_1 + T_2 = T$. The duty ratio of the switching regulator is defined as $\tilde{d} = T_2/T$. The gain is defined as $\tilde{g} = V_{\mathrm{out}}/V_{\mathrm{in}}$. $\tilde{r} = R_2/R_1$ is the normalized resistance. $\tilde{T} = R_1 T/L$ is the normalized switching duty ratio.

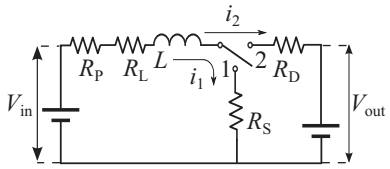

Fig. 2: Equivalent Circuit

Considering the boosting process, the voltage of the capacitor increases very slowly. So, the shape of the current approaches to a saturated shape as shown in Fig.3. The current can be expressed as

$$i_1 = \frac{V_{\mathrm{in}}}{R_1} \frac{\left(\frac{1-\tilde{g}}{\tilde{r}} - 1\right)\left(1 - e^{\beta}\right)}{1 - e^{\alpha+\beta}} e^{-\frac{R_1}{L}t} + \frac{V_{\mathrm{in}}}{R_1}, \qquad (1)$$

$$i_2 = \frac{V_{\mathrm{in}}}{R_1} \frac{\left(\frac{1-\tilde{g}}{\tilde{r}} - 1\right)\left(1 - e^{\alpha}\right)}{e^{-\tilde{r}\tilde{T}+\alpha} - e^{\tilde{r}\alpha}} e^{-\frac{R_2}{L}t} + \frac{V_{\mathrm{in}} - V_{\mathrm{out}}}{R_2}, \qquad (2)$$

when $\alpha = -\left(1 - \tilde{d}\right)\tilde{T}$ and $\beta = -\tilde{r}\tilde{d}\tilde{T}$.

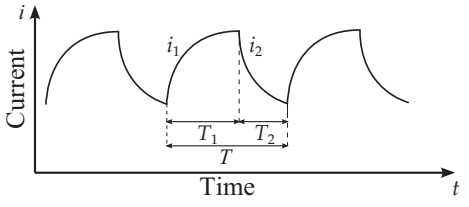

Fig. 3: Switching Cycle and Current

The characteristics such as V_{in} and the circuit parameters such as L, R, etc... cannot be changed in the operation. V_{out} increases with increasing charge in the capacitor during the operation. Therefore, the gain is a given parameter. The control parameter should be controlled to obtain the efficient accumulation of the tiny electric energy. Because the Switching period should be defined considering energy loss of the FET and resisters, the switching cycle cannot be optimize in this study. So, only the duty ratio is the controllable parameter.

3 Optimum Duty Ratio

The charge accumulated in the capacitor is

$$q = \int_{T_1}^{T} i_2 dt \tag{3}$$

The optimum duty ratio can be obtained by maximizing,

$$\frac{q}{T} = \frac{V_{\text{in}}}{R_2}\left\{\frac{1}{\tilde{T}}\frac{\left(1-e^{-\left(1-\tilde{d}\right)\tilde{T}}\right)\left(1-e^{-\tilde{r}\tilde{d}\tilde{T}}\right)}{1-e^{-\left(1-\tilde{d}+\tilde{r}\tilde{d}\right)\tilde{T}}}\left(1+\frac{\tilde{g}-1}{\tilde{r}}\right)-\left(\tilde{g}-1\right)\tilde{d}\right\} \tag{4}$$

The optimum duty ratio $\tilde{d}$ should be chosen so that

$$\frac{\partial \frac{q}{T}}{\partial \tilde{d}} = 0 \tag{5}$$

is satisfied. Eq.5 leads to

$$\tilde{g} = 1 + \frac{\tilde{r}\frac{-e^{\alpha}+\tilde{r}e^{\beta}+2(1-\tilde{r})e^{\alpha+\beta}+\tilde{r}e^{2\alpha+\beta}-e^{\alpha+2\beta}}{(1-e^{\alpha+\beta})^2}}{\tilde{r}-\frac{-e^{\alpha}+\tilde{r}e^{\beta}+2(1-\tilde{r})e^{\alpha+\beta}+\tilde{r}e^{2\alpha+\beta}-e^{\alpha+2\beta}}{(1-e^{\alpha+\beta})^2}}, \tag{6}$$

Eq.5 is only a necessary condition of the optimum duty ratio. In order to verify whether condition of Eq.6 is maximizing condition or minimizing condition, the sign of $\partial^2\left(\frac{q}{T}\right)/\partial\tilde{d}^2$ should be verified. Since $\partial^2\left(\frac{q}{T}\right)/\partial\tilde{d}^2$ is always negative when

$$\tilde{g} > 1 - \tilde{r} \tag{7}$$

is satisfied. The gain obtained by Eq.6 is always satisfied Eq.7. So, Eq.6 shows the most efficient duty ratio as a function of the switching period, the circuit parameters and the gain. Eq.6 is plotted in Fig.4. Fig.4 shows the relation between gain and optimum duty ratio. The gain $\tilde{g}$ increases with increasing the voltage of the capacitor. When the gain is less than $\frac{1}{1+\tilde{r}}$, capacitor should be connected the power source. When the gain is larger than $\frac{1}{1+\tilde{r}}$, the switching regulator is started to operation and the duty ratio is chosen according to the voltage of the capacitor.

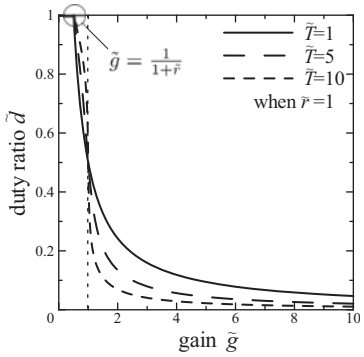

Fig. 4: The Optimum Duty Ratio of Equivalent Circuit

4 Comparing the Conditions

In the equivalent circuit, the diode is assumed to be a resister. The reverse current might flow to the inductor when the voltage of the capacitor grows. The existence of the reverse current makes a failure of the equivalent circuit because the reverse current cannot flow to the inductor. The boundary condition which the reverse current does not flow to inductor is

$$i_1(0) = i_2(T) > 0. \tag{8}$$

From Eq.8, the boundary condition is obtained as

$$\tilde{g} < \frac{\tilde{r}e^{\beta}\left(1-e^{\alpha}\right)}{1-e^{\beta}} + 1. \tag{9}$$

From Eq.9, the applicable area of the model in which the reverse current does not flow is shown in Fig.5.

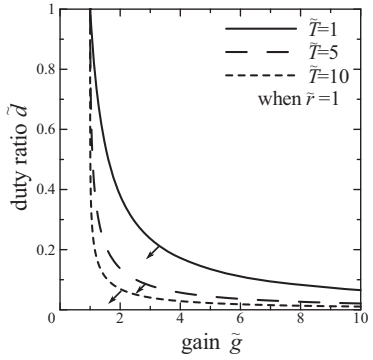

Fig. 5: Boundary Condition of approximation

In order to operate the FET without the failure of the equivalent circuit, the optimum condition is needed to satisfy Eq.9. The optimum condition is compared with the boundary condition of the model in order to verify the relation between both conditions. Then it is made clear that the optimum condition always satisfies the boundary condition.

5 Conclusion

The optimum condition of the duty ratio and the bounder of the applicable area of the model are obtained as functions of the switching period and the circuit parameters. Comparing both conditions, the optimum duty ratio always satisfies the applicable area of the model. The optimum duty ratio without the failure of the equivalent circuit is obtained.

References

[1] G. Walden, J. Stepan and C. Mikolajczak, 2011, "Safety Considerations when Designing Portable Electronics with Electric Double-Layer Capacitors (Supercapacitors)", IEEE Symp. Product compliance Engineering, 1-5.

[2] Otome Keisuke, Effects of conditions of use on the energy efficiency of boost switching regulator, master thesis, (2010)

Wideband IQ Imbalance Compensation Technique using Spectrum Analyzer

Student Number:08B23061 Name:Yuta Maruichi Supervisor: Jun-ichi Takada, Minseok Kim

1 Introduction

New communication systems are constantly being developed, as demand for various new wireless applications continues to increase rapidly. Thus, super high bit-rate mobile systems are strongly desired. However, considering the recent explosion of mobile Internet usage and congestion of conventional frequency spectrum (below 3 GHz), it will be necessary to explore new frequency spectrum which can accommodate systems with wider bandwidth than current ones. MIMO (multiple-input multiple-output) technology has been considered to realize the required performance by increasing spectrum efficiency.

When MIMO systems using higher frequencies and wideband signals are utilized, it is necessary to evaluate the channel capacity. For this purpose, implementation of a MIMO channel sounder is in progress [1]. To measure the channel response correctly using the channel sounder, system calibration is very important. This research focuses on IQ imbalance compensation for quadrature modulator in the RF circuit.

2 Narrowband IQ Imbalance Compensation Method

A slight discrepancy in the quadrature modulator causes an imbalance between the in-phase and quadrature components, named IQ imbalance. It should be sufficiently compensated because it causes image (mirror frequency) distortion and generates carrier leakage. By now, lots of compensation methods for IQ imbalance have been intensively studied.

Assuming that the frequency characteristic of each circuit component is negligible, the IQ imbalance in quadrature modulator can be simply modeled as Fig. 1, where ε denotes the amplitude difference, θ denotes the phase offset or quadrature skew of the quadrature oscillator branches, and Δ_{I} and Δ_{Q} denote the DC offset components for I and Q branches respectively [3]. A simpler method using only spectrum measurement with a spectrum analyzer to get the amplitude of signal is used, because it is a handy and efficient method providing sufficient accuracy.

From the model, distorted output signal can be written as

$$\begin{aligned} \tilde{z}(t) &= (\mathbf{E}\mathbf{w}(t))^T(\mathbf{x}(t)+\boldsymbol{\Delta}) \\ &= z(t)+z_{\mathrm{ei}}(t)+z_{\mathrm{ec}}(t), \end{aligned} \tag{1}$$

where $z(t)$, $z_{\mathrm{ei}}(t)$, $z_{\mathrm{ec}}(t)$ denote ideal output, image distortion, carrier leakage respectively, and $\mathbf{E}$ denote error matrix of ε and θ, $\mathbf{w}(t)$ denote the career wave, $\mathbf{x}(t)$ denote baseband wave, and $\boldsymbol{\Delta}$ denote DC offset. In the equation (1), if the Baseband wave have already distorted as

$$\mathbf{x}'(t) = (\mathbf{E}^{-T}\mathbf{x}(t) - \boldsymbol{\Delta}, \tag{2}$$

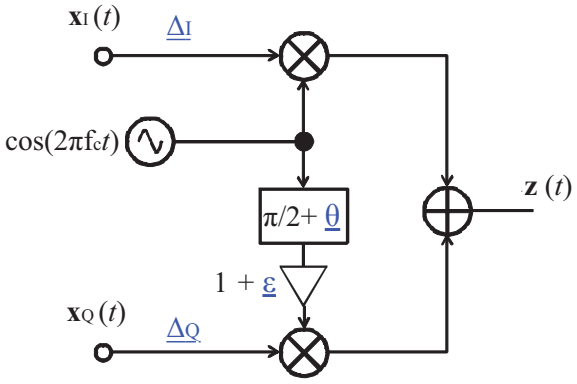

Figure 1: IQ imbalance model of quadrature modulator.

the output signal can be ideally generated. That shows if the model parameters can be estimated properly, the IQ imbalance can be easily eliminated using digital pre-distortion on the original transmit signals. By using the spectrum analyzer, the power spectrum of image distortion and carrier leakage can be obtained. From the information of amplitude of each component, it is possible to estimate the error parameters using the algorithm which is proposed in [2].

Then, the output signal can be ideally generated. In this thesis, the model parameter is optimized to suppress the following values

$$L_{\mathrm{IRR}} = \frac{E[\mathbf{z}_{\mathrm{ei}}(t)]}{E[\mathbf{z}(t)]} = \frac{(\varepsilon^2+2\varepsilon+2)-2(1+\varepsilon)\cos\theta}{4}, \tag{3}$$

which denotes the image power reduction ratio (IRR) , and

$$L_{\mathrm{CRR}} = \frac{E[\mathbf{z}_{\mathrm{ec}}(t)]}{E[\mathbf{z}(t)]} = \frac{\Delta_{\mathrm{I}}^2+\Delta_{\mathrm{Q}}^2}{A_x^2}, \tag{4}$$

which denotes the carrier leakage power reduction ratio (CRR) after ε and θ are compensated. A_x is the amplitude of the input signal.

NMSE (Normalized Mean Square Value) is used to estimate the effect of IQ imbalance. From the equaltions above, it can be derived that NMSE corresponds to L_{IRR}.

3 Wideband IQ Imbalance Compensation Method

By using the method above, the IQ imbalance can be compensated for any specific frequency, but it is valid only for a narrowband system. If it is used in a wideband system, the whole band can not be compensated properly. Fig.2 shows the result of narrowband compensation for wideband signal (-200MHz to 0MHz) that has been compensated at f_0 =6.25MHz. It can be seen as from the figure that the IRR level increases as frequency is further away from 6.25MHz.

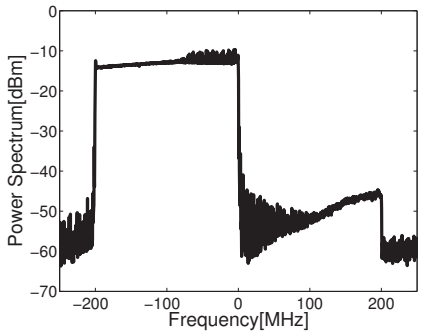

Figure 2: Wideband signal after narrowband compensation (f_0 = 6.25MHz)

It is because ε and θ that has been estimated at any specific frequency may not be the optimum value at different frequencies. Thus, it is necessary to alter this simple narrowband model into wideband model to perform compensation over multiple frequencies.

To compensate all frequencies and totally decrease the IRR level, ε and θ can be regarded as $\varepsilon(f)$ and $\theta(f)$, so error matrix $\mathbf{E}$ also becomes $\mathbf{E}(f)$. In (2), the variable is time and the signal is compensated in the time domain, but the variable of the parameters here are frequency, so it is necessary to use Fourier transform and compensate in the frequency domain. Thus, distorted signal in the frequency domain can be written as

$$\mathbf{X}'(f) = \{\mathbf{E}(f)^T\}^{-1}\mathbf{X}(f), \tag{5}$$

and the distorted signal becomes

$$\mathbf{x}'(t) = \mathcal{F}^{-1}[\mathbf{X}'(f)] - \mathbf{\Delta}, \tag{6}$$

where $\mathcal{F}^{-1}$ denotes the operator of inverse Fourier transform.

Error matrix is measured at center frequency of each subband individually by dividing the target frequency band into several number of sub-bands. For narrowband testing, the IRR level can be decreased as shown in Fig.3. Fig.4 shows one of the results of wideband testing using wideband compensation method. It is concluded that the wideband IQ imbalance can be compensated by using the proposed method.

Finally, narrowband testing and wideband testing are compared in Fig.5. In wideband testing, it includes the effect of intermodulation, so the NMSE of wideband testing is worse than narrowband testing.

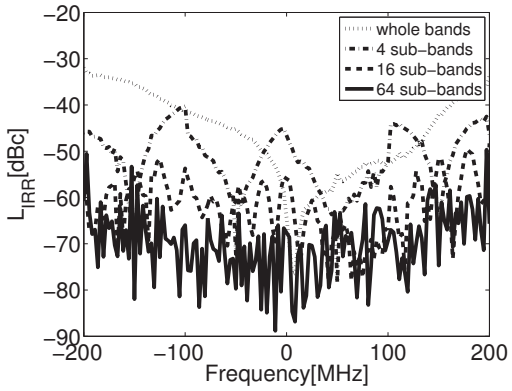

Figure 3: L_{IRR} vs. Frequency

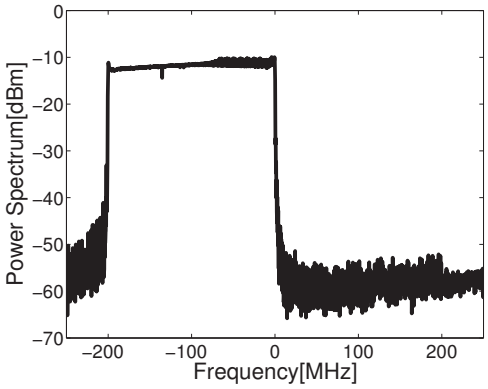

Figure 4: Wideband signal after wideband compensation (number of sub-bands, $N = 16$).

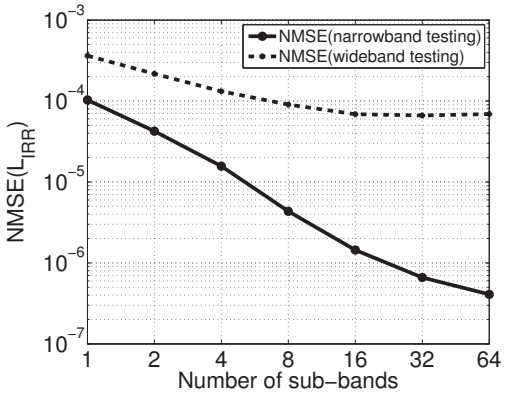

Figure 5: NMSE vs. Number of sub-bands

4 Conclusion

This thesis proposed an automatic wideband IQ imbalance compensation technique for quadrature modulator using spectrum measurement with a spectrum analyzer. The method is efficient to reduce the effect of frequency characteristics which occur in wideband systems by dividing whole band into several sub-bands and compensating at each sub-band .

Acknowledgment

This work was partly supported by "The research and development project for expansion of radio spectrum resources" of The Ministry of Internal Affairs and Communications, Japan.

References

[1] Y. Konishi, M. Kim, M. Ghoraishi, J. Takada, S. Suyama and H. Suzuki, "Channel Sounding Technique using MIMO Software Radio Architecture," Proc. *European Conference on Antennas and Propagation (EuCAP)*, Apr. 2011.

[2] M. Kim, Y. Konishi, J. Takada, B. Gao, "IQ Imbalance Compensation Technique for Quadrature Modulator by Single-Tone Testing," submitted to *IEICE Trans. Commun.*

[3] D. Tandur and M. Moonen, "Joint Compensation of OFDM Frequency-Selective Transmitter and Receiver IQ Imbalance", *EURASIP J. Wirel. Commun. Netw.* (2007.)

Synthesis of zeolites from lake sludge for heavy metal removal

Student No. 08B26852 Name : Liu Xuebin Supervisor: Hirofumi HINODE
Chris SALIM

1. Introduction

Lakes are important as sources of fresh water. However, contaminants can easily accumulate in lake due to closed system. The eutrophication of lake is often caused by human activities such as heavy use of fertilizers near the lake or the increase of wastewater discharged from households and factories. The lake in this condition typically has poor clarity and is subject to devastating algal blooms which will result in the decrease of dissolved oxygen and the increase of lake sludge. Usually, lake sludge is dredged from lake in order to keep the water quality. The dredged lake sludge is then disposed to landfill sites, but it causes the high cost problem. Previous studies showed that lake sludge that contains silica and alumina can be converted into zeolites using hydrothermal treatment[1] in NaOH medium. These zeolites are useful for heavy metal removal from wastewater.

In this study, the hydrothermal synthesis of zeolite from lake sludge at various reaction temperature and different NaOH concentration was tried. The performances of the synthesized zeolite were evaluated.

2. Experimental

2.1 Zeolite synthesis

Lake sludge from Kasumigaura was dried at 105℃ for 24 h and sieved. The dried sludge was mixed with sodium hydroxide solution (NaOH) and was shaken for 24 h in a 23 ml teflon reaction vessel. The vessel was then put inside autoclave and incubated at specific temperature of 90 to 150℃ in the oven. After the reaction, the solid phase was washed with deionized water until pH was closed to 7 and air dried.

2.2 Characterization

XRD analysis was carried out to identify the crystal phase. The cation-exchange capacity (CEC) was determined by sodium acetate method[2] with the following procedure. The sample was saturated with NaOAc solution, and then the Na^+ was extracted by NH_4OAc solution. The amounts of released Na^+ were measured using Inductively Coupled Plasma-Atomic Emission Spectrometry (ICP-AES) equipment. The synthesized zeolites were evaluated on their adsorption capacity of heavy metal (Cu^{2+}) in aqueous solutions. The specific surface structure was observed by scanning electron microscopy (SEM).

3 Results and discussio

3.1 XRD analysis

Temperature is an important factor affecting the formation of zeolite. Figure 1 shows the formation of zeolite NaP1 was observed at temperature of 90 to 150 ℃ . The zeolite Analcime-C was formed at temperature of 120 to 150℃.

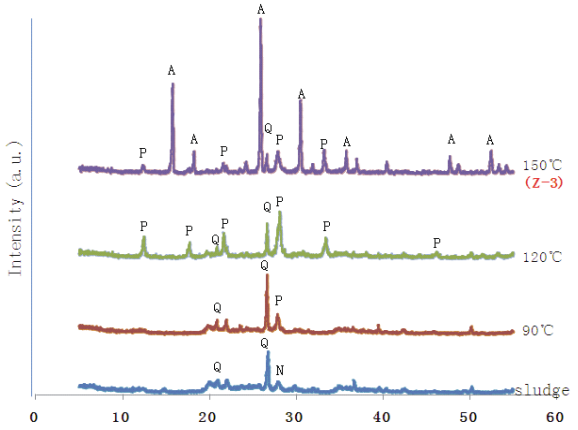

Figure 1.XRD pattern of the products obtained from various reaction temperature (1M, L/S=5ml/g, 24h)

The results from XRD analysis of obtained products with various NaOH concentrations are shown in Figure 2. With NaOH concentration

of 1M, the zeolite NaP1 was formed and quartz was also present. From 1.5 M to 2 M, it arreared that not only Nap1,the zeolite Analcime-C phase was also formed. It is possible the zeolite type changes due to the Si/Al ratio in the liquid phase. At NaOH concentration of 3 M, zeolite NaP1 and Analcime-C almost disappared due to the formation of Unnamed zeolite

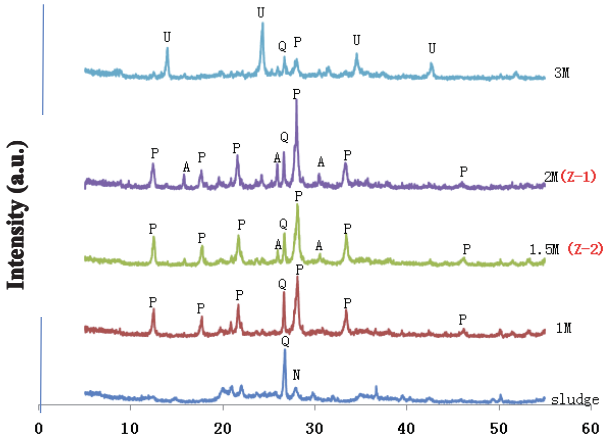

Figure 2.XRD pattern of zeolites produced under various NaOH concentrations (120℃,24 h)

Q:Quartz (SiO_2)
U: Unnamedzeolite ($Na_6(AlSiO_4)_6 \cdot 4H_2O$)
P: Zeolite NaP1 ($Na_6Al_6Si_{10}O_{32} \cdot 12H_2O$)
A:Analcime-C ($Na(AlSi_2)O_6 \cdot H_2O$)
N: Albite ($NaAlSi_3O_8$)

3.2 The Cation-Exchange Capacity (CEC)

Figure 3 shows the CEC values of products under different NaOH concentrations. Zeolite produced under NaOH concentration of 1.5 M showed the highest CEC value. Based on the XRD results, zeolite NaP1 exhibited higher CEC, compared to zeolite Analcime-C and Unnamed zeolite.

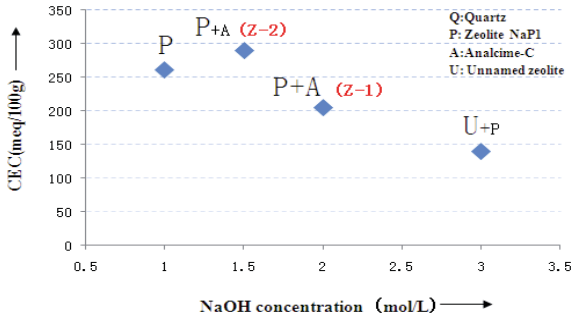

Figure 3.CEC of the products obtained from various NaOH concentrations(120℃,24h)

Figure 3 shows the CEC values of products under different reaction temperation. Zeolite produced under 120 ℃ showed the highest CEC value. Based on the XRD results, zeolite NaP1 exhibited higher CEC, compared to zeolite Analcime-C and quartz.

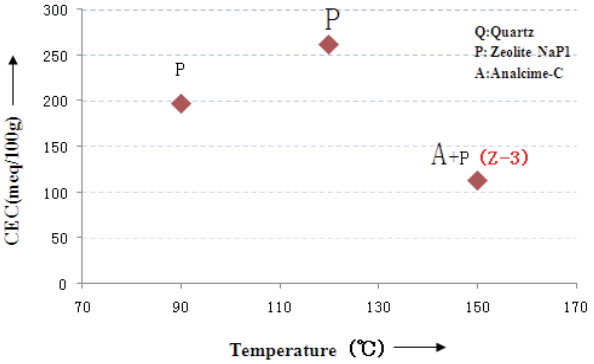

Figure 4.CEC of the products obtained from various reaction temperature (1M, L/S=5ml/g, 24h)

3.3 Heavy metal adsorption

Table 1 shows the saturated adsorption capacity (X_m) of Cu^{2+} for various synthesized zeolite. These results indicated that the synthesized zeolites have adsorption capacity toward Cu^{2+}, and NaP1 has a higher adsorption capacity towards Cu^{2+} than zeolite Analcime-C.

Zeolite product	Major phase	CEC(meq/100g)	Xm (Cu2+(mg/g))
Z-1	NaP1	204.4	35.7
Z-2	NaP1	289.1	58.8
Z-3	Analcime-C	113.1	19.6

Table 1.CEC and adsroption capacity of Cu^{2+} for synthesized zeolite

4.Conclusions

Lake sludge (Si/Al=1.9) was successfully converted into zeolites. Zeolite NaP1 was formed at 1~2M of NaOH solution and at 90~120℃. Analcime-C was identified at 1~2 M of NaOH solution and at 120~150 ℃. Zeollite NaP1 has a higher CEC and a higher adsorption capacity of Cu^{2+} than Analcime-C.

Reference

[1]W.Qu. Master's thesis, Tokyo Institute of technology(2006)

[2]United State Enviromental Protection Agency, http://www.epa.gov/

Temperature Distribution Change by Point Contact Current

Student Number: 08B26958 Name: Kazuki WAKABAYASHI Supervisor: Kunio TAKAHASHI

1 Introduction

In industrial world, the Joule heat generation is used to join materials, such as resistance welding technology, but it can damage the contact point of electro devices, such as relays in high-frequency application.

A bunch of researches are carried out to understand the heat generation[1]~[6]. In the electro devices investigation, researches are carried out to investigate temperature distribution of the devices for preventing melting[2] [3]. In the welding technology, researches are carried out to investigate the melting condition [4] [5]. For those, temperature distribution change is important to estimate if material melts because it is possible to estimate if material melts to compare the temperature with the malting temperature of a material.

In order to get temperature distribution change, numerical analyses using FEM(Finite Element Method) are carried out to obtain the temperature distribution change inside a material[6] under the point contact of two materials. However, the treatment of a singular point is unclear. Around a singular point, the energy is concentrated and it has large affection to temperature. Furthermore, the result can not be applied to the system in which different material is used or different scale is settled. Then, the temperature distribution change which is available for various systems is needed. In this research, we focus on obtaining an analytical solution of temperature distribution change which is useful for estimation of the melting condition.

2 Derivation of theoretical equation of temperature distribution change by point contact current

2.1 Semi-infinite solid model

A semi-infinite solid system to which current flows from a point is considered as a model. The heat which occurs at $\boldsymbol{r}_1$ propagates to $\boldsymbol{r}$ by heat diffusion and reflection at surface.

In the calculation, an infinite solid system to which current $2I$[A] is applied is introduced because the sum of heat increase at $\boldsymbol{r}$ in the infinite system is equivalence to that in the semi-infinite system to which current I[A] is applied.

Heat loss from surface to atmosphere is assumed negligible because the loss is generally small compared with temperature increase by heat propagations in the solid. Since phase transformation is not considered, latent heat is assumed negligible. Even though materials are not homogeneous because of surface oxidation and others, material constants(specific heat, density, resistivity, thermal diffusivity) are assumed homogeneous to investigate a simple system, and not to change during the heat generation.

2.2 Heat equation

Heat equation is

$$\frac{\partial T(x,y,z,t)}{\partial t} = D\Delta\ T(x,y,z,t) \tag{1}$$

where Δ is Laplace operator. When a quantity of heat $d\delta q(\boldsymbol{r}_1)$ [J] is deposited instantaneously at $\boldsymbol{r}_1$ at $t=\tau$, the solution at $\boldsymbol{r}$ at $t\ (>\tau)$ is given as (2).

$$d\delta T(\boldsymbol{r},\boldsymbol{r}_1,t,\tau) = \frac{d\delta q(\boldsymbol{r}_1)}{C\rho_d}\frac{1}{(4\pi D(t-\tau))^{3/2}}\exp\left(-\frac{(\boldsymbol{r}_1-\boldsymbol{r})^2}{4D(t-\tau)}\right) \tag{2}$$

The energy source of this system is current. The current density distribution of the system to which current $2I$[A] is applied to origin is expressed as $i(\boldsymbol{r}_1) = 2I/4\pi|\boldsymbol{r}_1|^2 = I/2\pi|\boldsymbol{r}_1|^2$. Therefore, instantaneous heat input $d\delta q(\boldsymbol{r}_1)$[J m^{-3}] at $\boldsymbol{r}_1$ is given as follows,

$$d\delta q(\boldsymbol{r}_1) = \rho\left(\frac{I}{2\pi|\boldsymbol{r}_1|^2}\right)^2\delta t dv \tag{3}$$

where ρ[Ω m] is resistivity, δt is differential time, dv is differential volume. Temperature distribution change is obtained by substituting Eq. (3) for Eq. (2) and integrating it for space $r_1 \geq 0$ and for time $t \leq t_{\rm heat}$. However the result diverges due to the singular point of heat input at the origin.

2.3 An approximation for removal of the singular point

In this system, current density distribution $i(\boldsymbol{r}_1)$ is proportional to $\frac{1}{{r_1}^2}$, so it diverges at the origin. In fact, there is an area at the contact between electrode and solid and current density has finite values. Therefore, this model is not appropriate as a model of the heat generation.

An contact area a is defined as shown in Fig. 2. In the outside of semi-sphere whose radius is a, the current density is proportional to $\frac{1}{{r_1}^2}$ since it is not affected by the existence of the contact area. Inside of the semi-sphere, current density seems to have complex distribution. Even though, it is reported that the current density has distribution which has peak at $r=a$ [6], in this research, the purpose is to roughly estimate the melting condition. Therefore, a simple approximation that current density inside $r \leq a$ is constant is introduced. The constant value is set to obtain a upper/lower limit of temperature and the limits is compared with melting point for estimation of melting. Fig. 1 shows two ways of approximations:

In order to obtain the lower limit, an approximation(1) current density distribution inside $r \leq a$ is the value of current density at $r=a$, is introduced. In this approximation, less energy amount is considered than input energy so that it provides us a lower limit

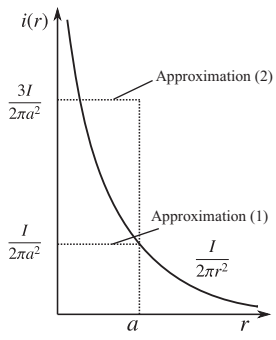

Fig.1 An approximation of current distribution in $r \leq a$

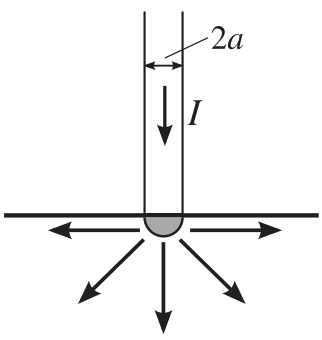

Fig.2 Current distribution with contact area

of temperature. In order to obtain the higher limit, an approximation(2) current density distribution inside $r \leq a$ is the value of the average of current density in $0 \sim a$ is introduced. The average of current density $i_{ave}(a)$ is $\frac{3I}{2\pi a^2}$, the value of current density at $r = a$ is $\frac{I}{2\pi a^2}$. The approximation(1) has same energy as input energy so that it provides us the rough upper limit of temperature. By those approximations, we can obtain the rough range of temperature.

2.4 Nondimensionalization of $T(r,t)$

Nondimensionalization is carried out as follows: $\tilde{t} = t/t_{\rm heat}$, $\tilde{\tau} = \tau/t_{\rm heat}$, $\tilde{r} = r/a$, $\tilde{r_1} = r_1/a$ and $\tilde{D} = \frac{4D}{a^2/t_{\rm heat}}$. In addition to those, T is nondimensionalized as

$$\tilde{T}(\tilde{r},\tilde{t}) = \frac{T(\tilde{r},\tilde{t},a,t_{\rm heat}) - T_0}{2\frac{\rho}{C\rho_d}\left(\frac{I}{2\pi}\right)^2\left(\frac{t_{\rm heat}}{4\pi D}\right)^{\frac{1}{2}}\frac{1}{a^3}} \tag{4}$$

Normalized temperature distribution is finally obtained as follows. In the case of period of heat input ($\tilde{t} \leq 1$),

$$\tilde{T}(\tilde{r},\tilde{t}) = \frac{1}{2\tilde{r}}\int_{\tilde{\tau}=0}^{\tilde{\tau}=\tilde{t}} \frac{1}{(\tilde{t}-\tilde{\tau})^{1/2}} \left[\begin{array}{l} +c^2\int_{\tilde{r}_1=0}^{\tilde{r}_1=1}\tilde{r}_1\left\{\exp\left(-\frac{1}{\tilde{D}}\frac{(\tilde{r}_1-\tilde{r})^2}{\tilde{t}-\tilde{\tau}}\right)-\exp\left(-\frac{1}{\tilde{D}}\frac{(\tilde{r}_1+\tilde{r})^2}{\tilde{t}-\tilde{\tau}}\right)\right\}d\tilde{r}_1 \\ +\int_{\tilde{r}_1=1}^{\tilde{r}_1=\infty}\frac{1}{\tilde{r}_1^3}\left\{\exp\left(-\frac{1}{\tilde{D}}\frac{(\tilde{r}_1-\tilde{r})^2}{\tilde{t}-\tilde{\tau}}\right)-\exp\left(-\frac{1}{\tilde{D}}\frac{(\tilde{r}_1+\tilde{r})^2}{\tilde{t}-\tilde{\tau}}\right)\right\}d\tilde{r}_1 \end{array} \right] d\tilde{\tau} \tag{5}$$

In the case of period after heat input finishes ($\tilde{t} > 1$),

$$\tilde{T}(\tilde{r},\tilde{t}) = \frac{1}{2\tilde{r}}\int_{\tilde{\tau}=0}^{\tilde{\tau}=1} \frac{1}{(\tilde{t}-\tilde{\tau})^{1/2}} \left[\begin{array}{l} +c^2\int_{\tilde{r}_1=0}^{\tilde{r}_1=1}\tilde{r}_1\left\{\exp\left(-\frac{1}{\tilde{D}}\frac{(\tilde{r}_1-\tilde{r})^2}{\tilde{t}-\tilde{\tau}}\right)-\exp\left(-\frac{1}{\tilde{D}}\frac{(\tilde{r}_1+\tilde{r})^2}{\tilde{t}-\tilde{\tau}}\right)\right\}d\tilde{r}_1 \\ +\int_{\tilde{r}_1=1}^{\tilde{r}_1=\infty}\frac{1}{\tilde{r}_1^3}\left\{\exp\left(-\frac{1}{\tilde{D}}\frac{(\tilde{r}_1-\tilde{r})^2}{\tilde{t}-\tilde{\tau}}\right)-\exp\left(-\frac{1}{\tilde{D}}\frac{(\tilde{r}_1+\tilde{r})^2}{\tilde{t}-\tilde{\tau}}\right)\right\}d\tilde{r}_1 \end{array} \right] d\tilde{\tau} \tag{6}$$

3 Result of theoretical analysis

3.1 Temperature Distribution Change

Fig. 3,6 shows the result of Eq. 5,6 with approximation(1)(2) where $\tilde{D} = \frac{4D}{a^2/t_{\rm heat}} = 100$. Note that $\tilde{D}$ is defined by thermal diffusivity D, contact area a, heat input time $t_{\rm heat}$.

Fig. 3,5 shows the temperature change with time. Temperature is monotonically increasing with time in the period of heat input. When heat input finishes ($\tilde{t} = 1$), temperature changes as differential coefficient is noncontinuous. This is because heat input suddenly disappears. Temperature goes back to initial temperature with sufficient passage of time.

Fig. 4,6 shows temperature distribution. The temperature is highest at origin and is monotonically decreasing with distance from origin.

4 Conclusion

A theoretical equation of temperature distribution change is obtained for investigating heat generation phenomena by point contact current with considering the model that semi-infinite solid to which current is applied and with introducing an approximation that current distribution is constant inside $r \leq a$, under the assumptions that material constants are constant and latent heat and radiant heat are negligible. Given material, contact area, heat input time and input current, we can estimate if the material melts by the result. If material melts, we can also roughly estimate when the melting occurs. Fig. 5,6 simply express the result that shows relationship between temperature and time and the relationship between temperature and distance from the origin.

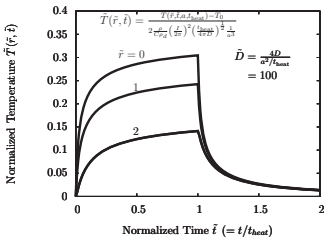

Fig.3 Temperature change with time in the approximation (1) ($\tilde{D} = 100$)

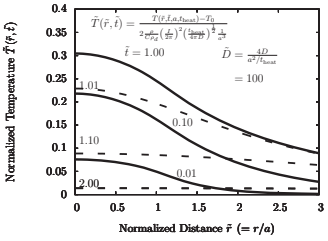

Fig.4 Temperature change with distance from heat origin in the approximation (1) ($\tilde{D} = 100$)

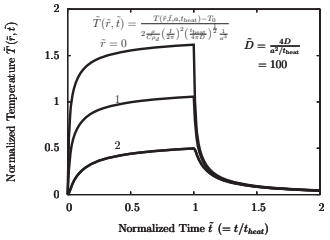

Fig.5 Temperature change with time in the approximation (2) ($\tilde{D} = 100$)

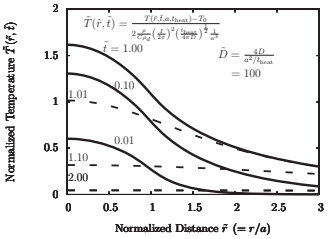

Fig.6 Temperature change with distance from origin in the approximation (2) ($\tilde{D} = 100$)

Reference

[1] Nannji Saka Bor-Jeng Wang. Thermal analysis of electrode heating and melting due to a spark. *IEEE Trans. on Compo. Hybr. and Manuf. Technol.*, Vol. 16, No. 4, pp. 456–466, 1993.

[2] Bor-Jeng Wang Chi H Leung, Anthony Lee. Thermal modeling of electrical contacts in switches and relays. *IEEE Trans. on Compo. Pack. and Manuf. Technol., Part A*, Vol. 19, No. 3, pp. 346–352, 1996.

[3] Daniel Hyman and Mehran Mehregany. Contact physics of gold microcontacts for mems switches. *IEEE Trans. on Compo. Pack. and Manuf. Technol.*, Vol. 22, No. 3, pp. 357–364, 1999.

[4] Y. YOSHIOKA. Research on the welding phenomena of a model contact and the practical contacts. *The Journal of the Institute of Electrical Engineers of Japan*, Vol. 87-2, No. 941, pp. 97–105, 1966.

[5] T. OMORI. Consideration on the ratio of the short time current carrying capacity and the continuous current carrying capacity of the point contacts. *The Journal of the Institute of Electrical Engineers of Japan*, Vol. 85-8, No. 923, pp. 111–115, 1965.

[6] Takayoshi Kubono. Temperature distribution in the constriction region of electri cal contacts carrying the dc-current. *The transactions of the Institute of Electrical Engineers of Japan.A*, Vol. 104, No. 6, pp. 47–53, 1985.

Large Eddy Simulation Using Real existing city Geometrical data for Urban boundary layer

実都市幾何形状を考慮した都市境界層の Large Eddy Simulation

学籍番号：08B27142　氏名：渡辺修　指導教官：神田学

1. はじめに

都市において住環境の変化はめざましく、市街地の開発時の大気環境アセスメントが必要になっている。建築物の周囲の流れに対する影響は系として効果が出てくるので、その再現計算には高い空間解像度が要求され、大量の計算資源を必要とする。そのため実都市の大気乱流の研究では主に、時間平均統計量に重点を置いたものが多い。本研究では Large Eddy Simulation を利用し、実都市の幾何を利用した乱流の発生と、高層建造物群の影響の細部に焦点を当て観察する。

2. 計算概要

名古屋市内から選ばれた水平 1km 四方の領域（1km×1km×0.6km）をグリッドサイズ 2.5m で解像した流体計算を行った。ある特徴的4つのエリア（Figure1）についてそれぞれ 3 次元平均流データを出力し、Dispersive-Flux、全運動量フラックスなどを計算し、グリッドごとのプロファイルを算出し、ローカルな運動量フラックスの空間分布形状について検討した。

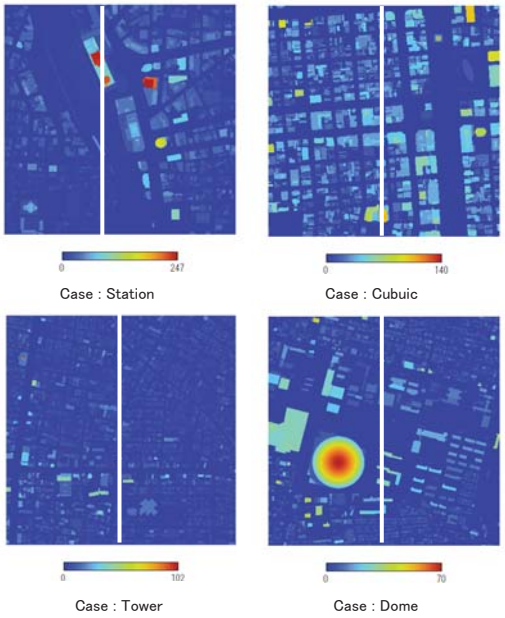

Figure 1 計算領域の建物高さのコンター図
※カラーは高度を表している

3. 結果

Figure2 は運動量フラックスの鉛直分布を示した図になる。エネルギーを吸収しているのは地面側なので値はマイナスになっている。絶対値の大きいものから。Station ＞ Cubic ＞ Dome ＞ Towerという結果になっている。

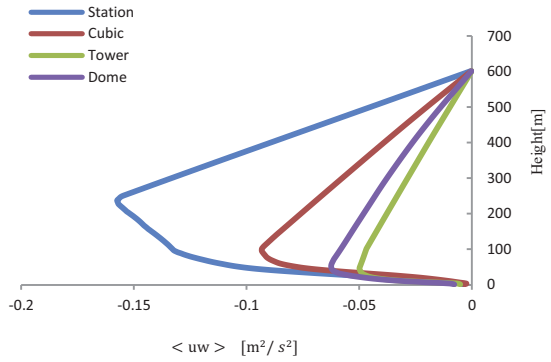

Figure 2　水平断面平均運動量フラックスの鉛直分布

運動量フラックスは乱流成分、と平均的な速度成分 2 成分に分解することができて、

$$< \overline{uw} >=< \overline{u'w'} > +< \bar{u}\bar{w} >$$

全運動量フラックス＝変動成分　＋定常成分

その乱流変動成分フラックスを Eddy-Covariance（以後＜u'w'＞）平均流速成分によるフラックスを Dispersive-Flux（以後＜u＞＜w＞）としているが、その Dispersive-Flux を書かせたものを同じように絶対値順に並べると、Station ＞ Dome ＞ Tower ≅ Cubic となった。

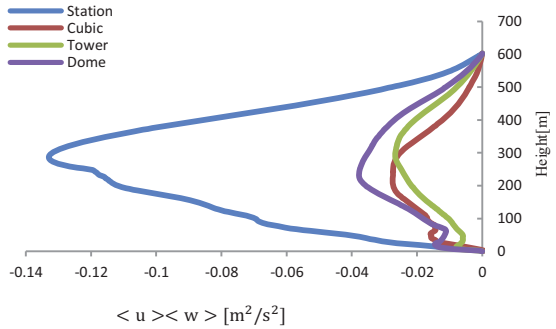

Figure 3　水平断面平均 Dispersive Flux の鉛直分布

この Figure3 を見ると Station のエリアにおいてはフラックスが大きいのはそのままだが、この平均流成分を見た時には全フラックスは 2 番目に大きかった Cubic のエリアも Tower のものと殆ど変わらない大きさになっている。

次に場所ごとにその< uw >,< u′w′ >,
< u >< w >と Building Coverage(ある水平断面をとった時に建物が占めている面積の割合) を並べてグラフにしたものを載せる。横軸のフラックスは場の特徴的な応力により定義される摩擦速度で無次元化されている。

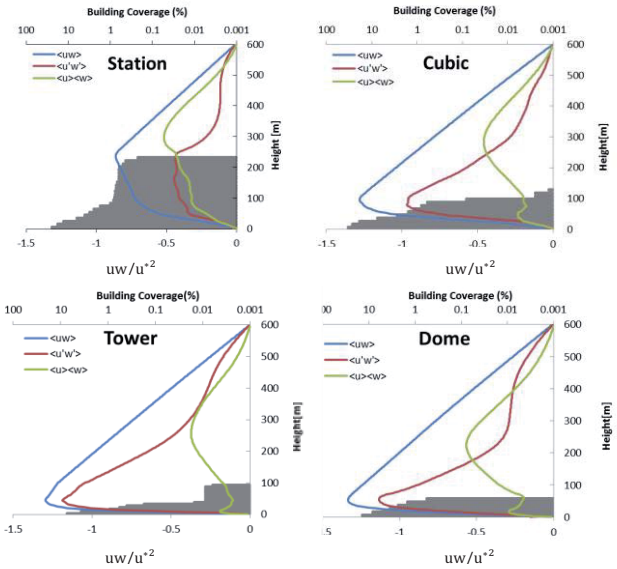

Figure 4 水平断面平均運動量フラックスの鉛直分布
水色：全運動量フラックス、赤 Eddy-Covarience、 緑：Dispersive-Flux、(横軸は摩擦速度で無次元化してある)

Figure4 は各エリアにおける< uw >,< u′w′ >,
< u >< w >の鉛直分布図になる。全運動量フラックスがおおよそ建物のある高さにおける分布と対応しているのが見て取れる。また、Dome においてとても平均流による運動量の輸送が大きいことがわかる。また、平均化時間を十分とっているので、Tower による影響もわずかながらにプロファイルから見ることができて、< uw >の頂点の高さから Tower の高さである 100m 付近の高さまで傾きの少し違う領域があり、これが電波塔の流れに与えている影響であるといえる。

Figure5 はその平均的な流れを流れ方向に対して垂直に切って、どのような循環が生じているかを表した図になる。ベクトルの長さが平均流速の強さを示しているので、Station、Dome では大型建造物の影響で建物を避けて通る風が強い定常流を作り出している様子が見える。対して Cubic,Tower の領域では対流は見られるもののベクトルの長さも短く、Tower での細くて高い建物の影響は見て取ることができないのでほぼ定常流を発生させていないと言える。逆に Cubic Tower のような形状の街では、乱流成分がより重要ということもできる。

これらより、領域に対して高い建物の立っている非一様幾何の上空では Dispersive Flux も無視できない程度のフラックスの寄与を示し、その対流の位置の固定は抵抗に直接的に関係ないとされるような建物でも起こりうることがわかった。

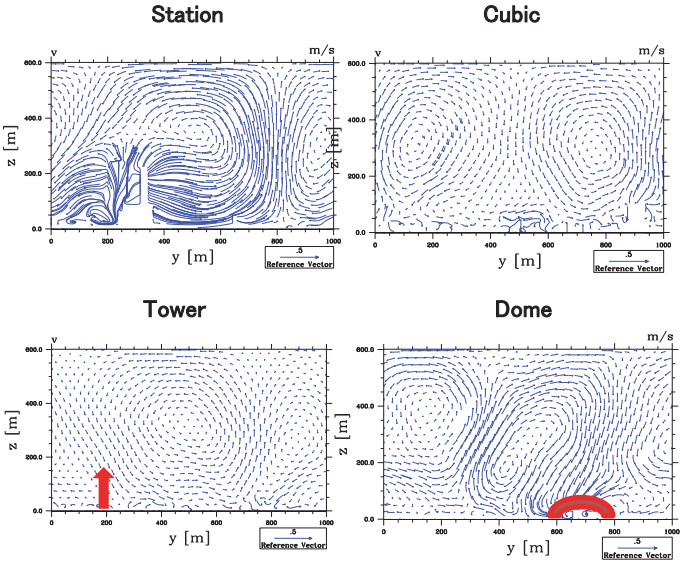

Figure 5 平均風速場の鉛直断面図
赤矢印のところには上流に電波塔 、赤い円弧の上流にはナゴヤドームがある、切断面は Figure 1 計算領域の建物高さのコンター図の白線上

4. 結論

抵抗となっている単体建造物があると言うよりは、幾つかの建物が群になることでその運動量輸送が大きくなるという事を示唆する結果を得た。

大きな建物が存在しているときはそれが軸になって大気の循環の寄与部分を大きくしている。速度の平均的に遅い領域の Dispersive Flux を原因とする部分は、建物が抵抗を作り出していると言うよりも建物が上昇流を作り出すことによって低空の低速領域を持ち上げ、間接的に建物上空に定在する遅い領域を作り出しているという結果になった。

参考文献

[1] Pijush K. Kundu and Ira M Cohen “Fluid Mechanics Third Edition” ELSEVIR ACADEMIC PRESS, 2004

[2] Kip S. Throne “Application of Classical Physics” California Institute of Technology, California , 2011

[3] Marieta Cristina Castillo, Atsushi Inagaki and Manabu Kanda “The Effect of Inner- and Outer Layer Turbulence in a Convective Boundary Layer on the Hear-Neutral Inertial Sublayer Over an Urban-Like Surface” Boundary-Layer Meteorol DOI 10.1007/s10546-011-9614-4, 2011

[4] Marcus Oliver Letzel “High resolution Large-Eddy Simulation of turbulent flow around buildings” Sept 2007